Summer 8-2022

Multi-Technique Characterization of Superconducting Materials for Particle Accelerator Applications

Junki Makita
Old Dominion University, jmakita@live.com

Recommended Citation

MULTI-TECHNIQUE CHARACTERIZATION OF SUPERCONDUCTING

MATERIALS FOR PARTICLE ACCELERATOR APPLICATIONS

by

Junki Makita
B.S. May 2012, Cornell University
M.S. December 2015, Old Dominion University

A Dissertation Submitted to the Faculty of
Old Dominion University in Partial Fulfillment of the
Requirements for the Degree of

DOCTOR OF PHILOSOPHY

PHYSICS

OLD DOMINION UNIVERSITY
August 2022

Approved by:

Alexander Gurevich (Director)

Gianluigi Ciovati (Member)

Jean R. Delayen (Member)

Gail E. Dodge (Member)

Hani Elsayed-Ali (Member)

ABSTRACT

MULTI-TECHNIQUE CHARACTERIZATION OF SUPERCONDUCTING MATERIALS
FOR PARTICLE ACCELERATOR APPLICATIONS

Junki Makita
Old Dominion University, 2022
Director: Dr. Alexander Gurevich

We investigated the performance limitations of superconducting radio-frequency (SRF) cavities and materials using multiple experimental techniques. In particular, this study focuses on understanding the surface properties of nitrogen-doped Nb cavities and superconducting thin films with higher T_c such as Nb_3Sn. The main goal of this work is to use different techniques to better understand each aspect of the complex loss mechanism in superconductors to further improve the already highly efficient SRF cavities.

Nitrogen doping applied to a Nb SRF cavity significantly improves the quality factor Q_0 compared to a conventional Nb cavity, at an expense of reduced maximum accelerating gradient. The early quench mechanism was analyzed by using temperature maps before and during the quenching. The temperature maps revealed insignificant heating before the quench, and we concluded that nitrogen doping reduces critical magnetic fields in local regions, leading to premature quenching.

To understand the origin of the increasing Q_0 with the rf field, the density of states (DOS) of cold spots from nitrogen-doped and standard cavities were measured and analyzed using scanning tunneling microscopy. The results suggested that nitrogen doping reduces the spatial inhomogeneity of superconducting properties and shrinks the metallic suboxide layers, which tunes the DOS in such a way as to produce the field-induced reduction in the surface resistance.

To characterize SRF thin films, an experimental setup for measuring a coplanar waveguide (CPW) resonator was developed and tested. A surface impedance measurement of the Nb film showed good agreement with the BCS calculation. The preliminary results from measurements of Nb_3Sn and NbTiN films are also presented here.

The nonlinear Meissner effect was investigated in Nb_3Sn film CPW resonators by measuring the resonant frequency as a function of a parallel magnetic field. Contrary to a conventional quadratic dependence of the penetration depth $\lambda(B)$ on the applied magnetic field B, as expected in s-wave superconductors, nearly a linear increase of $\lambda(B)$ with B was

observed. It was concluded that this behavior of $\lambda(B)$ is due to weakly linked grain boundaries on the polycrystalline Nb$_3$Sn films, which can mimic the NLME expected in a clean d-wave superconductor.

ACKNOWLEDGMENTS

TABLE OF CONTENTS

LIST OF TABLES

LIST OF FIGURES

Figure   Page

CHAPTER 1

INTRODUCTION

Superconducting Radio Frequency (SRF) cavities are used to accelerate charged particles and are the backbones of the large particle accelerators. Currently, the technology of the SRF cavity is based on bulk Nb that is refrigerated to cryogenic temperatures between $2\,\mathrm{K}$ to $4\,\mathrm{K}$ using cryogenic plants. The exponentially small surface resistance of the superconducting Nb allows the SRF cavities to reach high quality factors above 10^{10}. This makes it possible for the superconducting cavities to deliver accelerating gradients on the order of tens of MV/m much more efficiently compared to normal conducting copper cavities, even after taking into account the refrigeration cost.

Developing efficient SRF cavities with high accelerating gradients is imperative in order to minimize the operational cost and the size of the accelerators while keeping up with the increasing demand of the accelerator-based science. Improving the quality factor of the cavity will reduce the losses at a given accelerating gradient, which, in turn, can decrease the size and the electric power consumption of the cryogenic plants. The cavity that can sustain a higher accelerating gradient will reduce the number of the cavities needed to achieve the required energy of a beam. Furthermore, a requirement to use the liquid Helium refrigeration can be eliminated and replaced with a compact closed-cycle cryocooler that is less expensive and simpler to operate if the cavities can sufficiently operate at temperatures above $4.2\,\mathrm{K}$. Keeping the size and the running cost of the accelerators small is essential not only in improving the sustainability of the particle accelerators for science, but also for industrial and societal applications such as water decontamination, medical device sterilization, medical isotope production, and food preservation.

Over the last four decades, a significant research effort has been devoted to improving the quality factor and the accelerating gradient of the Nb cavities. Recently, it was discovered that diffusing impurities such as nitrogen into the surface of the cavity substantially increases the quality factor [1, 2]. This discovery was so successful, that it was rapidly adopted as a part of the treatment for the SRF cavities to be used in the LCLS-II project [3]. However, most of the nitrogen-doped cavities suffered from reduced maximum accelerating gradient. Understanding the causes of the enhanced quality factor and the lower quench field due to

the nitrogen-doping is not only important to gain fundamental knowledge of SRF physics, but also for application purposes to build more efficient cavities.

To further improve the performance of the SRF cavities beyond the intrinsic limit of the Nb, there has been a growing effort in search of alternatives to bulk Nb cavities. Some of the innovations include using a thin film of Nb on a copper cavity to improve thermal stability and depositing thin film materials with higher T_c and higher critical magnetic field on the inner surface of Nb cavities. A thin film of Nb_3Sn deposited on the inner surface of Nb cavities is a promising candidate for future applications. With its T_c of $18\,K$, the Nb_3Sn treated cavities have the potential to significantly simplify cryogenic operations. Recent progress on the Nb_3Sn treated cavities has resulted in the single-cell cavities reaching the maximum gradient as high as $24\,MV/m$; yet, this is still $\sim 50\,\%$ of the accelerating gradient achieved by the Nb cavities [4]. To realize the full potential, further investment in the research and development of the Nb_3Sn film is needed.

The first part of the dissertation focuses on understanding the surface properties of the nitrogen-doped cavities using both the temperature mappings and the scanning tunneling microscopy (STM). In particular, the surface oxide contributions to the superconducting properties of the nitrogen-doped cavities were studied in comparison to that of the standard treated Nb cavities. The results give insights into the effects the nitrogen doping has on the surface of the Nb as well as new ways to improve the performance of the SRF cavities. The second part of the work describes using the coplanar waveguide resonators to measure thin film superconductors. Experimental procedures and results for extracting superconducting properties from rf measurements on thin film resonators made with Nb, NbTiN, and Nb_3Sn are presented. Furthermore, magnetic field dependent measurements were carried out using the probe station to investigate the nonlinear Meissner effect in the Nb_3Sn films. The rf measurement procedure described in this dissertation provides a robust benchmarking method for characterizing thin film superconductors, and the results of the nonlinear Meissner effect give insight into how the Nb_3Sn films respond under parallel magnetic fields.

This dissertation begins with chapter 2 where the overview of the theory of superconductivity relevant to this work is given. Chapter 3 gives a brief outline of the electrodynamics of the superconducting rf cavities. In chapter 4, the basics of transmission line physics as well as analytical techniques for the superconducting coplanar waveguide resonators are described. In chapter 5, studies of the nitrogen-doped cavities are presented. This includes the results of the temperature mappings and detailed procedures and analysis results of the scanning tunneling microscopy on the coupons from the nitrogen-doped and the standard treated Nb

cavities. Chapter 6 moves on to the characterizations of the thin film superconductors using the coplanar waveguide resonators. The design of the probe-coupled measurements is given in detail, and the results from the rf measurements on Nb, NbTiN, and Nb_3Sn thin films are presented. Chapter 7 studies the nonlinear Meissner effect in Nb_3Sn thin-film coplanar waveguide resonator. This includes the description of the cryogenic probe station used in the experiment and results from the measurement of the resonant frequency as a function of a parallel magnetic field. Lastly, chapter 8 gives the summary of the dissertation and the future outlook.

CHAPTER 2

PHYSICS OF SUPERCONDUCTIVITY

2.1 LONDON THEORY

In 1934, Gorter and Casimir characterized the properties of superconductivity using a two-fluid model [5]. This phenomenological model assumed the coexistence of normal and superconducting electrons below T_c. The two types of electrons contributed separately to the total current density as follows:

$$\boldsymbol{J} = \boldsymbol{J_n} + \boldsymbol{J_s}, \tag{1}$$

$$= n_n e \boldsymbol{v_n} + n_s e \boldsymbol{v_s}, \tag{2}$$

where n_n and n_s are densities of normal and superconducting electrons respectively. Based on this model, Fritz and Heinz London proposed two equations that described the electrodynamic features of the superconductor: perfect conductivity and screening of magnetic field within the penetration depth λ_L, the latter being referred to as the Meissner effect. The London equations are

$$\frac{\partial \boldsymbol{J}}{\partial t} = \frac{1}{\mu_0 \lambda_L^2} \boldsymbol{E}, \tag{3}$$

$$\boldsymbol{B} = -\mu_0 \lambda_L^2 \nabla \times \boldsymbol{J}, \tag{4}$$

where

$$\lambda_L = \sqrt{\frac{m}{\mu_0 n_s e^2}}, \tag{5}$$

is the London penetration depth [6]. The first equation replaces the normal conducting Ohm's law and is derived from the response of an electron to an electric field in the Drude Model: $m\frac{d\boldsymbol{v}}{dt} = e\boldsymbol{E} - m\frac{\boldsymbol{v}}{\tau}$, where τ is the phenomenological scattering time. Letting $\tau = \infty$ models a perfect conductor, and substituting $\boldsymbol{v} = \frac{\boldsymbol{J}}{ne}$ derives Eq. (3). The second London equation describes the Meissner effect in the superconductor. Substituting $\nabla \times \boldsymbol{B} = \mu_0 \boldsymbol{J}$ into Eq. (4) yields

$$\nabla^2 \boldsymbol{B} = \frac{1}{\lambda_L^2} \boldsymbol{B}, \tag{6}$$

which has the general solution of the form $B(x) = B_0 e^{-x/\lambda_L}$. The equation shows a magnetic field decaying exponentially inside the superconductor with the London penetration depth as the length scale. The London penetration diverges at $T = T_c$ and approaches a minimum at $T = 0$. The temperature dependence of λ_L near T_c is approximated as [7]

$$\lambda_L(T) = \frac{\lambda_L(0)}{\sqrt{1 - \left(\frac{T}{T_c}\right)^4}}. \tag{7}$$

2.2 THE PIPPARD NON-LOCAL RELATION

In the early 1950s, Pippard conducted a series of experiments to measure the change in the resonant frequency of a superconducting wire with increasing static magnetic field and determined the penetration depth to vary with impurity concentration [8]. In his experiment, the penetration depth of Sn doubled with an addition of 3% In impurity while the critical temperature and field were only slightly affected. This result contradicted the London penetration depth that depended only on the effective mass and density of the superconducting electrons.

In analogy with the anomalous skin effect in a normal conductor, Pippard introduced a "coherence length" ξ and proposed a new non-local formula to supersede the London equation:

$$\mathbf{J(r)} = -\frac{3}{4\pi\xi_0\Lambda} \int \frac{\mathbf{R}\left[\mathbf{R} \cdot \mathbf{A(r')}\right]}{R^4} e^{-R/\xi} d\mathbf{r'}, \tag{8}$$

where $\mathbf{R} = \mathbf{r} - \mathbf{r'}$, $\Lambda = \mu_0\lambda_L^2$, and ξ is dependent on the mean free path l and a constant characteristic length ξ_0 as

$$\frac{1}{\xi} = \frac{1}{\xi_0} + \frac{1}{l}. \tag{9}$$

Equation 8 describes $\mathbf{J(r)}$ in response to $\mathbf{A(r')}$ at points $\mathbf{r'}$ within the radius of ξ around $\mathbf{r}$. ξ_0 was interpreted by Pippard as the characteristic length scale of the superconducting electron wave function. In the limit $\lambda_L \gg \xi$, $\mathbf{A(r')}$ varies much more slowly compared to an external field, so $\mathbf{A}$ can be taken out of the integral in Eq. (8), and the magnetic penetration depth λ depends on the mean free path as follows:

$$\lambda = \lambda_L \left(1 + \frac{\xi_0}{l}\right)^{1/2}. \tag{10}$$

2.3 GINZBURG-LANDAU THEORY

Ginzburg and Landau developed a macroscopic theory of superconductivity that introduced a complex wave function $\psi(\mathbf{r})$ such that $|\psi(\mathbf{r})|^2$ is proportional to the density of superconducting electors n_s [9]. The theory introduced a spatial variation in n_s and a non-linear response to fields. The Ginzburg-Landau (GL) theory postulates that at temperatures close to T_c where $|\psi|^2$ is small, the free energy density can be expanded in series of $|\psi|^2$ and its small spatial gradients as shown below:

$$F(\mathbf{r}, T) = F_n(\mathbf{r}, T) + \alpha|\psi|^2 + \frac{\beta}{2}|\psi|^4 + \frac{1}{2m^*}\left|(-i\hbar\nabla - 2e^*\mathbf{A})\,\psi\right|^2 + \frac{\mathbf{B}^2}{2\mu_0}, \qquad (11)$$

where $F_n(\mathbf{r}, T)$ is the free energy density of the normal state. The kinetic energy associated with the external field is taken into account with the momentum operator $\mathbf{p} = (-i\hbar\nabla - 2e\mathbf{A})$, and the last term is the magnetic self-energy. Only the even powers $\psi\psi^*$ are included because the order parameter is complex and the right hand side of the equation must be real.

The coefficient $\alpha(T) = \alpha'(T - T_c)$ changes sign at the critical temperature T_c. In an absence of a field, if $\alpha > 0$ the free energy is minimized when $|\psi| = 0$ which corresponds to $F(\mathbf{r}, T) = F_n(\mathbf{r}, T)$ or a normal state. For a negative α and a positive β, the lowest free energy is achieved when

$$|\psi|^2 = -\frac{\alpha}{\beta} = |\psi_\infty|^2. \qquad (12)$$

The difference in free energy between the normal and superconducting state $F(\mathbf{r}, T) - F_n(\mathbf{r}, T)$ at this value gives the thermodynamic critical field:

$$\frac{\mu_0 H_c^2}{2} = \frac{\alpha^2}{2\beta}. \qquad (13)$$

The critical field H_c refers to the maximum field that can be applied to the superconductor without destroying its superconductivity. The value of α is positive for $T > T_c$ and becomes negative at $T < T_c$ at the phase transition. By expanding in series near T_c with respect to $t = T/T_c$, the temperature dependence of α is derived to be

$$\alpha(t) = \alpha'(t - 1), \qquad (14)$$

which indicates that H_c varies by $(1 - t)$ with temperature.

Expanding the fourth term in Eq. (11) using $\psi = |\psi|e^{i\phi}$ we obtain

$$\frac{1}{2m^*}\left[\hbar^2(\nabla|\psi|)^2 + (\hbar\nabla\phi - 2e^*\boldsymbol{A})^2|\psi|^2\right].\tag{15}$$

The second term is associated with the kinetic energy of the supercurrent, which is simply $\frac{e^{*2}\boldsymbol{A}^2}{2m^*}|\psi|^2$ when using constant ϕ in the London gauge. Comparing this with the kinetic energy density expression from the London theory, we can obtain the penetration depth

$$\lambda^2 = \left(\frac{m^*}{e^{*2}\mu_0|\psi|^2}\right)^{1/2},\tag{16}$$

which is identical to λ_L when $|\psi|^2 = \frac{n_s}{2}$, $e^* = 2e$, and $m^* = 2m$ where e and m are the electron charge and mass, respectively.

In the absence of fields, currents, or gradients, the free energy Eq. (11) is minimized with $|\psi|^2 = |\psi_\infty|^2$; however, when the boundary conditions are imposed, minimization of the free energy with respect to the order parameters $|\psi|$ and $|\boldsymbol{A}|$ leads to the following GL equations:

$$\alpha\psi + \beta|\psi|^2\psi + \frac{1}{2m}\left(-i\hbar\nabla - 2e\boldsymbol{A}\right)^2\psi = 0,\tag{17}$$

and

$$\boldsymbol{J} = \frac{e}{m}\left[\psi^*\left(-i\hbar\nabla - 2e\boldsymbol{A}\right)\psi\right] + c.c.\tag{18}$$

In a case with no magnetic field, Eq. (17) can be solved to obtain the characteristic length of a spatial variation of $|\psi|$ as

$$\xi^2 = \left(\frac{\hbar^2}{2m\alpha(T)}\right) \propto \frac{1}{1 - T/T_c}.\tag{19}$$

This is called Ginzburg-Landau coherence length and is different from the ξ_0 in Pippard's definition. The temperature-dependent coherence length $\xi(T)$ describes the healing length of the wavefunction when the superconductor is perturbed, for example by magnetic field or inclusion of normal metal.

A dimensionless Ginzburg-Landau parameter κ is the ratio between the penetration depth and the coherence length:

$$\kappa = \frac{\lambda(T)}{\xi(T)}.\tag{20}$$

The value of $\kappa = 1/\sqrt{2}$ separates superconductors into two types of superconductors:

Type I: $\kappa < 1/\sqrt{2}$,
Type II: $\kappa > 1/\sqrt{2}$.

For a type II superconductor, it is energetically favorable to create a mixed state of normal and superconducting regions above $H = H_{c1}$. When the field is increased beyond H_{c1}, the magnetic flux penetrates the material in the form of quantized flux lines or vortices, until $H = H_{c2}$ where the superconducting state transitions into the normal state [10]. The vortex has a normal core with a circulating supercurrent, producing a total flux equal to

$$\Phi_0 = \frac{h}{2e} = 2.07 \times 10^{-15} T \cdot m^2. \tag{21}$$

In a presence of a current, the vortex experiences the Lorentz force $\boldsymbol{f} = \boldsymbol{J} \times \Phi_0$ causing the flux line to move perpendicular to the direction of the current. This motion of the vortex results in the time variation of the field, giving rise to an electric field which will produce resistive loss inside the normal core of the vortex. Therefore, the presence of the vortex breaks the lossless superconductivity unless the flux is pinned by material defects.

2.4 COOPER PAIR

A microscopic theory of superconductivity was developed by Bardeen, Cooper, and Schrieffer (BCS) and provided a comprehensive explanation for the origin of superconductivity 46 years after its first discovery [11]. The theory showed that a weak attractive electron-electron interaction creates a bound state below the Fermi surface. This formation of the pair of electrons or Cooper pairs below the Fermi level resulted in an energy gap $\Delta \simeq kT_c$ in the electron energy spectrum.

Experiments conducted in 1950 had shown that a transition temperature of mercury varied inversely with the square root of its isotopic mass [12, 13]. These results confirmed the importance of electron-phonon interaction in superconductivity [14]. It was later shown by Fröhlich, Bardeen, and Pines that an electron-electron interaction due to exchange of phonons results in attraction between two electrons with opposite momenta and spins, which can be stronger than the direct Coulomb repulsion [15, 16]. The phonon-mediated attraction occurs when a first electron attracts positively charged ions and deforms the lattice. The density of positive ions is increased on its trail, which can then attract a second electron passing through. The sequence of events effectively produces the attractive interaction between the first and the second electrons.

Cooper showed that when such a pair of electrons is added to the sea of Fermi electrons, they will form a bound state below the Fermi level [17]. The Schrodinger's equation for the

two-particle system can be written as [7]

$$(H_0 + V) \sum_{\boldsymbol{k}} g_{\boldsymbol{k}} |\boldsymbol{k}, -\boldsymbol{k}\rangle = E \sum_{\boldsymbol{k}} g_{\boldsymbol{k}} |\boldsymbol{k}, -\boldsymbol{k}\rangle , \tag{22}$$

where $|\boldsymbol{k}, -\boldsymbol{k}\rangle$ is the two-particle state with $H_0 |\boldsymbol{k}, -\boldsymbol{k}\rangle = 2\epsilon_{\boldsymbol{k}} |\boldsymbol{k}, -\boldsymbol{k}\rangle$. In the equation, two electrons are assigned equal and opposite momentum to yield the lowest energy state possible. The interaction potential V was approximated to be constant within a narrow energy shell of width $\hbar\omega_c$ around the Fermi surface and zero everywhere else. The solution to the energy eigenvalue of the system with respect to the Fermi energy E_F is

$$E = -2\hbar\omega_c e^{-2/N(0)V}, \tag{23}$$

in the weak-coupling approximation $N(0)V \ll 1$ where $N(0)$ is the density of states for electrons at the Fermi level [7]. The result shows that in the presence of the attractive potential, the Cooper pairs condense into a ground state with energy below E_F, suggesting a gap in the energy spectrum.

2.5 BCS GROUND STATE

Cooper's calculation showed that the Fermi sea of electrons would be unstable when the attractive potential exists between them [17]. This means that the electrons will form pairs until the system departs enough from the normal metal state and becomes energetically unfavorable to form another pair. Bardeen, Cooper, and Schrieffer extended Cooper's calculation to describe this complicated state of electron pairs in their famous BCS theory.

The wavefunction proposed in the BCS theory takes the form

$$\Psi_{BCS} = \prod_{\boldsymbol{k}} \left(u_{\boldsymbol{k}} + v_{\boldsymbol{k}} \hat{c}_{\boldsymbol{k}\uparrow}^{\dagger} \hat{c}_{-\boldsymbol{k}\downarrow}^{\dagger} \right) |\phi_0\rangle , \tag{24}$$

where $\hat{c}_{\boldsymbol{k}\uparrow}^{\dagger}$ is a fermion creator operator that creates an electron with momentum $\boldsymbol{k}$ and spin $\uparrow$ and $|\phi_0\rangle$ is the vacuum state [7, 11]. A probability that a pair state $(\boldsymbol{k}\uparrow, -\boldsymbol{k}\downarrow)$ is occupied is $|v_{\boldsymbol{k}}|^2$ and unoccupied is given by $|u_{\boldsymbol{k}}|^2 = 1 - |v_{\boldsymbol{k}}|^2$. This wavefunction relaxes a restriction of fixing a number of particles in a system and instead describes a superposition of pair states containing 2 to ∞ electrons. The Hamiltonian of the pair system is

$$\mathscr{H} = \sum_{\boldsymbol{k}\sigma} \xi_{\boldsymbol{k}} \hat{c}_{\boldsymbol{k}\sigma}^{\dagger} \hat{c}_{\boldsymbol{k}\sigma} + \sum_{\boldsymbol{k}\boldsymbol{k}'} V_{\boldsymbol{k}\boldsymbol{k}'} \hat{c}_{\boldsymbol{k}\uparrow}^{\dagger} \hat{c}_{-\boldsymbol{k}\downarrow}^{\dagger} \hat{c}_{-\boldsymbol{k}'\downarrow} \hat{c}_{\boldsymbol{k}'\uparrow}, \tag{25}$$

where $\xi_{\boldsymbol{k}} = \epsilon_{\boldsymbol{k}} - \mu$ is a single particle energy measured from the Fermi energy and $V_{\boldsymbol{k}\boldsymbol{k}'}$ is the attractive interaction potential of the pair that follows the Cooper's model [7, 11]. $u_{\boldsymbol{k}}^2$ and $v_{\boldsymbol{k}}^2$ are calculated by minimizing $\langle\Psi_{BCS}| \mathscr{H} |\Psi_{BCS}\rangle$ to be

$$v_{\boldsymbol{k}}^2 = \frac{1}{2}\left[1 - \frac{\xi_{\boldsymbol{k}}}{(\Delta^2 + \xi_{\boldsymbol{k}}^2)^{1/2}}\right], \tag{26}$$

$$u_{\boldsymbol{k}}^2 = 1 - v_{\boldsymbol{k}}^2 = \left[1 + \frac{\xi_{\boldsymbol{k}}}{(\Delta^2 + \xi_{\boldsymbol{k}}^2)^{1/2}}\right], \tag{27}$$

where

$$\Delta = \frac{\hbar\omega_c}{\sinh[1/N(0)V]} \approx 2\hbar\omega_c e^{-1/N(0)V}, \tag{28}$$

for $N(0)V \ll 1$ [7, 11]. The Cooper pair occupation probability $v_{\boldsymbol{k}}^2$ as a function of single-particle energy is shown in the Fig. 1. Unlike the Fermi function of a normal metal, the distribution near the Fermi energy is smeared out at $T = 0$. In the superconducting state, some of the states outside the Fermi sphere are occupied to create pair interaction that results in an overall reduction of energy compared to the normal metal state.
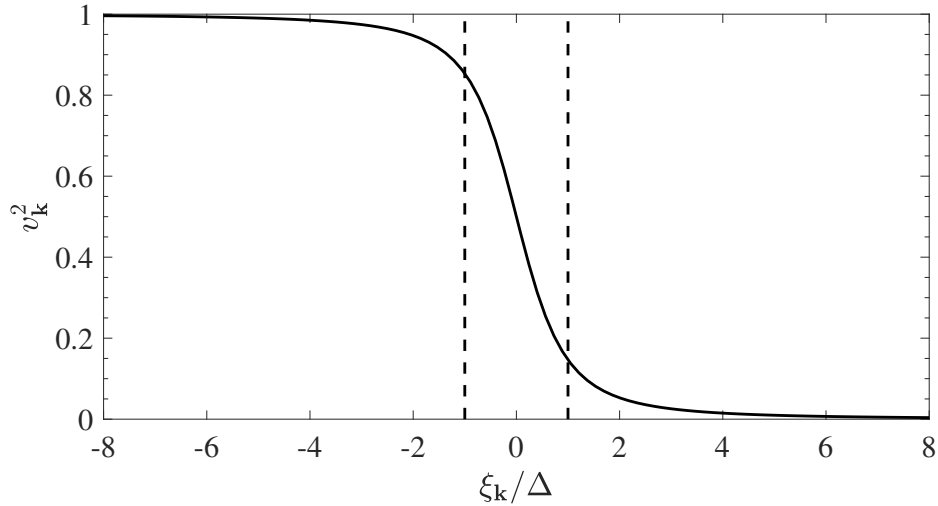
FIG. 1: A probability amplitude that a pair state with momentum $\boldsymbol{k}$ is occupied is smeared out around Δ as opposed to a sharp step function at $T = 0$.

An excited state of the superconductor involves breaking up a Cooper pair due to some

external excitation. If an electron in a state $\boldsymbol{k}\uparrow$ is scattered, it will leave an electron in a state $-\boldsymbol{k}\downarrow$ unpaired. Because of this correlation, the elementary excitation from the ground state superconductor involves quasiparticle creation and destruction operators that mixes the electron-like and hole-like operators as shown by Bogoliubov [18]

$$\hat{\gamma}_{\boldsymbol{k}\uparrow} = u_{\boldsymbol{k}}\hat{c}_{\boldsymbol{k}\uparrow} + v_{\boldsymbol{k}}\hat{c}_{-\boldsymbol{k}\downarrow}^{\dagger}, \tag{29}$$

$$\hat{\gamma}_{\boldsymbol{k}\uparrow}^{\dagger} = u_{\boldsymbol{k}}\hat{c}_{\boldsymbol{k}\uparrow}^{\dagger} - v_{\boldsymbol{k}}\hat{c}_{-\boldsymbol{k}\downarrow}. \tag{30}$$

Diagonalizing the Hamiltonian of Eq. (25) using the new operators show the excitation energy to be

$$E_{\boldsymbol{k}} = \left(\xi_{\boldsymbol{k}}^2 + |\Delta_{\boldsymbol{k}}|^2\right)^{1/2}, \tag{31}$$

where the gap

$$\Delta_{\boldsymbol{k}} = \sum_{\boldsymbol{l}} V_{\boldsymbol{k}\boldsymbol{l}} \frac{\Delta_{\boldsymbol{l}}}{2E_{\boldsymbol{l}}} \tanh\frac{E_{\boldsymbol{l}}}{2k_B T}, \tag{32}$$

where the summation over $\boldsymbol{l}$ is restricted by a narrow energy shell of thickness $\hbar\omega_D$ at the Fermi surface, where ω_D is the Debye frequency. Equation (31) shows that the minimum energy required for the excitation is Δ above the Fermi surface; thus the superconductor exhibits an energy gap Δ in the density of states. The quasiparticle density of states $N_s(E)$ normalized to the normal metal density of states is

$$\frac{N_s(E)}{N(0)} = \frac{d\xi}{dE} = \begin{cases} \dfrac{E}{\left(E^2 - \Delta^2\right)^{1/2}}, & (E > \Delta), \\ 0, & (E < \Delta). \end{cases} \tag{33}$$

$N_S(E)/N(0)$ at $T = 0$ is shown in Fig. 2. The density of states is zero for $|E| < \Delta$ and diverges at $E = \Delta$.

For $T > 0$, the probability of quasiparticle excitation follows the normal metal Fermi function $f(E_{\boldsymbol{k}}) = \left(e^{E_{\boldsymbol{k}}/k_B T} + 1\right)^{-1}$. As the temperature increases, more quasiparticles are excited and $\Delta(T)$ is reduced, until it becomes zero at the critical temperature T_c. From the BCS theory, $\Delta(0)$ and T_c are related by

$$\frac{\Delta(0)}{kT_c} = 1.764. \tag{34}$$

Furthermore, in the BCS approximation where the interaction potential $V_{\boldsymbol{k}\boldsymbol{l}} = -V$ and $\Delta_{\boldsymbol{k}} = \Delta$, Eq. (32) can be solved numerically to yield temperature dependence of gap $\Delta(T)$
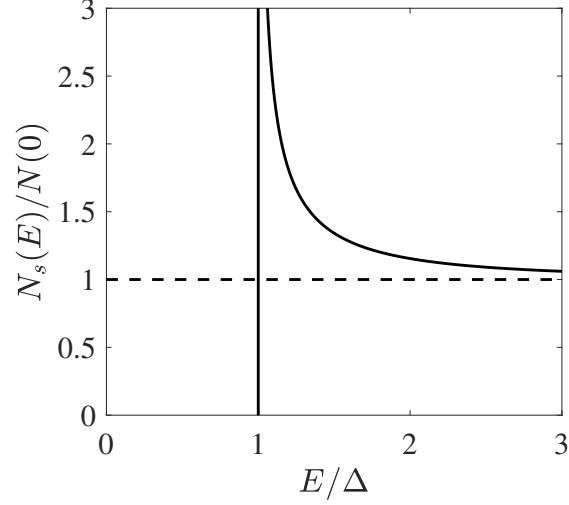
FIG. 2: A superconducting density of states normalized to that of a normal metal is shown in a solid line and a dashed line indicates the normal metal density of states. The density of states is zero within a gap Δ and has a sharp divergence at an energy just above Δ for a superconductor at $T = 0$.

as shown in the Fig. 3. Two limiting cases can be approximated as below [7]:

$$\frac{\Delta(T)}{\Delta(0)} \approx \begin{cases} 1 - e^{-\beta\Delta(0)}, & \frac{T}{T_c} < \frac{1}{3}, \\ 1.74\left(1 - \frac{T}{T_c}\right)^{1/2}, & \frac{T}{T_c} \to 1, \end{cases} \tag{35}$$

which indicates that the Δ remains approximately constant for low T.

2.5.1 COMPLEX CONDUCTIVITY

A superconductor is lossless only when dc field is applied and becomes resistive when ac field is applied. A complex conductivity of a superconductor is derived starting from the Maxwell's equation:

$$\nabla^2 \mathbf{E} = \mu_0 \frac{\partial \mathbf{J}}{\partial t}. \tag{36}$$

Substituting for $\mathbf{J} = \mathbf{J_n} + \mathbf{J_s} = \sigma_1 \mathbf{E} + \mathbf{J_s}$ results in

$$\nabla^2 \mathbf{E} = \mu_0 \sigma_1 \frac{\partial \mathbf{E}}{\partial t} + \frac{\mathbf{E}}{\lambda_L^2}, \tag{37}$$
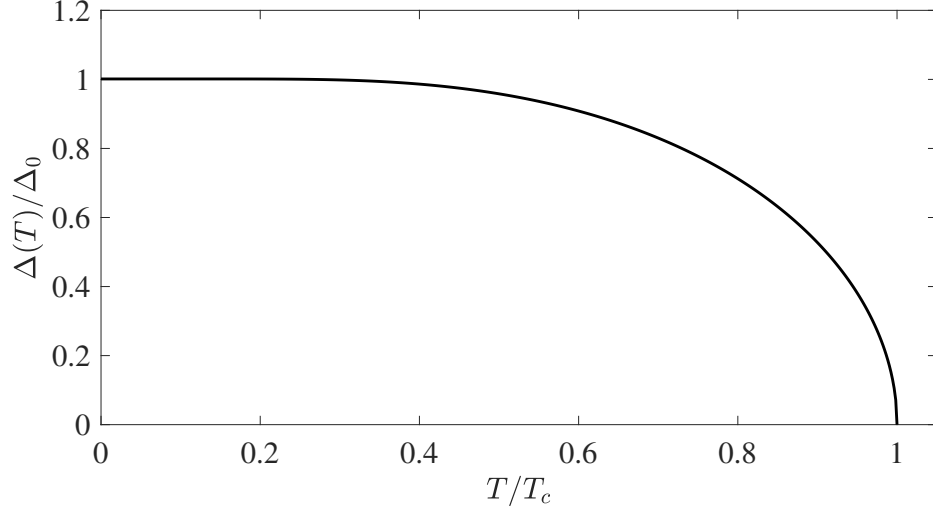
FIG. 3: Temperature dependence of Δ for a weak-coupling superconductor. The gap is nearly constant for low T and then drops sharply to zero at T_c.

where the second term is derived from Eq. (3). The conductivity σ_1 arises from thermally excited normal electrons that are generated from breaking of Copper pairs. For a field with sinusoidal time dependence, Eq. (37) becomes

$$\nabla^2 \mathbf{E} = i\omega\mu_0 \left(\sigma_1 - i\frac{1}{\omega\mu_0\lambda_L^2} \right) \mathbf{E}. \tag{38}$$

This form is analogous to the wave equation in a normal conductor when the complex conductivity $\sigma = \sigma_1 - i\sigma_s$ is introduced [19]:

$$\nabla^2 \mathbf{E} = i\omega\mu_0\sigma\mathbf{E}, \tag{39}$$

where the imaginary part is

$$\sigma_s = \frac{1}{\omega\mu_0\lambda_L^2}. \tag{40}$$

An effect of the complex conductivity can be visualized using a simple equivalent circuit model shown in Fig. 4. In this model, a resistance from σ_1 is connected in parallel with a lossless reactance from σ_s. When $\mathbf{J}$ is constant in time, all the currents are shorted toward σ_s without any loss. This reactive part called kinetic inductance emerges from a finite inertia of the Cooper pairs to oppose a change in the current when $\mathbf{J}$ is dependent on time. Because
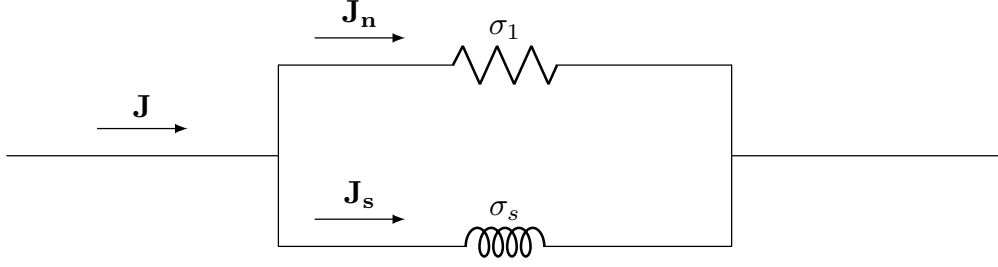
FIG. 4: An equivalent representation of complex conductivity in the circuit diagram.

it takes a finite amount of time for the Cooper pairs to respond to the alternating field, a phase lag with respect to the external field occurs. Therefore, some of the oscillating current can travel through the normal, lossy resistance.

2.6 SURFACE IMPEDANCE

The electromagnetic behavior of a metal is described by a surface impedance defined by the ratio $Z_s = E_x(0)/H_y(0)$. An expression for the surface impedance in the two-fluid approximation is given by [20]:

$$Z_s = \frac{E_x(0)}{H_y(0)} = \sqrt{\frac{i\omega\mu}{\sigma_1 - i\sigma_s}}. \tag{41}$$

For $\sigma_s \gg \sigma_1$, the surface resistance R_s and surface reactance X_s are given as [20]

$$Z_s = R_s + iX_s = \frac{\omega^2\mu^2\sigma_1\lambda^3}{2} + i\omega\mu\lambda. \tag{42}$$

The surface resistance in a superconductor has ω^2 dependency in contrast to $\sqrt{\omega}$ of the normal conductors, and this prediction has been observed in clean conventional superconductors [20].

The total internal inductance L_I is defined as

$$L_I = L_m + L_k. \tag{43}$$

It is a sum of magnetic L_m and kinetic L_k inductance. L_m originates from magnetic energy stored by the field penetrating into the conductor by the length scale λ, and L_k is derived from the kinetic energy of the super electrons. In the approximation $\sigma_s \gg \sigma_1$, L_m is equal to L_k [19].

A detailed expression for σ_1 that takes into the temperature-induced pair breaking effect has been calculated in the BCS theory. For frequencies below the gap frequency $\omega < \omega_D = 2\Delta/\hbar$, the ratio of σ_1/σ_n in the normal state is given as [7]

$$\frac{\sigma_1}{\sigma_n} = \frac{1}{\hbar\omega} \int_{-\infty}^{\infty} \frac{(E^2 + \hbar\omega E + \Delta^2)[f(E) - f(E + \hbar\omega)]}{(E^2 - \Delta^2)^{1/2}[(E + \hbar\omega)^2 - \Delta^2]^{1/2}}, \tag{44}$$

where σ_n is the normal state conductivity. This integral must be calculated numerically for a general case, but in the limits of frequencies much lower than the gap $\hbar\omega \ll \Delta$ and low temperatures $k_B T \ll \Delta$, it is approximated in a much simpler form:

$$\frac{\sigma_1}{\sigma_n} \approx \frac{4\Delta}{\hbar\omega} e^{-\Delta/k_B T} \sinh\left(\frac{\hbar\omega}{2k_B T}\right) K_0\left(\frac{\hbar\omega}{2k_B T}\right), \tag{45}$$

where K_0 is the modified Bessel function of the second kind [21]. Since $\hbar\omega/2k_B T \approx 10^{-2}$, Eq. (45) can be further simplified using $\sinh(x) \approx x$ and $K_0(x) \approx -\gamma + \ln(2/x)$ where γ is the Euler-Mascheroni constant [22, 23]. The approximate expression for the BCS conductivity becomes

$$\frac{\sigma_1}{\sigma_n} \approx \frac{2\Delta}{k_B T} e^{-\Delta/k_b T} \ln\left(\frac{C k_B T}{\hbar\omega}\right), \tag{46}$$

where $C = 4/e^\gamma \approx 2.25$ [23]. An approximate form of the BCS surface resistance is then derived by substituting Eq. (46) into the real part of Eq. (42):

$$R_s = \frac{\mu_0^2 \omega^2 \lambda^3 \Delta \sigma_n}{k_B T} \ln\left(\frac{C k_B T}{\hbar\omega}\right) e^{-\Delta/k_B T}. \tag{47}$$

The expression reveals that the surface resistance of a superconductor decreases exponentially with T.

The surface impedance described by Eq. (47) and Eq. (42) is applicable in the local limit where the characteristic length scale ξ or l is much smaller than the decay length λ and the conventional Ohm's law $\mathbf{J} = \sigma\mathbf{E}$ hold true. On the other hand, a non-local relation between the current density $\mathbf{J}(\mathbf{r})$ and the vector potential $\mathbf{A}(\mathbf{r}')$ is described by the BCS theory in analogous to Eq. (8):

$$\boldsymbol{J}(\boldsymbol{r}) = \frac{3}{4\pi v_F \hbar \lambda_L^2} \int \frac{\boldsymbol{R}\boldsymbol{R} \cdot \boldsymbol{A}(\boldsymbol{r}') I(\omega, R, T) e^{-R/l}}{R^4} d\boldsymbol{r}', \tag{48}$$

where $\boldsymbol{R} = \boldsymbol{r}' - \boldsymbol{r}$ [24]. The Mattis-Bardeen kernel $I(\omega, R, T)$ decays over the coherence length proposed in the BCS model:

$$\xi_0 = \frac{\hbar v_F}{\pi\Delta}, \tag{49}$$

where v_F is the Fermi velocity at $T = 0$ [24]. This equation describes $\boldsymbol{J(r)}$ in response to the values of $\boldsymbol{A(r')}$ around the radius $\xi^{-1} \approx \xi_0^{-1} + l^{-1}$. Equation (48) can be used with Maxwell's equation to derive surface impedance of the superconductor for diffuse surface scattering [25]:

$$Z_s = i\mu_0\omega \frac{\pi}{\int_0^\infty \ln\left(1 + \frac{Q(k,\omega)}{k^2}\right) dk},$$
(50)

where $Q(k,\omega)$ is the Fourier transformed kernel. Equation (50) is calculated numerically to extract the real and imaginary part of the surface impedance given the necessary material parameters for the superconductor.

Taking the real part of Eq. (50) gives an expression for the penetration depth [7]:

$$\lambda(T) = \frac{\pi}{\text{Re}\left[\int_0^\infty \ln\left(1 + \frac{Q(k,\omega)}{k^2}\right) dk\right]}.$$
(51)

In the limit, $\xi, \lambda \ll l$, so-called "clean limit", the temperature dependnce of $\lambda(T)$ calculated using Eq. (51) resembles the Gorter-Casimir temperature dependence $\lambda(T) \propto 1/\sqrt{(1 - (T/T_c)^4}$. On the other hand, in the limit $\xi \gg l$, so-called "dirty limit," $\lambda(T)$ diverges slightly from the Gorter-Casimir temperature dependence. The numerically calculated $\lambda(T)$ for both limits are compared with $1/\sqrt{(1 - (T/T_c)^4}$ in Fig. 5.
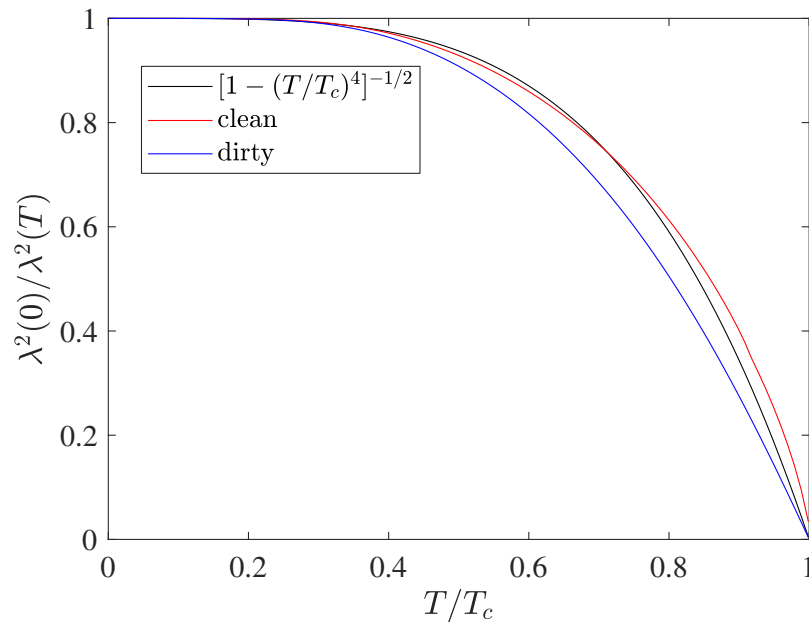
FIG. 5: Comparison of the temperature dependence of magnetic penetration depth. Clean limit $\xi \ll l$ temperature dependence becomes closer to that of two-fluid approximation, while in the dirty limit, $\lambda(T)$ increases faster with T.

CHAPTER 3

BASICS OF SUPERCONDUCTING RADIO FREQUENCY CAVITIES

3.1 ELECTROMAGNETICS OF RF CAVITIES

An rf cavity is an conductive enclosed structure that can store an oscillating electromagnetic field. The electromagnetic field in the cavity can be calculated for a simple model of a cylinder with two end caps or a "pillbox cavity" with perfectly conducting wall. The electromagetic field satisfies the following boundary conditions:

$$\hat{n} \times \mathbf{E} = 0, \tag{52}$$

$$\hat{n} \cdot \mathbf{H} = 0, \tag{53}$$

where $\hat{n}$ indicates vector normal to the surface inside the cavity. Combining Maxwell's equations, the field inside satisfies the wave equation:

$$\left(\nabla^2 - \frac{1}{c^2} \frac{\partial^2}{\partial t^2} \right) \begin{Bmatrix} \mathbf{E} \\ \mathbf{H} \end{Bmatrix} = 0. \tag{54}$$

Different boundary conditions imposed on the electric and magnetic fields produce two sets of solutions with different eigenvalues. They are denoted as a transverse magnetic (TM) mode and a transverse electric (TE) mode. In the TE mode, $E_z = 0$ where z-axis is the direction of the propagation, but other components of the $\mathbf{E}$ are nonzero, and in the TM mode, $H_z = 0$, but other components of H are nonzero.

Different TM and TE mode solutions are denoted by integer indices as TM_{mnp} and TE_{mnp}. The indices m, n, and p indicate a number of wavelengths along the circumference, diameter, and longitudinal direction. In the simple pill-box cavity, TE mode does not have a longitudinal electric field and cannot accelerate the beams, so they are not used for accelerating cavities. TM_{010} mode is often used for accelerating cavity because it has the lowest eigenfrequency and the longitudinal component of E does not vanish.

An accelerating cavity used in a practical application has an elliptical shape. This shape was optimized from the pillbox cavity to mitigate multipacting [26]. Multipacting is a process in which a large number of electrons are emitted from the wall of the cavity, absorbing the rf power and limiting the performance of the cavity. Those electrons can also be accelerated

by the rf field and eventually impact the cavity wall. When the emitted electrons impact the wall, more electrons may be produced, leading to local heating and thermal breakdown of superconductivity. The field profile in the elliptical shape allows emitted electrons to drift toward the equator where the radial electric field is zero so the emitted electrons do not gain enough energy further produce secondary electrons [26].

3.2 ACCELERATING VOLTAGE

For an electron traveling down the center of the cavity close to the speed of light, the maximum energy gain is achieved if the electron traverses the cavity at one-half of the rf period. For a cavity length of d, this requirement is met when the flight time T_d of the electron through the cavity is given by:

$$T_d = \frac{d}{c} = \frac{\pi}{\omega_0},$$
(55)

where ω_0 is the oscillating frequency of the electromagnetic field. This condition ensures that the electron always sees an accelerating field pointing in the same direction. The accelerating voltage gained by the electron is calculated as

$$V_c = \left| \int_0^d E_z(\rho = 0, z) e^{i\omega_0 z/c} dz \right|,$$
(56)

where $E_z(\rho = 0, z) e^{i\omega_0 z/c}$ is the electric field at the center of the cavity $\rho = 0$ with sinusoidal time dependence $e^{i\omega t}$ with $t = z/c$. The average accelerating electric field or the accelerating gradient that the electron experiences is then

$$E_{acc} = \frac{V_c}{d}.$$
(57)

3.2.1 PEAK SURFACE FIELD

A schematic of the electromagnetic field lines inside the cavity is illustrated in Fig. 6. How much E_{acc} the cavity can deliver depends on the maximum field at the surface of the cavity. The peak surface magnetic field B_{pk} which lies near the equator would quench the cavity when the value exceeds the critical magnetic field or when the surface heats above T_c. The maximum surface electric field E_{pk} near the iris is also important because of the risk of field emission. The ratio E_{pk}/E_{acc} and B_{pk}/E_{acc} are optimized by modifying the cavity geometry.
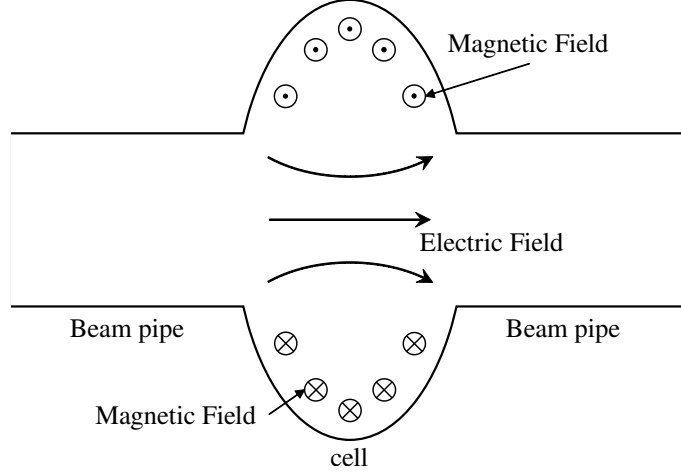
FIG. 6: A schematic of the elliptical cavity with field lines [27]. The surface electric field is strongest near the iris while the surface magnetic field is maximum near the equator region.

3.2.2 QUALITY FACTOR

A figure of merit that characterizes the efficiency of the accelerating cavity is the intrinsic quality factor defined as

$$Q_0 = \frac{\omega U}{P_c}, \tag{58}$$

where ω is the angular frequency of the electromagnetic field, U is the stored energy, and P_c is the power dissipated in the wall of the cavity. The dissipated power is

$$P_c = \frac{1}{2} R_s \int_S |\mathbf{H}|^2 ds, \tag{59}$$

where R_s is the surface resistance of the superconductor and the integration is over the inner surface of the cavity. The time averaged stored energy is

$$U = \frac{1}{2} \mu_0 \int_V |\mathbf{H}|^2 dv, \tag{60}$$

where the integration is over the volume of the cavity. Written in terms of those integrals, Q_0 becomes

$$Q_0 = \frac{\omega \mu_0}{R_s} \frac{\int_V |\mathbf{H}|^2 dv}{\int_S |\mathbf{H}|^2 ds}. \tag{61}$$

Since the ratio of the volume and the surface integral of $\mathbf{H}$ depends only on the shape of the cavity, a constant geometric factor G is defined as

$$G = \frac{\omega \mu_0 \int_V |\mathbf{H}|^2 dv}{\int_S |\mathbf{H}|^2 ds}. \tag{62}$$

Q_0 can now be rewritten as a ratio of G to R_s:

$$Q_0 = \frac{G}{R_s}, \tag{63}$$

which shows that reducing R_s directly improves the efficiency of the SRF cavity.

CHAPTER 4

BASICS OF SUPERCONDUCTING COPLANAR WAVEGUIDE

RESONATOR

4.1 INTRODUCTION

A coplanar waveguide (CPW) is a three-conductor transmission line with a center signal strip and two ground planes deposited on top of a dielectric material as shown in Fig. 7. The
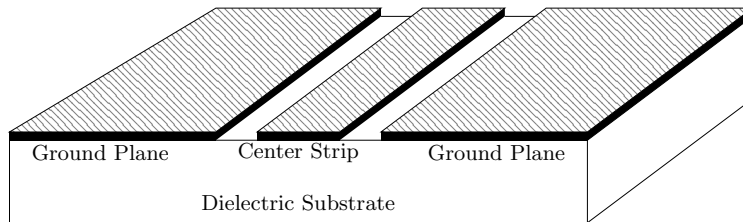
FIG. 7: A simple diagram of the coplanar waveguide.

CPW with an open-ended strip as shown in Fig. 8 creates reflections at both ends, resulting in a standing wave similar to any other resonating cavity, with the fundamental mode equal twice the strip length. The CPW resonators fabricated from Nb films have achieved very high quality factors in the order of 10^6 at $T = 10$–$20\,\mathrm{mK}$ [28, 29]. In addition to the high quality factor, the CPW resonator has advantages over other resonating structures in that only one superconducting film layer is required on top of a dielectric substrate and that the resonators can be fabricated in micron scales using modern lithography techniques. These advantages lead to wide applications including kinetic inductance detectors at millimeter and submillimeter wavelengths [21, 30], qubit devices for quamtum computers [31,
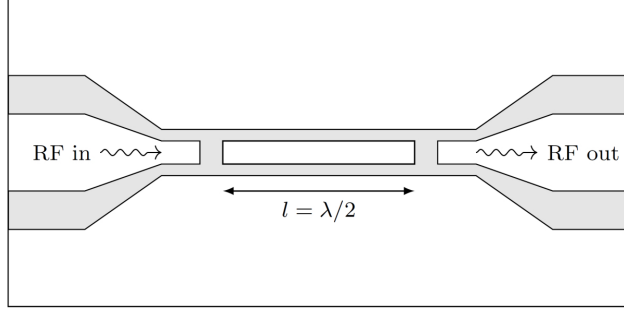
FIG. 8: Top view of the coplanar waveguide resonator with the open-ended circuit on both ends of the center strip. Ground plans are shown on the top and the bottom of the figure.

32], electron spin resonance spectroscopy [33, 34], and characterizations of superconducting properties [35–37].

The properties of the superconducting films can be extracted from measurements of quality factor Q_0 and resonant frequency f_r. The operating frequency of less than $3\,\text{GHz}$ can be achieved in a small sample size of ~ 10 mm, which makes the use of CPW a suitable choice for bench-marking superconducting samples for SRF accelerator applications. The superconducting CPW resonator provides a cost-effective rf measurement, much needed for the development of alternative materials for the Nb SRF cavities [38].

4.2 TRANSMISSION LINE RESONATOR BASICS

A transmission line is designed to carry current at high frequency, where the wavelength may be comparable or smaller than the conductor. Over its length, the voltages and currents vary, and circuit parameters such as capacitance, resistance, and inductance are distributed continuously throughout the line. A simple transmission line can be represented by a two-wire line as illustrated in Fig. 9 along with an equivalent lumped-circuit model of a differential section Δz. The circuit model represents the transmission line in terms of resistance R and an inductance L per unit length of a current-carrying conductor and a capacitance C and shunt conductance G per unit length between conductors.

The transmission line parameters R, L, C, and G characterize a sinusoidal wave traveling along the conductors. The wave traveling along the transmission line is described by $e^{i\gamma x - i\omega t}$
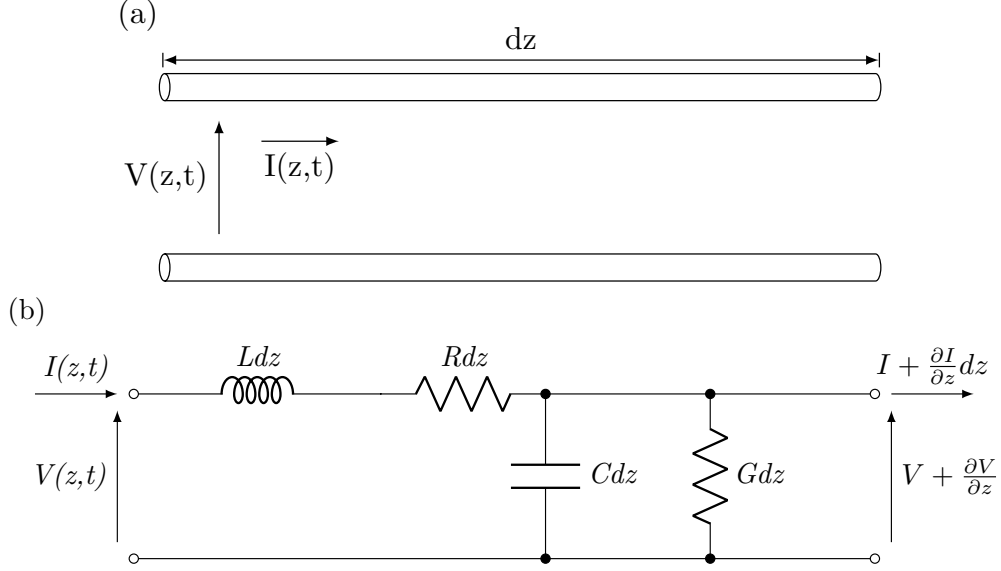
FIG. 9: (a) A parallel two-conductor transmission line; (b) equivalent circuit for differential section dz.

where

$$\gamma = \alpha + i\beta, \tag{64}$$

$$\gamma \approx \frac{1}{2}\sqrt{LC}\left(\frac{R}{L} + \frac{G}{C}\right) + i\omega\sqrt{LC}, \tag{65}$$

where α is the attenuation constant and β is the phase constant [39]. A ratio of amplitudes of the voltage and the current of a wave traveling in one direction is defined as the characteristic impedance of the line Z_c:

$$Z_c = \sqrt{\frac{R + i\omega L}{G + i\omega C}}, \tag{66}$$

where ω is the angular frequency of the wave. For a low loss line with $R, G \ll L, C$ relevant to superconducting transmission lines, Z_c is approximated to

$$Z_c = \sqrt{\frac{L}{C}}. \tag{67}$$

Z_c of the transmission line determines a reflection coefficient for waves traveling from a Z_1 to Z_2 as follows [39]:

$$\Gamma = \frac{Z_2 - Z_1}{Z_2 + Z_2}. \tag{68}$$

Therefore, when connecting two transmission lines, the transmitted power is maximized when the characteristic impedance of the two lines matches.

For a transmission line of length l that is terminated with an arbitrary load impedance Z_L, the input impedance at the beginning of the line is [40]

$$Z_{in} = Z_c \frac{Z_L + iZ_0 \tanh(i\beta l + \alpha l)}{Z_c + Z_L \tanh(i\beta l + \alpha l)}. \tag{69}$$

The open-ended half-wave resonator like the one shown in Fig. 8 is represented with an open circuit at the load or $Z_L = \infty$. The input impedance becomes [40]

$$Z_{in} = Z_c \frac{1 + i\tan(\beta l)\tanh(\alpha l)}{\tanh(\alpha l) + i\tan(\beta l)}. \tag{70}$$

For the resonator, the line length is $l = \lambda/2$ where the wavelength $\lambda = 2\pi v_p/\omega_0$, and the phase velocity $v_p = \omega/\beta$. The propagation constant near the resonant frequency ω_0 can be approximated by setting $\omega = \omega_0 + \delta\omega$:

$$\beta = \frac{\omega}{v_p} \approx \frac{\omega_0}{v_p} + \frac{\delta\omega}{v_p} = \frac{1}{l}\left(\pi + \frac{\delta\omega\pi}{\omega_0}\right). \tag{71}$$

Plugging Eq. (71) into Eq. (69) and assuming small loss $\alpha l \ll 1$, the input impedance of the half-wave transmission line resonator is

$$Z_{in} = Z_c \frac{1 + i\alpha l\delta\omega/\omega_0}{\alpha l + i\pi\delta\omega/\omega_0}, \tag{72}$$

$$\approx \frac{Z_c}{\alpha l + i\pi\delta\omega/\omega_0}. \tag{73}$$

This input impedance can be compared to that of a lumped parallel RLC circuit to obtain an expression for the Q_0. For the RLC circuit illustrated in Fig. 10, the input impedance near the resonance is

$$Z_{in} = \left(\frac{1}{R'} + \frac{1}{i\omega L'} + i\omega C'\right)^{-1}, \tag{74}$$

$$= \frac{R'}{1 + 2i\delta\omega R'C'}, \tag{75}$$

and Q_0 is

$$Q_0 = \omega_0 R'C', \tag{76}$$

where ω_0 is

$$\omega_0 = \frac{\pi}{l\sqrt{LC}}. \tag{77}$$

Comparing Eq. (69) and Eq. (75), R' and C' expressed in terms of transmission line parameters are

$$R' = \frac{Z_c}{\alpha l},\tag{78}$$

$$C' = \frac{\pi}{2\omega_0 Z_c},\tag{79}$$

and the Q_0 is then

$$Q_0 = \omega_0 R' C' = \frac{\pi}{2\alpha l}.\tag{80}$$

Now, substituting $\alpha \approx \frac{1}{2}\sqrt{LC}\frac{R}{L}$ and $l = \frac{\pi}{\beta} \approx \frac{\pi}{\omega_0\sqrt{LC}}$, Q_0 in terms of the distributed transmission line parameters is

$$Q_0 = \frac{\omega_0 L}{R}.\tag{81}$$
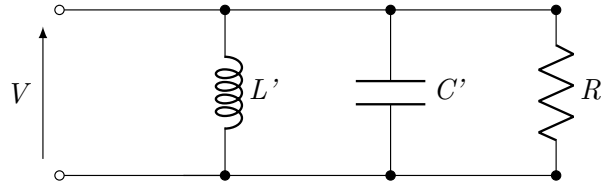
FIG. 10: A lumped circuit model of the parallel RLC circuit.

4.3 ANALYTICAL CALCULATIONS OF CPW PARAMETERS

To analytically calculate the distributed inductance L and capacitance C, the superconducting CPW is treated as a perfect conductor, and the geometric inductance L_g and the geometric capacitance C_g are calculated first. The effect of superconductivity, in particular, the kinetic inductance L_k can be calculated separately and added to yield the total inductance $L = L_g + L_k$. The geometric inductance and capacitance for the CPW are calculated assuming quasi-static approximation. In this regime, the parameters are obtained by

solving electro- and magneto-static problems based on the cross-sectional geometry of the CPW assuming the structure hosts a pure-TEM mode. In reality, a pure-TEM mode cannot propagate in the CPW since the conductors are deposited on a substrate with dielectric constant ϵ_r and the top half is exposed to vacuum or air. Part of the waves traveling in the air will have the velocity c while the waves in the dielectric will travel with velocity $c\sqrt{\epsilon_r}$. The difference in the wave speed produces longitudinal field components $\mathbf{E_z}$ and $\mathbf{H_z}$ along the length of the CPW [41]. Therefore, the CPW supports propagation of quasi-TEM mode at low frequencies and more TE-like at higher frequencies [42]. At low frequencies, treating the quasi-TEM mode as a pure-TEM provides a good approximation for calculating transmission line parameters when the transverse components of the waves $\mathbf{E_T}$ and $\mathbf{H_T}$ are much greater than $\mathbf{E_z}$ and $\mathbf{H_z}$. A condition that makes this approximation valid is [43]

$$w \ll \frac{1}{f_r\sqrt{\mu\epsilon}}, \tag{82}$$

where μ and ϵ are the permeability and the permittivity of the substrate, w is the width of the center conductor, and f_r is the operating frequency. For example, a CPW resonator operating at $f_r = 1 - 3\,\mathrm{GHz}$ deposited on sapphire has $\epsilon \sim 10\epsilon_0$ and $\mu = \mu_0$. With these parameters, the quasi-static approximation is valid for $w \ll 10^{-2}$ m.

In the quasi-static approximation, the transmission line parameters are calculated by solving the 2D Laplace's equation of the CPW geometry. The cross-sectional geometry of the CPW is shown in Fig. 11 where w is the center strip width, s is the gap width between the strip and the ground planes, t is the thickness of the strip, h is the dielectric substrate thickness, and ϵ_r is the dielectric constant of the substrate. To simplify the calculation of Laplace's equation, a conformal mapping technique is used to map the boundaries of the CPW into a simpler shape for which the solution can be found easily. A detail of the transformation is given in Appendix A. For $t \ll w$, the geometric inductance and capacitance are [40]

$$L_g = \mu_0 \frac{K(k')}{4K(k)}, \tag{83}$$

$$C_g = \frac{1 + \epsilon_r}{2}\epsilon_0 \frac{4K(k)}{K(k')} = \epsilon_e\epsilon_0 \frac{4K(k)}{K(k')}, \tag{84}$$

where $k = w/(w + 2s)$, $k' = \sqrt{1 - k^2}$, and $K(k)$ is the complete elliptic integral of the first kind. The characteristic impedance is

$$Z_c = \frac{L}{C} = \frac{Z_0 K(k')}{4\sqrt{\epsilon_e}K(k)}, \tag{85}$$
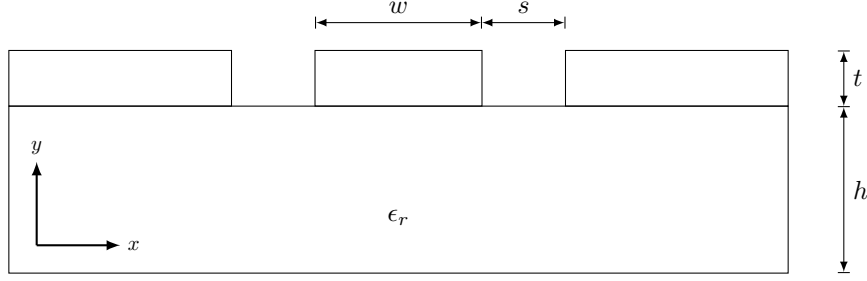
FIG. 11: Coplanar waveguide with important dimensions.

where $Z_0 = \sqrt{\mu_0/\epsilon_0}$.

The kinetic inductance L_k can be approximated with an analytical formula in a limiting case. For a wide center strip, $w \gg t$, the magnetic fields on the top and bottom surface of the center strip are equal to H_0 at the upper side and $-H_0$ at the bottom side. In such a case, the field inside the strip can be calculated analytically to be

$$H_x = H_0 \frac{\sinh(y/\lambda)}{\sinh(t/2\lambda)}, \tag{86}$$

where x is the direction across the width and y is the direction parallel to the thickness of the strip. The superconducting strip is defined over $-w/2 < x < w/2$ and $-t/2 < y < t/2$. In this configuration, the current density $\mathbf{J}$ inside the strip can be calculated analytically using the Ampére's Law, and the kinetic inductance is determined by equating the stored magnetic energy $\frac{1}{2}L_k I^2$ with the kinetic energy of the Cooper pairs:

$$\frac{1}{2}L_k I^2 = \frac{1}{2}\int_s \mu_0 \lambda^2 |\mathbf{J}|^2 dS, \tag{87}$$

where the integral is over the cross-section area of the center strip. The resulting kinetic inductance is then [44, 45]

$$L_k = \frac{\mu_0 \lambda}{2w} \coth\left(\frac{t}{2\lambda}\right). \tag{88}$$

In two cases where $t \ll \lambda$ and $t \gg \lambda$, L_k can be well approximated as

$$L_k \approx \begin{cases} \dfrac{\mu_0 \lambda^2}{wt}, & t \ll \lambda, \\ \dfrac{\mu_0 \lambda}{2w}, & t \gg \lambda. \end{cases} \tag{89}$$

4.4 NUMERICAL ANALYSIS OF R AND L

When characterizing only λ of the superconducting thin film, it is convenient to calculate L_k using the analytical formula in Eq. (88). However, to extract both R_s and λ from the measurements of the CPW, it is useful to rely on numerical analysis to calculate the distributed parameters R and L as a function of superconducting properties. R and L are calculated from the geometry of the CPW and the complex conductivity $\sigma = \sigma_1 - i\frac{1}{\omega\mu_0\lambda^2}$. This numerical method was first developed by Weeks [46] and was later adopted for a superconducting CPW by Porch [47].

In this method, a cross-section of the CPW geometry is divided into N smaller patches, with a higher concentration of patches near the edges of the conductors where the current varies rapidly, as shown in Fig. 12. Each patch is assumed to behave as a separate transmission line but is coupled to each other so that the energy from one patch to another is coupled by proximity. The system then obeys the coupled transmission line equation:

$$\frac{-\partial v_n}{\partial z} = \sum_{m=1}^{N} (r_{mn} + i\omega l_{mn}) \, j_m, \tag{90}$$

where v_n and j_m are the voltage and current on nth and mth patch, and r_{mn} and l_{mn} are the resistance and inductance matrices of the patches. The current is assumed to be uniform on
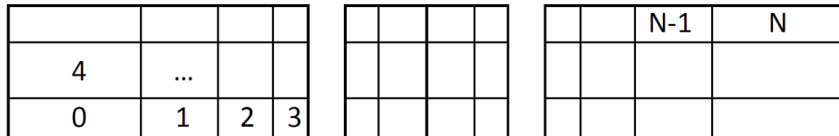
FIG. 12: A cross-section of a CPW is divided into N patches. Smaller patches are located along the edges where the current varies over the penetration depth.

the individual patches and runs along the z-axis. Each resistance term is given by

$$r = \mathrm{Re}\left(\frac{1}{\sigma A}\right), \tag{91}$$

where A is an area of an individual patch and σ is the complex conductivity. The inductance term consists of a sum of the kinetic inductance and the geometric inductance that includes both the mutual and external inductance between patches. The kinetic inductance part is given by

$$l = \frac{1}{w}\mathrm{Im}\left(\frac{1}{\sigma A}\right). \tag{92}$$

The geometric inductance between patches is calculated using an analytical formula derived from the stored energy concept by Weeks [46]. Given the complex conductivity, the impedances r_{mn} and l_{mn} are calculated, and the current distributions inside the CPW are calculated by inverting Eq. (90). Once the current on each patch is calculated, the distributed R and L are calculated as

$$R = \frac{1}{I_{tot}^2}\sum j_n^2 r_n, \tag{93}$$

$$L = \frac{1}{I_{tot}^2}\sum_{mn} j_m j_n l_{mn}. \tag{94}$$

This algorithm was implemented in MATLAB® codes by Mateu [48].

4.5 DIELECTRIC AND RADIATION LOSS

In addition to the intrinsic Q_0 that probes the conductor rf losses of the CPW, the measured quality factor includes losses in the dielectric substrate and radiation losses. Additionally, any energy dissipated into external input and output ports is represented as external quality factor Q_{ext}. The total quality factor or the loaded quality factor Q_L is then

$$\frac{1}{Q_L} = \frac{1}{Q_0} + \frac{1}{Q_d} + \frac{1}{Q_r} + \frac{1}{Q_{ext}}, \tag{95}$$

where Q_d and Q_r are the dielectric and the radiation quality factor respectively. The losses from dielectric and radiation should be minimized in designing the CPW resonator so that the measured Q_L are not influenced by the parasitic losses. From Eq. (80) and Eq. (81), the dielectric quality factor can be expressed in terms of the attenuation constant of the dielectric substrate α_d:

$$Q_d = \frac{\beta}{2\alpha_d} = \frac{\omega\sqrt{LC}}{2\alpha_d}. \tag{96}$$

The approximate formula for α_d when $t \ll w$ is calculated in Ref. [40] as:

$$\alpha_d = \frac{\pi}{2\lambda_0} \frac{\epsilon_r}{\sqrt{\epsilon_e}} \tan \delta_l, \tag{97}$$

where ϵ_r is the dielectric constant, $\epsilon_e = (1+\epsilon_r)/2$, λ_0 is the free space wavelength, and $\tan \delta_l$ is the loss tangent of the dielectric substrate.

The radiation quality factor is estimated by calculating the total power radiated by the electric field. When $\lambda \ll t$, currents are concentrated at the edges of the strip and the ground planes, and the current distribution can be estimated as simple current-carrying wires located at the edges of the conductors. In such case, the radiation quality factor is approximated as [19]

$$Q_r \approx \frac{2.49}{n^4} \frac{Z_c'}{Z_0} \frac{l^4}{s^2(s+w)^2}, \tag{98}$$

where n is the mode number, Z_c' is the characteristic impedance of the CPW in the absence of the dielectric substrate, l is the length of the resonator, and $Z_0 = 377\,\Omega$ is the impedance of free space. In the other limit where $\lambda \gg t$, the current is approximated as nearly constant on the strip and decays away exponentially on the ground planes with $\sim \lambda$. The Q_r is then reduced by factor ν compared to Eq. (98) [19]:

$$\nu \approx \left[1 + \left(\frac{12\lambda^2 + 6\lambda(2s+w) + w^2}{6s(s+w)}\right)\right]^2. \tag{99}$$

CHAPTER 5

NITROGEN-DOPED CAVITY CHARACTERIZATION

5.1 INTRODUCTION

Over the last few years, much progress has been made on building superconducting rf resonators with high quality factors. Achieving high values of Q_0 could mean a substantial reduction in the operational cost of an accelerator. A discovery to anneal Nb cavities in the presence of nonmagnetic impurities such as titanium, nitrogen, and oxygen has shown suppression of the surface resistance up to $\sim 50\%$–70% as the peak magnetic field increases from 0 to $\lesssim 0.5 H_c$ [1, 2, 49, 50]. Although the impurity-treated cavities have shown to reach higher Q_0, they are limited by quench fields almost 40% lower than the conventional typically treated cavities [2, 49, 51, 52]. In an attempt to understand the quenching mechanism of the doped cavities, an array of thermometers was used to map the temperatures of the outer surface of the cavities while increasing the field. To get an insight into the mechanism by which the field-induced reduction in $R_s(H)$ occurs, coupons from the nitrogen-doped cavity have been studied using a scanning tunneling microscope (STM) to measure the local density of states (DOS) at the surface. This chapter presents methods and results of temperature mappings of the nitrogen-doped cavity and the STM results and analysis of coupons using a theoretical model of the superconducting DOS. This chapter is based on the research publications Refs. [51, 53].

5.2 NITROGEN DOPING OF SRF CAVITIES

Nitrogen doping of the SRF cavity is the process of diffusing nitrogen into the surface of Nb and later removing several microns from the inner surface. The first necessary step is the high-temperature heat treatment at $800\,^\circ$C for approximately three hours in a high vacuum furnace. This process helps reduce the concentration of hydrogen in the niobium that could otherwise form lossy hydrides at the surface [54]. High purity nitrogen gas is then injected at a partial pressure of around $25\,$mTorr for 30 minutes. After the nitrogen gas is removed, the cavity is further annealed at $800\,^\circ$C for 30 minutes before cooling down to room temperature. The final crucial step involves electropolishing (EP) to remove a thin N-rich

layer from the inner surface of the cavity. The EP involves forming an electrolytic cell with an aluminum rod as a cathode and the niobium cavity as an anode. The electrolyte consists of a mixture of HF (49%) and H_2SO_4 (96%) in a volume ratio of nine to one [52, 55]. The electrolysis induces a formation of Nb_2O_5 on the surface which is then dissolved by HF. At the end of the process, approximately 10–35μm of the inner surface is removed.

The nitrogen-doped cavities measured in this study were fabricated from ingot niobium from Tokyo Denkai, Japan with a residual resistance ratio (RRR) of around 300 with a large grain size of a few cm^2. They are 1.3 GHz single-cell cavities with a TESLA/XFEL center cavity shape [56]. Two cavities of this type labeled TD3 and TD4 were tested with a temperature mapping system. Those two cavities differed only in the final step of N-doping, where $\sim 35\,\mu$m was removed from the inner surface of TD3, and $\sim 10\,\mu$m was removed from TD4 using EP.

For a comparison, an additional cavity was prepared using a conventional procedure without the nitrogen treatment and tested with the temperature mapping. This cavity labeled A2 was made with ingot niobium from Companhia Brasileira de Matalurgia e Mineração (CBMM), with the RRR of the niobium reaching around 260. The cavity had gone through a typical treatment of buffered chemical polishing (BCP) and high-pressure rinsing. BCP is a process of removing $\sim 200\,\mu$m of damaged inner layer that resulted from the mechanical fabrication of the cavity and ~ 20–$50\,\mu$m of lossy Nb layer contaminated from impurities during high-temperature heat treatment [57]. A mixture of HF, HNO_3, and H_3PO_4 are used in the BCP process which is one of the typical treatments for the niobium cavities before testing [57].

5.3 CAVITY TEST RESULTS

Figure 13 shows a plot of $Q_0(B_p)$ for the BCP treated standard cavity A2 and two nitrogen-doped cavities TD4 and TD3 at 1.6 K. Each nitrogen-doped cavities were tested twice where they were warmed to 80–100 K and cooled down at different rates between tests. During the experiments, the residual magnetic field inside the cryostat was around 2 mG. The temperature was monitored at the middle and at the bottom of the dewar, and the rates at which the sensor crossed 9.2 K were recorded. For both cavities, the slow cooldown rate was approximately 25 mK/sec and the fast cooldown rate was around 90 mK/sec. A cavity is cooled down by filling the dewar with liquid helium which starts at the bottom; consequently, a faster cooldown creates a larger thermal gradient across the cavity compared to a slower cool down. Both cavities exhibited better performance after faster cooldown rates. The Q_0

of the TD3 and TD4 increased by approximately 59% and 83% at $B_p \sim 60\,\mathrm{mT}$ respectively, compared to the "slow" cooldown. The observed performance boost of the N-doped cavities by the faster cooldown is consistent with a model proposed by [58], in which the number of trapped vortices is calculated to be an inverse of the spatial temperature gradient across the cavity. The faster cooldown produced a more favorable condition for the expulsion of the residual ambient magnetic field, which resulted in lower residual resistance and thus higher Q_0. This result is also in agreement with other nitrogen-doped cavity measurements comparing different cooldown rates [59, 60].

TD3 reached the breakdown field of $\sim 130\,\mathrm{mT}$ while TD4 cavity quenched at $\sim 88\,\mathrm{mT}$. On the other hand, Q_0 of the TD4 cavity was almost three times as large as the Q_0 of the TD3 cavity for both cool down rates. At faster cooldown rates, TD3 and TD4 reached $Q_0 \sim 4.8 \times 10^{10}$ and $Q_0 \sim 1.3 \times 10^{11}$, and at slower cool down rates Q_0 at the breakdown fields of TD3 and TD4 were 2.8×10^{10} and 8.1×10^{10} respectively. The results show that material removal after nitrogen doping increases the accelerating gradient at an expense of quality factors. The performance of the TD3 cavity during the fast cool down is similar to that of the standard A2 cavity up to $B_p \sim 90\,\mathrm{mT}$, but the Q_0 of the A2 degraded rapidly beyond this point, a phenomenon exhibited commonly for the BCP-treated cavity known as Q-drop [26].

The error bars in the plot of $Q_0(B_p)$ are the combined systematic errors from the cable attenuation, fit of decay time constant, and the measurements from power meters. The attenuation constants of the cables used in the cavity tests were measured using a portable power meter with a relative error of around 4–5%. The decay time constant is the time it takes for the stored energy inside the cavity to fall by $1/e$. This is calculated by fitting the transmitted power signal from the cavity to an exponential function after turning off the rf power. The relative error in the decay constant after combining the fit error and the instrumental error was approximately 4%. The relative errors for power meters were approximately 5%. Finally, the propagated relative errors for Q_0 and B_p were around 15% and 6% respectively.

5.4 TEMPERATURE MAPPING

The temperature mapping is a useful tool to measure the change in temperature on the outer surface of the cavity caused by rf heating. A total of 576 thermometers cover the surface of the cavity to identify the locations of local heating and quench locations. The temperature mapping was used to understand the origin of the quench in nitrogen-doped
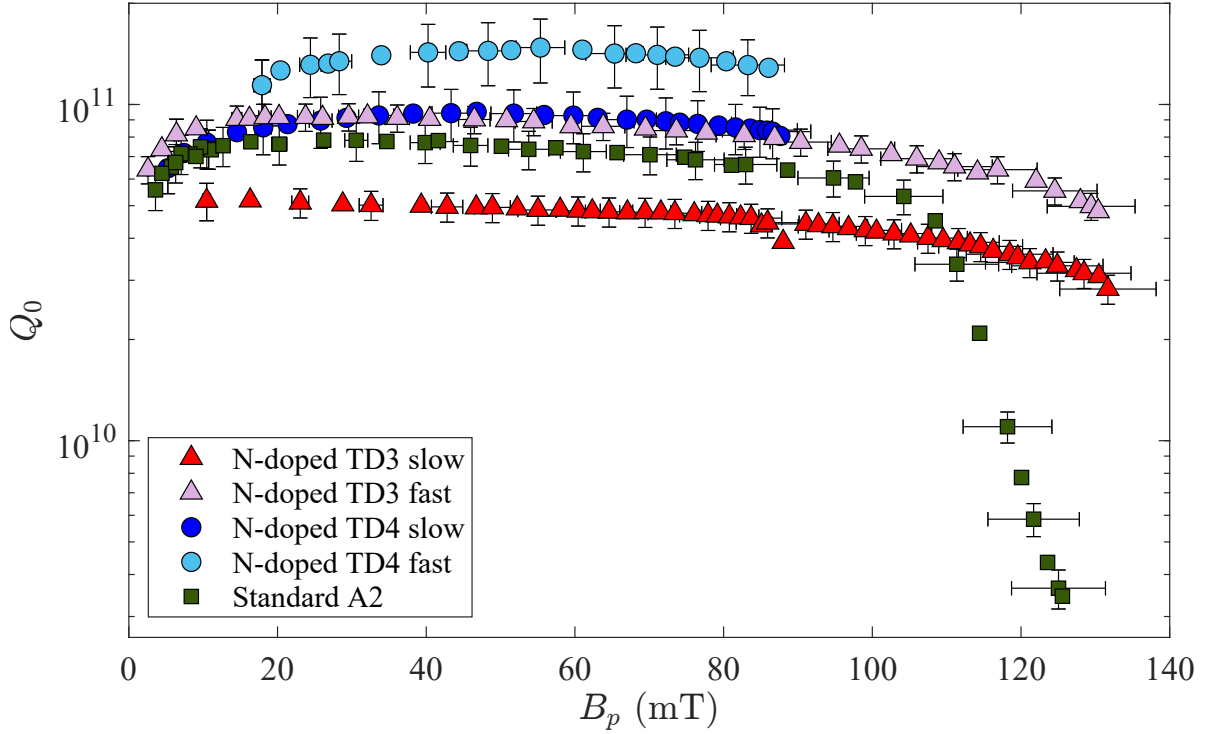
FIG. 13: Q_0 vs B_p at $1.6\,\mathrm{K}$ of the standard cavity A2 and two nitrogen-doped cavities TD3 and TD4 with different cooldown rates. The amount of inner surface removed following the nitrogen diffusion was $\sim 30\,\mu\mathrm{m}$ for TD3 and $\sim 10\,\mu\mathrm{m}$ for TD4. Slow and fast refer to a cool-down rate of $\sim 25\,\mathrm{mK/sec}$ and $\sim 90\,\mathrm{mK/sec}$.

cavities, and also to identify the "cold spots" and "hot spots" to conduct a surface study. "Cold spots" are regions that exhibited minimal heating compared to "hot spots" where strong rf heatings were observed.

The temperature mapping system consists of 36 arrays of printed-circuit boards each containing 16 thermometers fixed around the outer cavity surface. The device is based on a design developed at Cornell [61]. The thermometers are $100\,\Omega$ carbon Allen-Bradley resistors, whose resistance increases nearly exponentially with decreasing temperature, below $4.3\,\mathrm{K}$. The boards run azimuthally around the cavity with a $10\,^\circ$ separation, and each resistor on the board is labeled from 1 to 16, with the resistor 1 at the top iris of the cavity, 8 at the equator, and 16 at the beampipe. The circuit boards are designed to match the contour of the cavity, and each thermometer is mounted on a pogo stick to ensure the sensor remains in contact with the outer surface of the cavity during testing at a cryogenic temperature. Each sensor probes a surface area of $\sim 0.4\,\mathrm{cm}^2$, with a temperature resolution of $\lesssim 1\,\mathrm{mK}$. Figure 14 shows a cavity dressed with the temperature mapping system.

FIG. 14: A single-cell cavity with a partially attached thermometry system.

The temperature maps measured on the TD4 cavity at $B_p \approx 83\,\text{mT}$ for both slow and fast cooldown tests are shown in Fig. 15. The color map shows the temperatures on the outer surface of the cavity with respect to the helium bath temperature, where the x- and the y-axis correspond to an azimuthal angle around the cavity and the thermometer numbers respectively. A maximum heating of around 5–6 mK was measured during the slow cooldown. During the fast cooldown, the magnitude of the heating dropped significantly compared to the slow cooldown. The spots that exhibited 5–6 mK of heating in the slow cooldown only showed 1–2 mK of heating after the fast cooldown. Most of the heating is located in the equator regions for both cooldowns, but it can be observed that some hot spots that were there during the slow cooldown are gone in the fast cooldown, and there is a slight variation in the spatial distribution of the heat maps. The fact that the nature of the hot spots can change between different cooldown rates indicates that they are most likely caused by trapped flux during the cooldown [62]. A comparison of the temperature maps during the slow and fast cooldown suggests that fewer vortices were trapped during the fast cooldown, resulting in reduced losses in the cavity, as was also evident from the results of $Q_0(B_p)$ in Fig. 13.

The temperature maps recorded during the quench reveal the possible location that ignited the quench. Figure 16 (a) shows the temperature maps of the TD3 cavity during the actual quench and Fig. 16 (b) shows the heat map measured right below the quench field. A spot that showed the highest temperature rise during quench is circled. Importantly, the quench spots show no evidence of strong pre-heating before quench, only reaching max $\Delta T(B_p) \sim 15\,\text{mK}$ in the nearby area.

Figure 17 shows $\Delta T(B_p)$ as a function of T at the quench locations for the TD3 and the TD4 cavities and one of the hot spots of the A2 cavity for comparison. The lack of precursor heating in the quench spot is further evident from the plot. While the hot spot on the A2 cavity shows temperature rising quadratically with the field up to 500 mK, the heating on the hot spots on TD3 and TD4 cavities remains below $\sim 15\,\text{mK}$ prior to quenching. This suggests that the quenches for the nitrogen-doped cavities are not caused by thermal breakdown. In fact, a thermal breakdown is caused by a resistive defect or a region of weaker superconductivity, particularly near the equatorial high field region, where the heat from ohmic losses raises to above $\sim \frac{T_0}{\Delta}$ leading to thermal runaway instability and quench [63, 64]. Based on the temperature mapping studies, it is most likely that the nitrogen-doped cavities quench early due to the magnetic flux entry. The quench occurs near the equator where the surface magnetic field is the highest and is ignited without any significant precursor
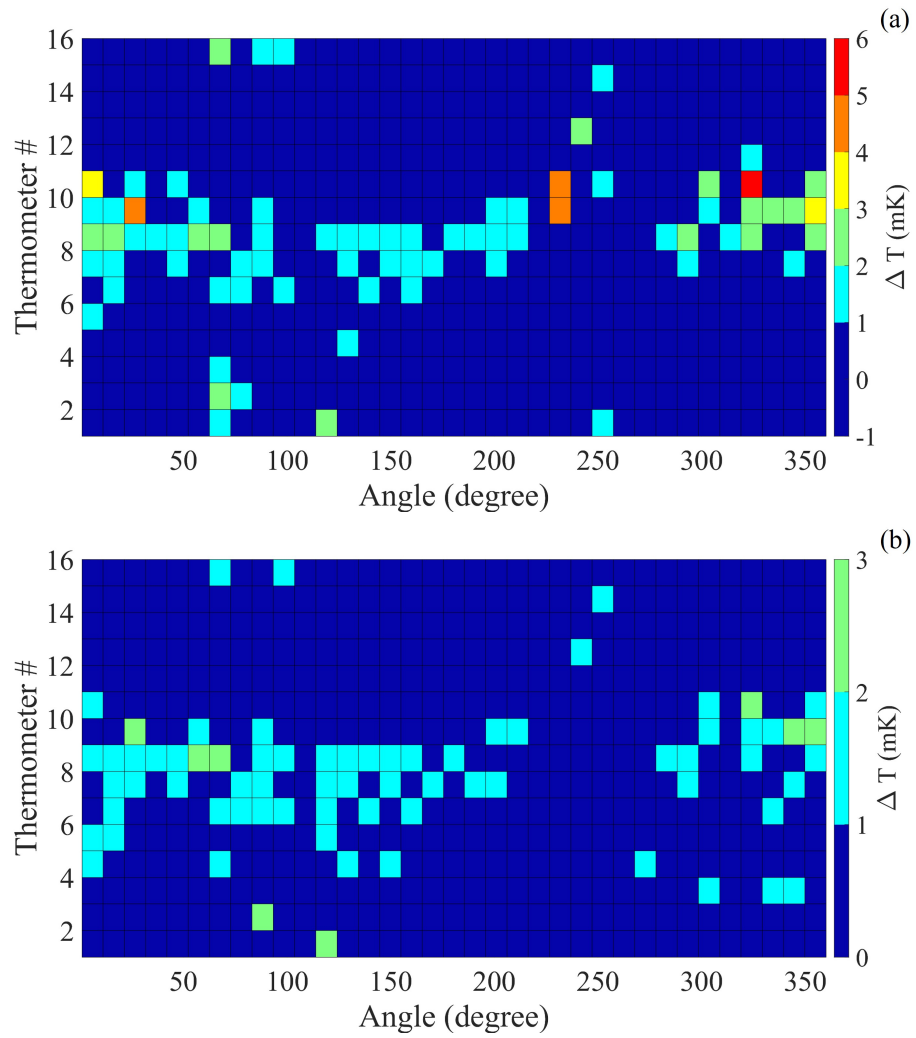
FIG. 15: The temperature maps recorded on TD4 cavities for the (a) slow cooldown and (b) fast cool down at the field slightly below the quench field.

heating. This observation suggests that the lower critical magnetic field H_{c1} is reduced on the surface by the impurity infusion. A comparison of the quench fields of the TD3 and the TD4 cavity shows that removal of the inner surface exposes a cleaner Nb surface and the H_{c1} can be recovered at an expense of reduced Q_0. Further investigation is necessary to fully understand how the nitrogen doping degrades the critical magnetic field, and the results also suggest for a systematic study on the amount of material removal for optimal performance.

5.5 DENSITY OF STATES STUDY WITH STM

To get an insight into the improved performance of the nitrogen-doped cavities, several coupons were cut from TD4 and A2 cavities, and their surface was studied extensively with Scanning Tunneling Microscopy (STM). The goal of the experiment is to identify which superconducting properties are modified by the nitrogen-doping that leads to unconventional field-induced reduction of the surface resistance. This phenomenon was observed up to $B_p \sim 60\,\mathrm{mT}$ for the nitrogen-doped TD4 cavity during the fast cool down as shown in Fig. 13.

The behavior of the nonlinear surface resistance is manifested by the physics of nonlinear superconductivity and pair-breaking rf currents on the first few nanometers at the surface. Subtle material features and impurity distributions within this layer play an important role in creating the field-induced reduction in R_s. It has been shown that smearing of the peaks which appear at the edge of the gap in the superconducting density of states (DOS) can result in a reduction of R_s by pair breaking currents [65], in agreement with experiments [49, 66]. It shows that the current induced reduction in R_s can be enhanced by engineering an optimum broadening of the peaks. Such broadening of the gap peaks can be current induced [23, 65, 67, 68], or due to paramagnetic impurities [69], or a proximity-coupled normal layer due to nonstoichiometry and metallic suboxide layers [70, 71]. The latter is relevant to the Nb surface which is covered in several nanometer thick oxide and suboxide layers. The oxide layer of Nb consists mainly of insulating Nb_2O_5 with a few nm thick metallic NbO and semiconducting NbO_2 at the interface between the oxide and the metallic Nb [72, 73].

The tunneling experiments can directly probe the local density of states, and the STM was used to probe how nitrogen doping changes the local DOS. Whatever the origin of the pair-breaking mechanism is, a simple phenomenological Dynes formula [74, 75] can be used to analyze the DOS with broadened peak:

$$\frac{N_s(E)}{N_n(0)} = \mathrm{Re}\frac{E + i\Gamma}{\sqrt{(E + i\Gamma)^2 - \Delta^2}}, \tag{100}$$
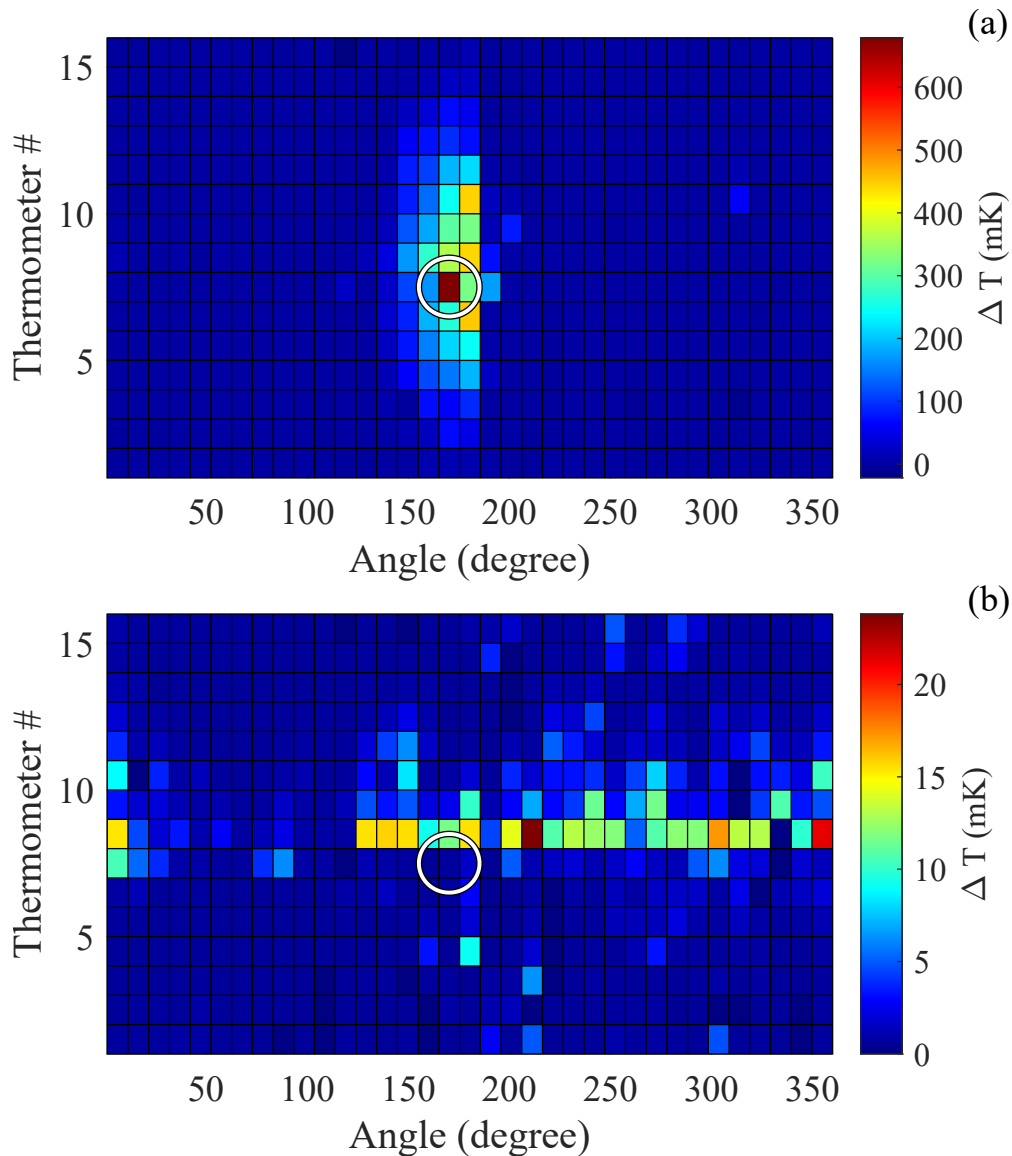
FIG. 16: (a) Temperature map during the quenching for the TD3 cavity. The x-axis is the azimuthal angle around the cavity and the y-axis is the thermometer number indicating the longitudinal positions where thermometer # 8 is located at the equator. The spot that exhibited the highest heat signature is the quench location and is marked with a circle. (b) The temperature map right before the quench shows that the location that ignited the quench shows negligible heating before the event.
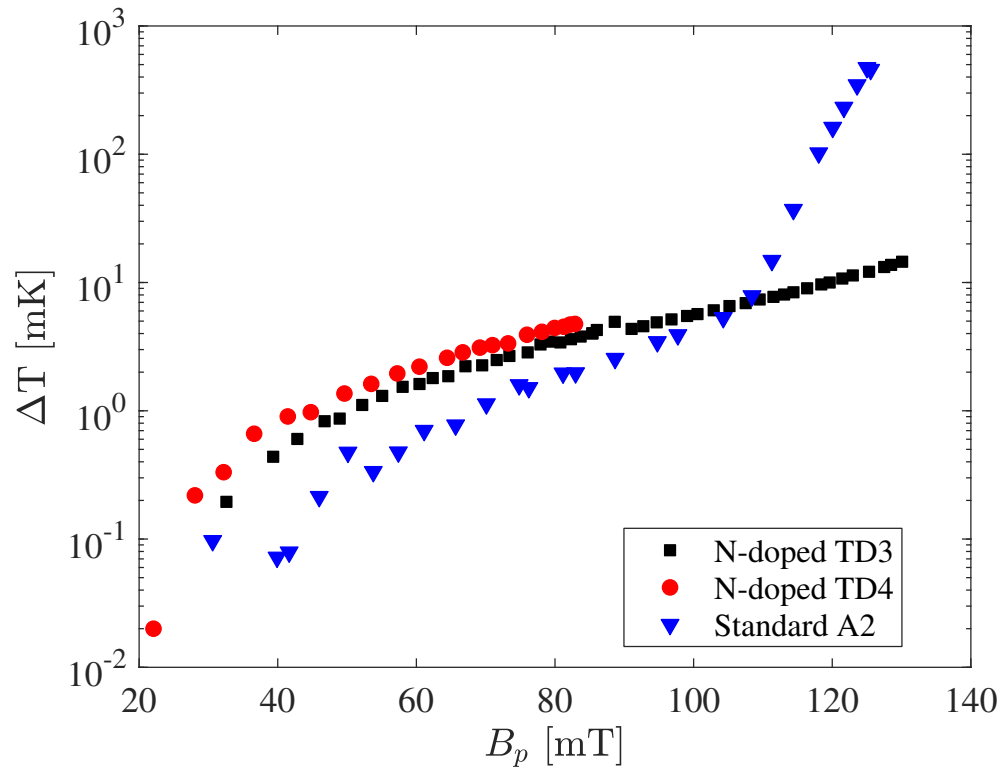
FIG. 17: A change in temperature as a function of peak magnetic field measured at the quench locations for the two nitrogen-doped cavities and one of the hot spots near the equator for the standard treated cavity.

where Γ is a parameter that describes a finite lifetime of the quasiparticles at the gap edge. Irrespective of the microscopic origin of the pair-breaking mechanism, this results in a smearing of the gap edge and finite quasiparticle states for $E < \Delta$. The collected tunneling spectra are fit with this Dynes formula and Δ and Γ are calculated. These parameters give insights into the mechanism of the nonlinear surface resistance. For instance, the number of quasiparticles decreases exponentially with $R_s \propto e^{-\Delta/k_B T}$, and with $\Gamma > 0$, there are finite states below $E < \Delta$ that are excited by the rf field. These subgap states exist even when $T = 0$ and contribute to $R_s(T)$ in a form of residual resistance R_i that is weakly dependent on temperature [23, 70]. On the other hand, the smearing of the gap peak by width $\sim \Gamma$ acts to reduce $R_s(T)$ at a higher temperature where R_i becomes negligible. The contribution of Γ in $R_s(T)$ appear in the logarithmic term in Eq. (47) where $\hbar\omega$ is now replaced by Γ when $\Gamma > \hbar\omega$ [23, 66, 70]:

$$R_s \propto \ln\left(\frac{k_B T}{\Gamma}\right). \tag{101}$$

The broadening of the peaks reduces $R_s(T)$, and the same can occur with a current-induced broadening. The oscillating rf field also smears out the peak, and if the width of the new peak exceeds $\hbar\omega$ and Γ, the logarithmic term gets replaced by

$$R_s(B) \propto \ln\left(\frac{T B_c^{4/3}}{T_c B^{4/3}}\right), \tag{102}$$

where B is the field on the surface and B_c is the critical field [66, 70]. Hence, $R_s(B)$ can be reduced by B.

In addition to the phenomenological Dynes formula, another model that incorporates the effect of an imperfect surface is used to analyze the data. The model developed by A. Gurevich and T. Kubo [58, 70] includes a realistic surface that contains a thin layer of a normal metal with reduced superconductivity. The theory is based on the Usadel equations [76] for the proximity-coupled normal and superconducting bilayers. In calculating the DOS, additional dimensionless parameters are introduced:

$$\alpha = \frac{d N_n}{\xi_S N_S}, \tag{103}$$

$$\beta = \frac{4e^2}{\hbar} R_B N_n \Delta d, \tag{104}$$

where d is the thickness of the normal layer, ξ_s is the coherence length of the bulk superconductor, N_n and N_s are the normal state DOS at the Fermi level for the normal and superconducting layer, and R_B is the contact resistance between the normal and superconducting

(N-S) layer. In essence, α quantifies the thickness of the normal layer, and β quantifies the transparency of the N-S interface. There is an optimal value for β given a specific α such that R_s is minimized due to a complex interplay of two effects that influences the R_s [70]. An increase in contact resistance between the N-S bilayer leads to a weakened proximity effect in the N layer; thus, increasing R_s. On the other hand, the proximity coupled normal layer also broadens the gap peaks, which replaces $\hbar\omega$ in the logarithmic term and reduces R_s. The purpose of the DOS measurement is to identify the mechanism by which nitrogen doping increases the performance by probing the electronic states both at the surface and in the bulk.

5.6 STM BASICS

Scanning Tunneling Microscope measures a tunneling current between a sample and an atomically sharp tip. The tunneling current decays roughly exponentially between the tip and the sample, and in STM measurements the potential barriers are often a few nanometer thick vacuum. When the tip is near the sample, there is a finite probability for an electron to tunnel from one conductor to an empty state of another conductor. When a bias voltage is applied between the tip and the sample, the measured current as a function of the voltage gives information about the density of states of a sample. Based on Bardeen's tunneling theory and Fermi's golden rule the current as a function of the bias voltage V between the normal tip and the superconducting sample is given as [77, 78]

$$I_{ns}(V) = \frac{2\pi e}{\hbar} \int_{-\infty}^{\infty} |M|^2 N_{1n}(E + eV) N_{2s}(E) \left[f(E) - f(E + eV) \right] dE, \qquad (105)$$

where E is energy measured from Fermi energy E_F, $f(E)$ is the Fermi function, N_{1n} is the DOS of the tip, N_{2s} is the superconducting DOS of the sample, and $|M|$ is Bardeen tunneling matrix given by [77, 79]

$$M = \frac{\hbar^2}{2m} \int \left(\psi_{tip} \nabla \psi_{sample}^* - \psi_{sample}^* \nabla \psi_{tip} \right) \cdot dS, \qquad (106)$$

where ψ_{tip} and ψ_{sample} are the wave functions of the tip and the sample, and the integral is over a separation surface between the tip and the sample. This tunneling matrix and the normal conductor DOS are nearly constant in energy near the Fermi level and are moved outside the integral [77]. Taking the derivative of the current with respect to the bias voltage gives

$$\frac{dI}{dV} \propto \int_{-\infty}^{\infty} N_{2s}(E) \frac{d}{dV} \left[f(E) - f(E + eV) \right] dE. \qquad (107)$$

The derivative $df/dV =$ is a peak function if width $\sim k_B T$ at the energy $E = eV$. If $k_B T \ll \Delta$, the slowly varying $N_{2s}(E)$ can be taken out of the integral and the STM gives a direct measurement of the superconducting DOS:

$$\frac{dI}{dV} \propto N_{2s}(eV). \tag{108}$$

In a measurement dI/dV are taken into account by calculation of the integral (107) numerically to extract $N_{2s}(E)$ from the STM data.

5.7 STM EXPERIMENTAL DETAILS

The cold spots from the nitrogen-doped and the standard cavities were measured with low-temperature STM to identify differences responsible for performance increase. Figure 18 shows the temperature maps recorded right before the quenching and the locations where the coupons were cut out. Coupons of size 8 mm × 8 mm were cut out from the cavity using a CNC milling machine with no lubricants. A steady flow of compressed helium was applied to the drilling region to prevent the sample from heating. The temperature was monitored throughout the process using an infrared thermometer to make sure it did not rise above $32\,°\text{C}$. To verify that this cutting process does not introduce any impurities, a larger 16 mm × 16 mm coupon was cut out first, and the surface was analyzed with the Time-of-Flight Secondary Ion Mass Spectroscopy (TOF SIMS). The measurement was repeated near the same location after cutting out a smaller coupon of size 8 mm× 8 mm. The analysis showed some increase in carbon concentration but did not show any new impurities after the cutting.

The cold samples from TD4 had shown no detectable heating, and their locations were $0°$ and $50°$ from the equator. All the samples from the A2 cavity had shown higher heating compared to the TD4 cavity, and they were cut from locations $20°$ and $40°$ from the equator. They experienced a peak ΔT of around 30–$50\,\text{mK}$ before quenching.

The STM measurements on cold spots were conducted using a Unisoku ultrahigh vacuum STM system at temperatures between 1.0–1.7 K. A detail of the system is given elsewhere [80]. For all the measurements, Pt-Ir tips were used. Two different methods were employed for the measurement: crashing the tips into the sample surface, and Ar-ion sputtering the surface clean of oxides. A typical STM system is equipped with a feedback loop that precisely controls the position of the tip a few nanometers above the sample surface by measuring the tunneling current. For the Nb sample, however, the surface is already dominated by several nanometers thick insulating Nb_2O_5 layer [81]. Since the tunneling current decays exponentially with distance, the STM cannot measure the DOS of the bulk
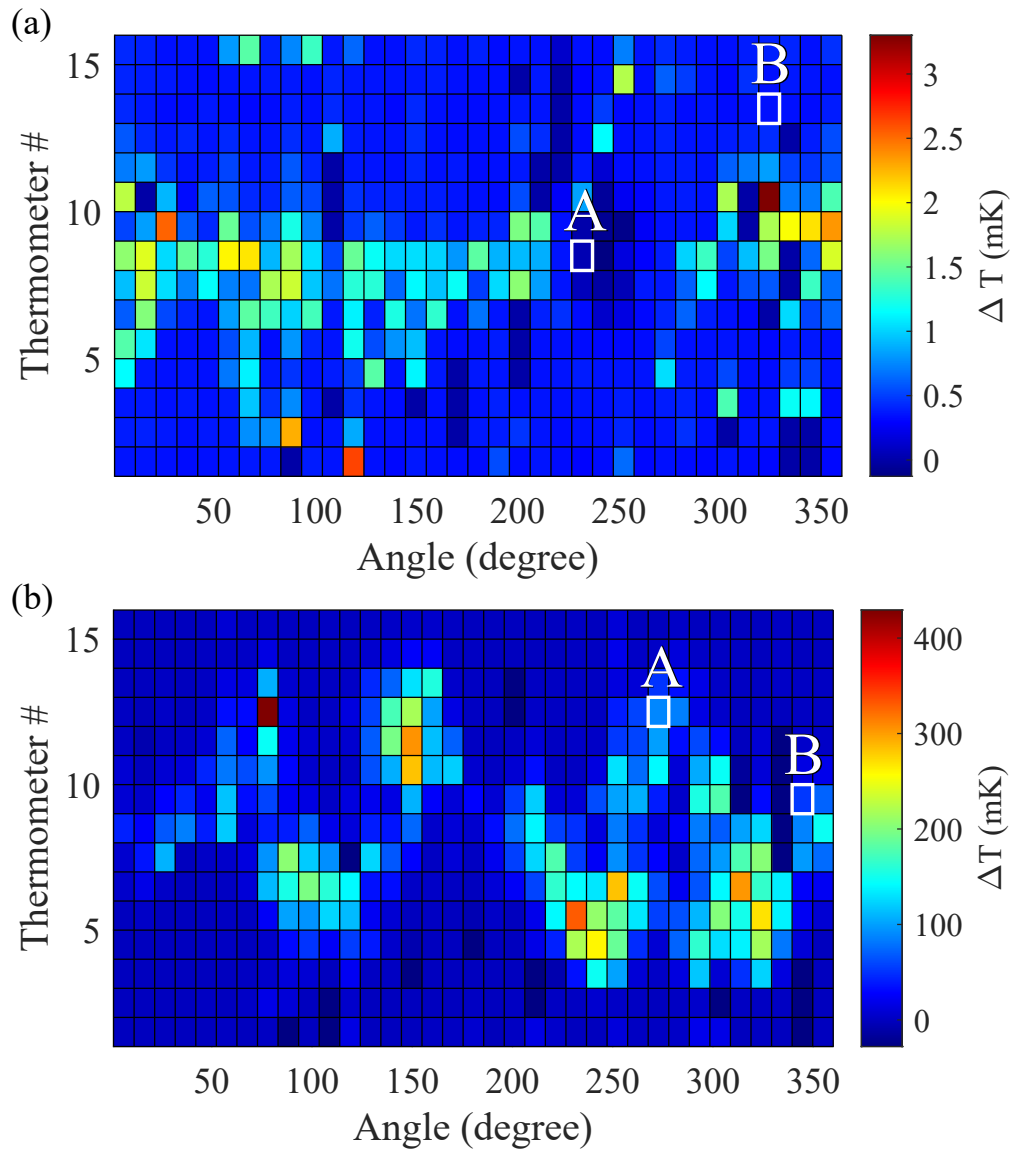
FIG. 18: Temperature maps at $1.6\,\mathrm{K}$ for the (a) TD4 and (b) A2 cavities right before the quench. The locations of the coupons labeled with A are measured with STM tips breaking the oxide and B are measured with STM after Ar-ion sputtering.

underneath the thick oxide. Therefore, it was necessary to either break through the oxide with the tip or clean the oxide layer with Ar-ion sputtering.

The STM tip was crashed into the sample surface by manually lowering the tip into the sample until a current was detected. This operation was repeated several times to break the oxide layers followed by a precise adjustment of the tip position using a feedback loop to stabilize the current to near $100\,\mathrm{pA}$ with a bias voltage of 10 mV. The tunneling spectra are acquired at this stage, and this procedure is repeated on different spots to obtain data statistics. The main advantage of this method is that it probes information about the native oxide layer that acts as a tunneling barrier between the tip and the sample and gives insight into what effect the nitrogen-doping has on the oxide layer. The downside is that this method does not allow for spatial scan across the surface, and the measured tunneling spectra contain complex contributions from a large area of the tip including the side surface. The barrier thickness and composition vary every time a tip lands into a new spot; thus, the results suffer from low statistics and a low amount of data.

In the second method, the surface of the Nb sample is cleaned first by Ar-ion sputtering in-situ, after the sample is transferred to the STM system. The surface removal rate was calibrated using Atomic Force Microscopy (AFM) to be approximately 0.27 nm/min, and the sample was sputtered for 60 minutes. This ensures that thick oxide layers are reduced and the tunneling currents are detected without crashing the tip into the sample. With this method, the bulk DOS can be measured with more statistics as the flat surface allows the tip to scan a wide area and collect a larger number of data.

5.8 STM RESULTS

The differential conductance dI/dV obtained in the measurements are analyzed using Eq. (107). The collected tunneling spectra are fit with this Dynes formula and Δ and Γ are calculated to get a broad idea of what Δ and Γ are expected from the untreated surfaces. Next, the DOS based on the theory of proximity coupled N-S bilayer [58, 70] is fit to tunneling spectra measured on the Ar-ion sputtered surface, and the effect of nitrogen doping on the suboxide layer is investigated by calculating Δ, Γ, α, and β.

5.8.1 RESULTS FROM CRASHING THE TIP

The tunneling spectra obtained by crashing the tip into the native Nb surface were fit with the simple Dynes formula to get an idea for Δ and Γ in the N-doped and the typical cavity samples. Several locations were investigated and the average values for Δ and Γ are

obtained from 20-50 spectra. Figure 19 shows a typical tunneling spectrum for the samples, and the distribution of the Δ and Γ are summarized in the histogram shown in Fig. 20. The histograms show that Δ on average is larger for the standard Nb compared to the N-doped Nb; however, the distribution of Δ is greater, and in particular, low value Δ's and large Γ/Δ were observed more often in the standard Nb samples. These results indicate the standard Nb samples exhibited stronger inhomogeneities of the superconducting properties on the surface. It is worth noting that only about 50% of acquired spectra for the standard Nb samples and 70% of the N-doped Nb samples could be fitted with the Dynes formula. The rest of the spectra exhibited subgap states, zero-bias conductance peaks, and gapless spectra.
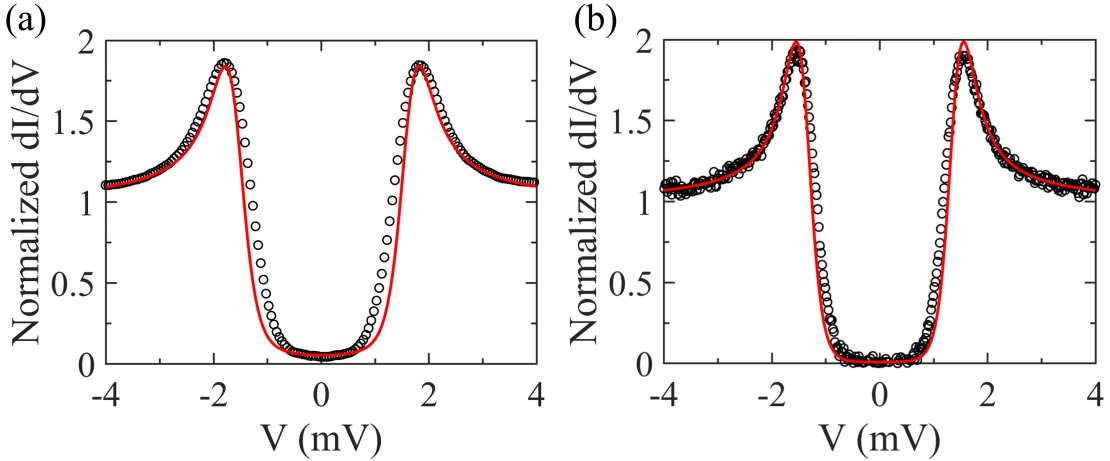
FIG. 19: Typical tunneling spectra measured (dot) from (a) the standard Nb sample and (b) the N-doped Nb sample by crashing the tip into the surface at $T = 1.5\,\mathrm{K}$. The data are fit (red)with Dynes formula, with (a) $\Delta = 1.60\,\mathrm{meV}$ and $\Gamma = 0.08\,\mathrm{meV}$ and (b) $\Delta = 1.39\,\mathrm{meV}$ and $\Gamma = 0.0\,\mathrm{meV}$. Plots reproduced from Ref. [53].
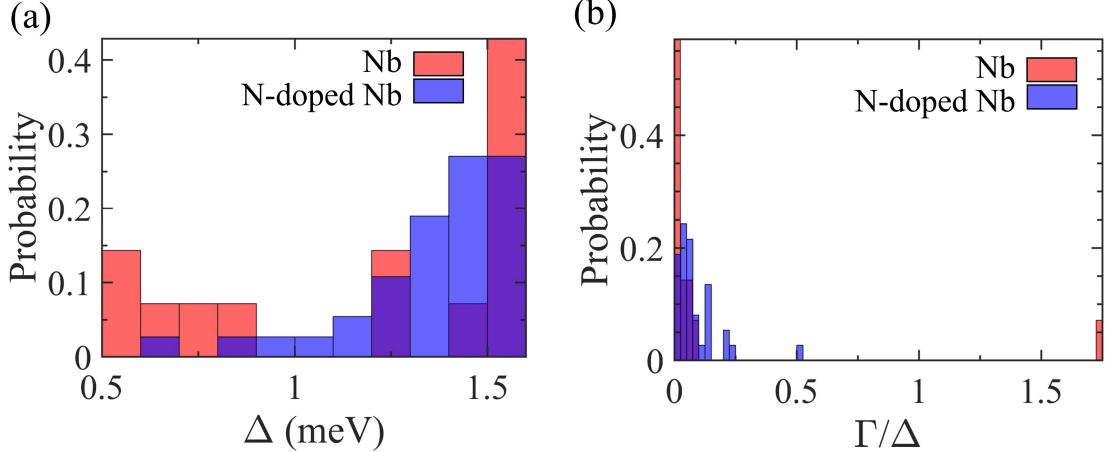
FIG. 20: Histograms showing the probability of occurrence for Δ and Γ in the standard and N-doped Nb samples, measured by crashing the tip into the surface. Plots are reproduced from Ref. [53].

5.8.2 RESULTS FROM THE AR-ION SPUTTERED SURFACE

Removal of the thick insulating layer by Ar-ion sputtering reveals a metallic surface that can be scanned without crashing the tip into the sample and thus obtain a larger number of data. The Ar-ion sputtering removed approximately 15 nm from the surface in both samples. Tunneling spectra were obtained in a grid pattern with a spacing of 32.6 nm over an area of $390 \times 390 \, \text{nm}^2$ or $780 \times 780 \, \text{nm}^2$, and this was repeated over several regions by moving the tip to a new location, typically $500 \, \mu\text{m}$ apart. The obtained spectra were fit using the DOS modified by the proximity coupled N-S bilayer [70]. Figure 21 shows the typical tunneling spectrum obtained in this method as well as a least-squares fit of the data. The probability histograms of the extracted parameters are illustrated in Fig. 22. On average Δ is reduced for the N-doped samples, but the spread is narrower. The broadening parameter Γ/Δ_0 on average is slightly larger than the standard Nb sample.

Interestingly there was an obvious difference in the distribution of α and β between the standard and N-doped Nb samples. On average, more spectra were obtained from the standard Nb samples that exhibited higher α value, and the extracted β values varied significantly more compared to the N-doped sample. The fitted values of β for the N-doped

Nb sample were clustered around $\beta \simeq 0.3$–0.4. Lower α values indicate the thickness of the normal layer in the N-doped Nb sample is reduced compared to the standard Nb. β quantifies the interface resistance, so the surface with higher β values means N-S layers are more decoupled with weakened proximity effect, which may lead to a higher surface resistance.
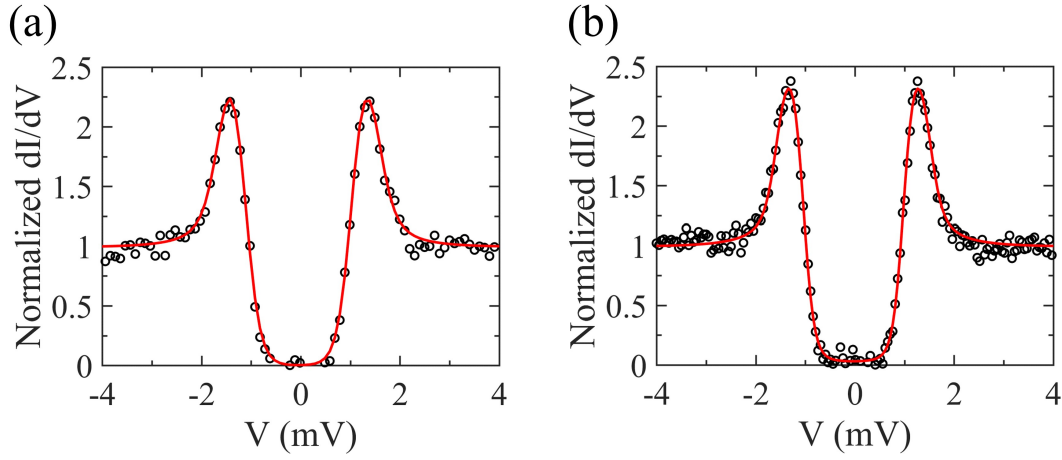
FIG. 21: Typical tunneling spectra at $T = 1.5$ K (dots) for (a) the standard and (b) the N-doped Nb samples with fit (red) using the DOS model incorporating the N-S layer. The fit parameters in these examples are $\Delta = 1.65$ meV and $\Gamma = 0.004$ meV for the standard sample and $\Delta = 1.63$ meV and $\Gamma = 0.03$ meV for the N-doped samples.

5.9 DISCUSSION OF THE STM RESULTS

The probability histograms in Fig. 20 reveal a wide distribution of Δ and Δ/Γ. For Δ, the value ranged from as low as ~ 0.3 meV to to an ideal Nb $\Delta \sim 1.6$ meV. Such low values indicate strong spatial inhomogeneities of the surface superconducting properties, which may result from thick metallic suboxide islands throughout the surface. The results show that such inhomogeneities are reduced and the surface properties become more uniform by
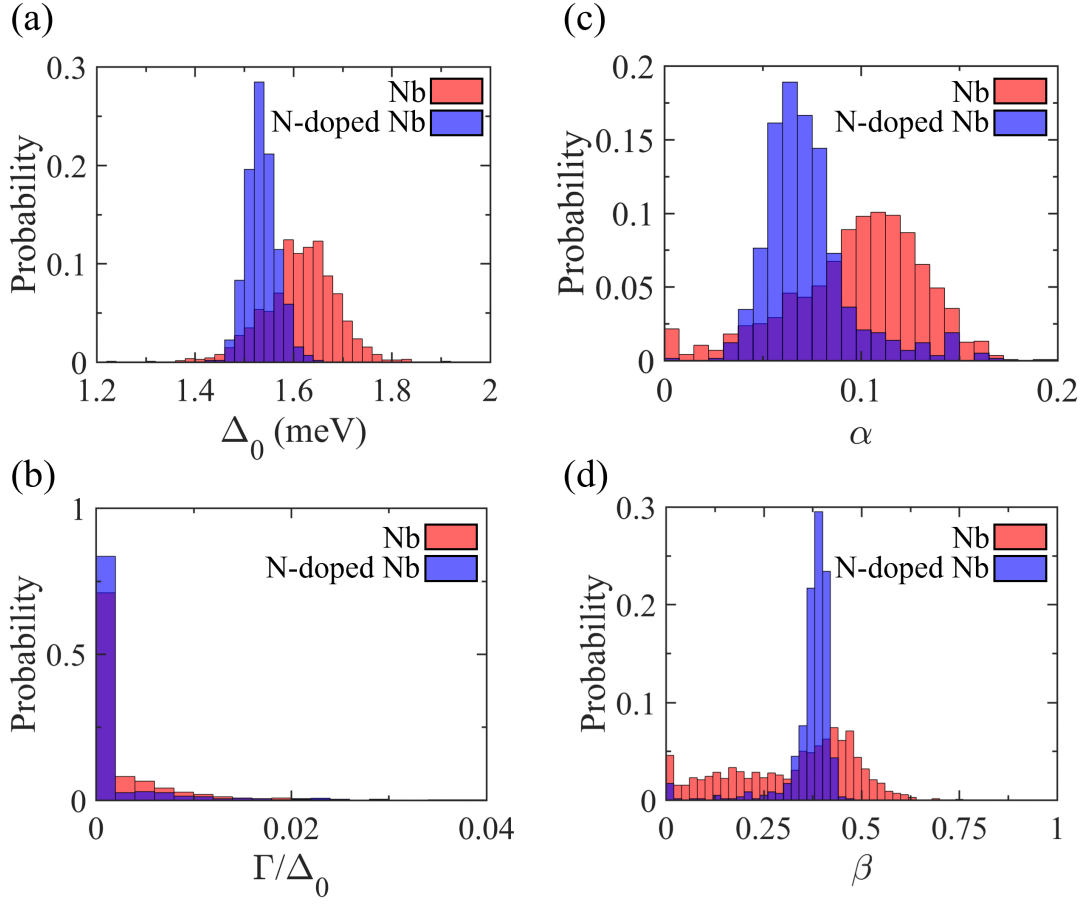
FIG. 22: The probability histograms of the calculated parameters Δ, Γ/Δ, α, and β at $T = 1.5\,\mathrm{K}$. Number of spectra taken for these measurements were 1440 for the standard and 576 for the N-doped samples.

nitrogen doping. This finding is consistent with tunneling results on titanium-doped cavity samples as well [49].

It should be noted that for the data obtained by crashing the tip into the surface, 30% of the spectrum from N-doped and 50% of the spectrum from the standard Nb samples could not be fit with either the Dynes formula or the modified DOS of the N-S bilayer [70]. This is not surprising given the complex interplay of the oxide and metallic suboxide surface on the superconducting properties, and it only reinforces the need to better understand the physics of the Nb surface. For instance, among the many spectra that could not be explained by the Dynes formula were those tunneling currents that appeared gapless. This could indicate the presence of metallic suboxide with a small gap [70]. Spectra with zero bias conductance peak or deep subgap states were also observed, which could suggest a presence of magnetic impurities [69] or two-level states at the surface [82]. Crashing the tip into the sample to extract reliable information may still not be a very controlled and consistent procedure especially because it requires a proper theoretical understanding of the influence of the side current and tunneling through complex oxide layers of variable thickness. Nevertheless, this method and the analysis with the simple Dynes model revealed differences in the distribution of Δ and Γ/Δ among two samples. Additionally, more parabolic-shaped background conductance at energy $eV > \Delta$ were observed for the standard Nb sample compared to the N-doped Nb sample. The parabolic-shaped conductance is related to a lower average work function, or in other words, the surface of the N-doped Nb sample may have reduced metallic defects in the natural oxide layer. This observation is consistent with the results of Ref. [83].

The results from Ar sputtered surface cannot exactly represent the surface of the Nb cavities since Ar sputtering alters the oxide layer; however, the results give insight into new ways of reducing R_s by materials treatments and surface nanostructuring [70, 71]. There are clear differences in the results between the standard and N-doped Nb samples as shown in Fig. 20 when they were treated to the same Ar sputtering; thus, it is reasonable to suggest that the differences are the result of the nitrogen doping.

Overall, the standard Nb samples have a higher average Δ and Γ than the N-doped Nb samples, but they also have a broader distribution of these values. It shows that nitrogen doping reduces the spatial inhomogeneity of the superconducting properties. This is also true for α and β extracted from the samples. The peak values of $\alpha \approx d/\xi$ were reduced from $\simeq 0.1$ to $\simeq 0.06$ and are more homogeneous compared to the standard Nb samples. Therefore, the results show that nitrogen-doping can reduce the thickness of the metallic

suboxide layers. Similarly, β values are less spread apart in the nitrogen-doped samples. In particular, most of the low and high β values are eliminated, and the β values are clustered around $\beta \simeq 0.3 - 0.4$. According to the proximity model [70], these values of β can lead to R_s smaller than that of an ideal surface.

The current induced broadening of the gap peaks can reduce R_s with increasing rf field [23, 65, 71]. However, if the broadening effect due to thick suboxide layer or by any other material induced increase in Γ is strong enough, the effect of current-induced broadening is not sufficient to produce the effect of the unconventional decrease in R_s with the field. However, as observed in the STM results, if the nitrogen doping can bring the material-induced broadening to an optimal level, the current induced broadening of the DOS will prevail and reduce R_s with the field. As shown in Fig. 20, the results indicate that nitrogen doping enables this field-induced reduction in R_s not by reducing Γ, but mainly by shrinking the metallic suboxide layer.

5.10 CONCLUSIONS

The temperature mapping experiment demonstrated that the cooldown dynamics significantly influence the rf losses in the hot spots. Between two cooldown rates, the faster cooldown reduced the intensity of the hot spots and improved Q_0 by 50–80%. The hot spots were primarily caused by the trapped magnetic flux during the cooldown of the cavity. These hot spots contribute to the residual resistance of the cavity at low temperatures and reduce the performance of the nitrogen-doped cavity. Our results show that optimizing the cooldown dynamics is an effective way to push out magnetic fluxes to maximize the efficiency of the cavity.

The heating as a function of the field on the quench spot revealed that the heating in the quench spot is insignificant prior to quenching, in the order of a few millikelvins. This behavior indicates that quenching in the nitrogen-doped cavity is due to the flux entry when the field is increased above H_{c1}. The reduction in the quench field compared to the standard cavity is most likely attributed to the lowering of H_{c1} by the nitrogen impurities on the surface of the cavity. Importantly, the results from TD3 and TD4 cavities indicate that the effect of the nitrogen impurities can be tuned by the amount of surface removal by EP. This suggests that the level of surface impurities and the amount of surface removal can be controlled to better engineer the nitrogen-doped cavities to meet the requirements of specific application goals.

Using the STM, the first few nanometers from the surface of the cavities were investigated.

Comparison between the nitrogen-doped and the standard cavities showed the nitrogen-doping reduced surface inhomogeneity of the superconducting properties, reduced thickness of the metallic suboxide layer, and optimized the contact resistance of the N-S interface. These results give insight into the optimal DOS to minimize the surface resistance and suggest new ways to further improve the performance of the cavity by impurity management. The combination of the STM measurements and the theoretical analysis of the DOS demonstrated in this work will benefit future research to explore new surface preparation techniques and search for new materials.

CHAPTER 6

CPW RESONATOR MEASUREMENTS USING

A PROBE-COUPLED METHOD

6.1 INTRODUCTION

The goal of the experiment is to use the CPW resonator to establish a characterization routine for a thin film superconducting sample at a useful frequency range for the SRF accelerator applications. To this date, there are numerous techniques for the material and structural characterizations of the surface [84]. However, to fully develop the SRF thin films for an alternative to the bulk Nb, a means to benchmark rf performances of the films is much needed. Many of the surface impedance measurements on thin films require host or test cavities such as the Surface Impedance Characterization (SIC) system [85], the Quadrupole Resonator (QPR) [86, 87], the hemispherical cavities [88], the RF chokes [89, 90], and the Cornell test sample host cavity [91]. As a cost-effective way to perform low field rf tests without using any host cavities, a measurement with the CPW resonator is developed and tested.

One of the major issues we encountered while designing this experiment was making a reliable connection to and from an rf source to the sample. For example, soldering a thin copper wire from the center pin of an SMA connector directly to the surface of Nb and Nb compound superconducting films proved difficult without damaging the sample surface with heat. Even when wires were soldered properly, high contact resistance at the interface increased the return loss, making it difficult to identify the resonant spectrum.

As an alternative, we designed a probe-coupled CPW resonator box based on the design of a probe coupled microstrip line resonator described in the Ref. [92]. In the probe-coupled resonator box, a thin film CPW resonator is placed inside a box, and a pair of monopole antennas are fixed above the sample surface to couple rf currents. Weak electromagnetic waves emitted from one antenna excite the resonance of the sample and the response is then detected by the second antenna probe. From the transmission signal, Q_0 and f_r are calculated, from which the superconducting properties are extracted. The main advantage

of using the probe-coupled method is that the quality factor Q_0 and the resonant frequency f_r of the film can be measured without making physical contact with the thin film.

In this chapter, we discuss the design of the probe-coupled resonator box and the pattern of the CPW resonator etched on thin films. Experimental setups for measuring Q and f_r as a function of temperatures are described here. Results of Nb, Nb$_3$Sn, and NbTiN thin film measurements and their extracted superconducting parameters are presented.

6.2 CPW RESONATOR DESIGN

The CPW resonators were designed to achieve resonant frequencies in the 2–3 GHz range on a film of size 10 mm × 10 mm. We designed four patterns of similar geometries, where the center strip widths were $w = 40, 50, 60$, and $70\,\mu$m, and the gap between the center strip and the ground planes were $s = 30, 25, 20$, and $15\,\mu$m respectively. All patterns share the same meandered strip length of approximately 23.62 mm. A picture of one of the patterned samples taken with an optical microscope is shown in Fig. 23. Four patterns were printed on a single chrome photomask on quartz by Photo Sciences, Inc, a commercial photomask manufacturer [93], which made it possible to produce up to four resonator samples from a thin film deposited on a 2-inch wafer.

6.3 RESONATOR BOX DESIGN

CST Studio Suite®, a 3D electromagnetic simulation solver, was used to design the box for the CPW resonator sample. To accurately measure Q and f_R of the sample, any parasitic losses from the box needed to be minimized, so that only the rf losses of the sample are probed. The model represented in the simulation software is shown in Fig. 24, which consists of a mock sample, two antennas, and the housing box. The sample was represented with a metal sheet of perfect conductivity deposited on a 0.5 mm thick substrate. The substrate was assumed lossless and was assigned a dielectric constant $\epsilon_r = 9.4$ close to that of a-plane Al$_2$O$_3$. The material of the box was modeled as pure copper, and the frequency response was calculated by exciting TEM mode electromagnetic wave on the antennas.

The eigenfrequency solver was used to calculate resonant frequencies to confirm the box frequency does not overlap with the sample frequency. Without a sample, the fundamental frequency of the box was calculated to be 15.66 GHz, and the sample resonant frequency was calculated to be 2.81 GHz, well below the box resonant frequency. On resonance, the electromagnetic field maps were simulated to make sure the field is properly coupled to the sample. The electric field map plotted on the center plane of the device in the vicinity of
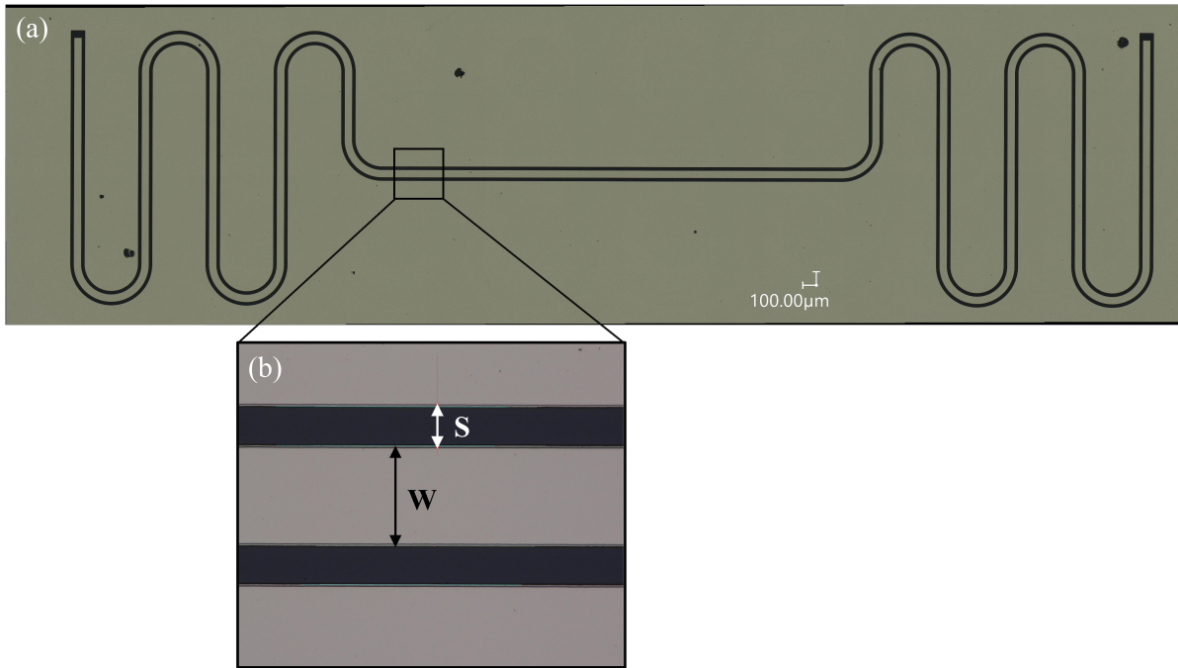
FIG. 23: (a) A resonator geometry with a center strip width $w = 70\,\mu$m is shown here as an example. The line meanders in order to fit a total length of $23.26\,$mm in a sample chip sized $10\,$mm $\times$ $10\,$mm. (b) A zoomed view of the resonator showing the dimensions. The samples were patterned with one of the dimensions of the center strip width $w = 40, 50, 60,$ and $70\,\mu$m, and corresponding gap width $s = 30, 25, 20,$ and $15\,\mu$m.
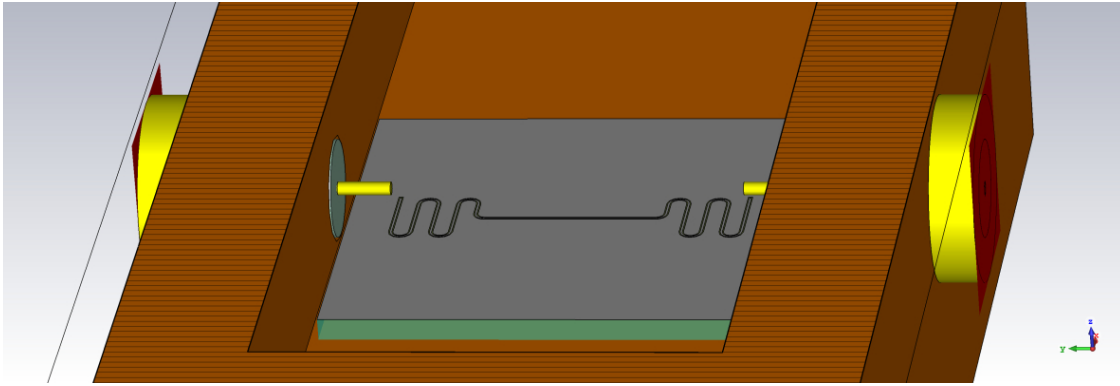
FIG. 24: A simulation model of the resonator box with a patterned sample. The rf currents are excited at one of the ports marked with the red region that transmitted through probe antennas floating above the film colored in gray. The resonator box in brown is modeled as a lossy pure copper to calculate any losses in the box.

the probe is shown in Fig. 25. The electric field plot shows the TEM-like propagation mode on the strip, and any other parasitic modes are suppressed.

The effect of the probe location on the coupling strength was also studied. Q_{ext} was simulated by adjusting the distance h between the probe and the sample as illustrated in Fig. 26. The result of the simulated external quality factor as a function of the distance is plotted in Fig. 27. The plot show that Q_{ext} varies exponentially with the distance. For example, when the probe is $0.5\,\mathrm{mm}$ above the sample, the Q_{ext} is 6×10^5 and is increased by an order of magnitude when the height increases by a mere $1.5\,\mathrm{mm}$. These results show that unless either the probe is nearly touching the sample or the resonator Q is in the 10^6–10^7 range, it would be impossible to achieve critical coupling. However, to ensure that the probe does not make any contact with the sample during measurements at a cryogenic temperature, the probe position was decided to be at least $1\,\mathrm{mm}$ above a sample when the thickness is $1\,\mathrm{mm}$. Unfortunately, this design further reduces the coupling when thinner samples are measured in this box.

Finally, any parasitic losses in the box were investigated. At the resonance, the electromagnetic field that reaches the surface of the box produces eddy current on the lossy
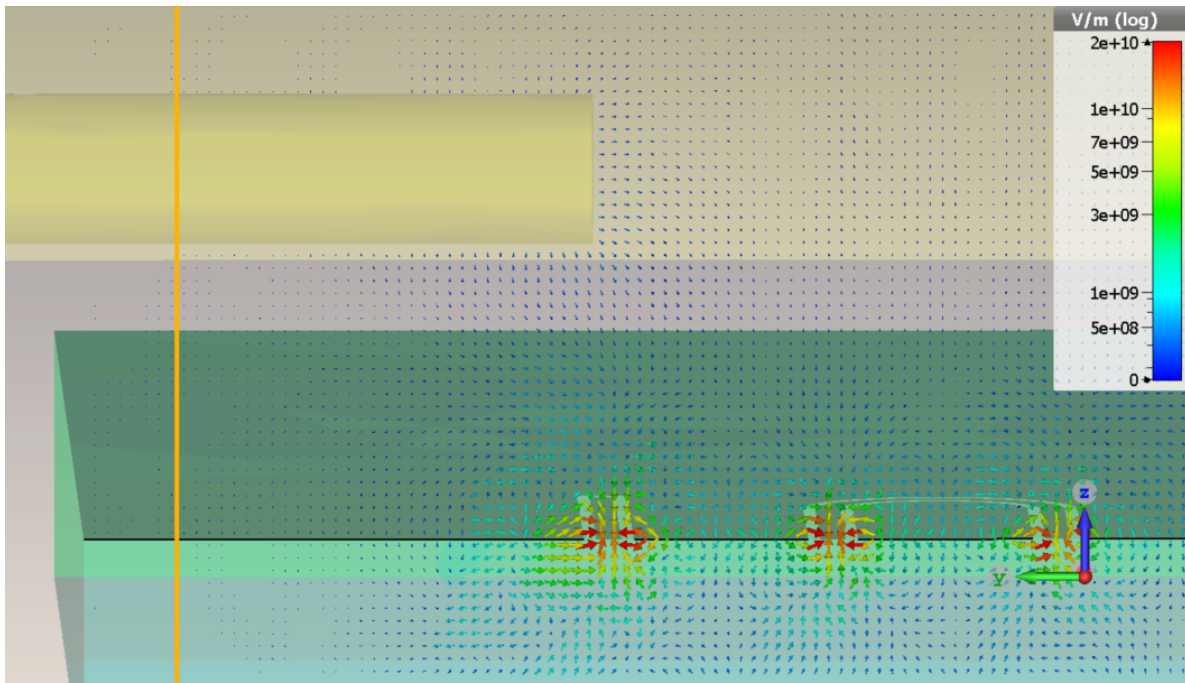
FIG. 25: The simulated electric field map on the cross-section of the resonator, in the vicinity of the probe antenna.
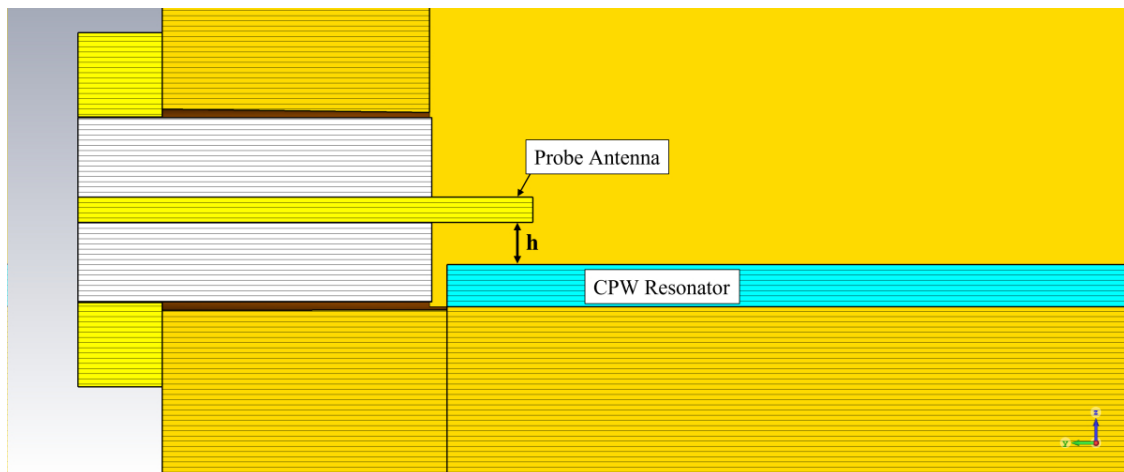
FIG. 26: A cross-sectional view of the resonator box and sample model. The coupling strength between the antenna and the resonator is dependent on the distance h.
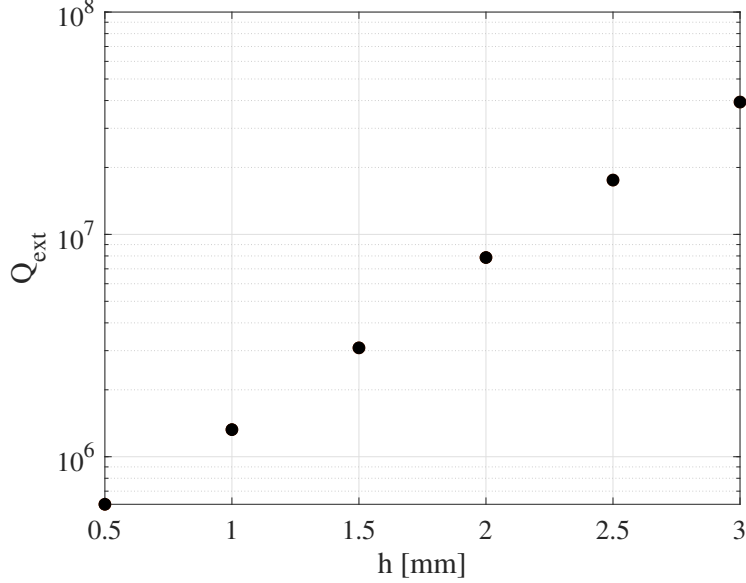
FIG. 27: A simulated Q$_{ext}$ as a function of the distance h between the probe and the surface of the resonator.

surfaces. This loss contributes to the measured loaded quality factor as

$$\frac{1}{Q_L} = \frac{1}{Q_0} + \frac{1}{Q_{ext}} + \frac{1}{Q_b},$$

(109)

where Q_b is the quality factor associated with the losses in the box. The copper box quality factor was simulated to be $Q_b = 4.4 \times 10^5$, which can be in the same order of magnitude as the resonator Q_0 if untreated. The simulation of the surface power loss revealed that most of the power loss is concentrated on the surface directly underneath the resonator pattern. The contour plot of the surface power loss density is illustrated in Fig. 28. To mitigate the loss produced in the box, a ditch was designed in the high loss region. With a 6 mm wide and 4 mm depth ditch, the loss in the box was reduced significantly, improving the box quality factor to 10^7.

The final sketch of the box is shown in Fig. 29. The inner cavity has the dimensions of 10.41 mm × 25.40 mm ×5.23 mm, with a 5.99 mm wide ditch of depth 4.01 mm. Two boxes were fabricated with different materials, one with Nb and another with OHFC copper, to confirm whether the losses in the boxes are insignificant. For an antenna, a flange mounted straight terminal (PN 1052902-1, TE Connectivity, USA) is used. It consists of an SMA
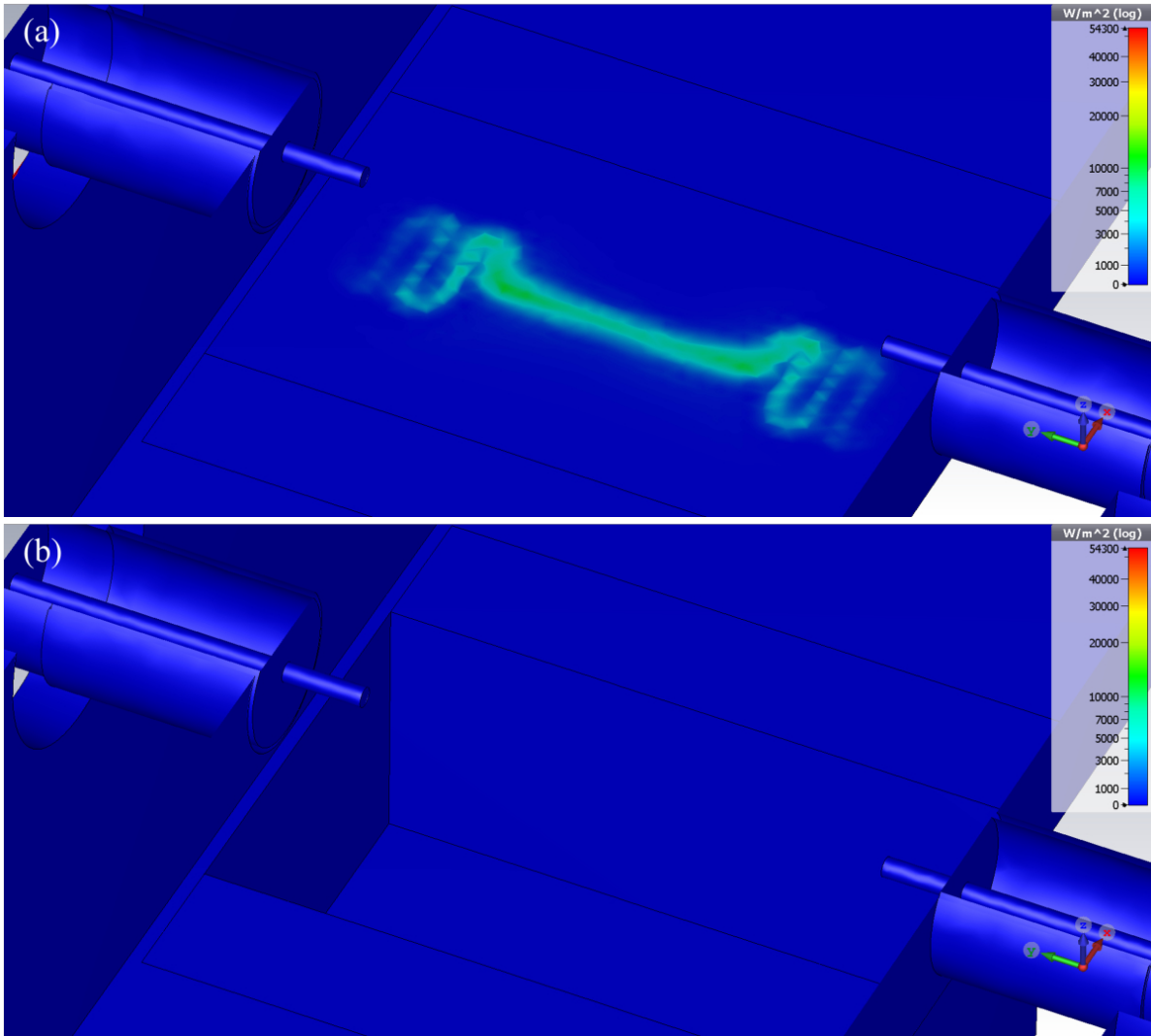
FIG. 28: (a) A contour plot showing power loss density in W/m^2 on the surface of the copper box. The sample is removed from the view for a clear view of the surface underneath the resonator. It is visible that most of the loss is concentrated under the resonator and negligible elsewhere. (b) The loss in this region is mitigated by creating a ditch in the region.

jack receptacle on one end and extruded dielectric and a further exposed center pin on the other end. The center pin is constructed from gold-plated beryllium copper with a diameter of 0.010 mm and length 0.049 mm.

6.4 RESONATOR SAMPLES

Three different Nb compound films were patterned for our work: Nb, NbTiN, and Nb_3Sn, The Nb film was grown on a 0.5 mm thick, 2 inch a-plane Al_2O_3 wafer using an electron cyclotron resonance (ECR) plasma reactor by A. -M. Valente-Feliciano at Thomas Jefferson National Accelerator Facility [94]. The thickness of the deposited Nb was approximate 1 μm. A 600 μm thick NbTiN film had also been prepared by A.-M. Valente-Feliciano using DC magnetron sputtering with a NbTi alloy target and grown on a 0.5 mm thick MgO substrate. The specifics of the growth chamber are described elsewhere [95]. Lastly, the Nb_3Sn film grown by C. Sundahl from University of Wisconsin-Madison was approximately 120 nm thick, grown on a 0.3 mm thick, 2 inch r-plane Al_2O_3 substrate. The film had been grown by co-sputtering Nb and Sn targets, where the detail of the setup and technique is described in Ref. [96].

All the films were patterned into a CPW resonator by STAR Cryoelectronics, a commercial foundry that specializes in superconducting device fabrications [97]. The patterning process involved standard photolithography, followed by either chemical wet etching or reactive ion etching, and dicing into 10 mm × 10 mm individual samples. The sample dimensions were measured with a digital microscope (Keyence VHX-7000), and they are summarized in Table 1. Nb and Nb_3Sn were etched using reactive ion etching and wet etching respectively, and they show slightly more over-cutting compared to NbTiN which was etched using Ar ion milling.

6.5 EXPERIMENTAL SETUP AND PROCEDURE

6.5.1 ASSEMBLY

The sample to be measured was placed in the resonator box using Ag conductive paint (Leitsilber 200, Ted Pella, Inc) and cured for one hour. Side edges of the sample were covered with Ag paint to properly ground the ground plane of the CPW resonator with the box. The Nb box and the OFHC copper box with an installed sample are shown in Fig. 30. The vacuum chamber for the box was prepared with an 8 inch long, ConFlat® Flange Full
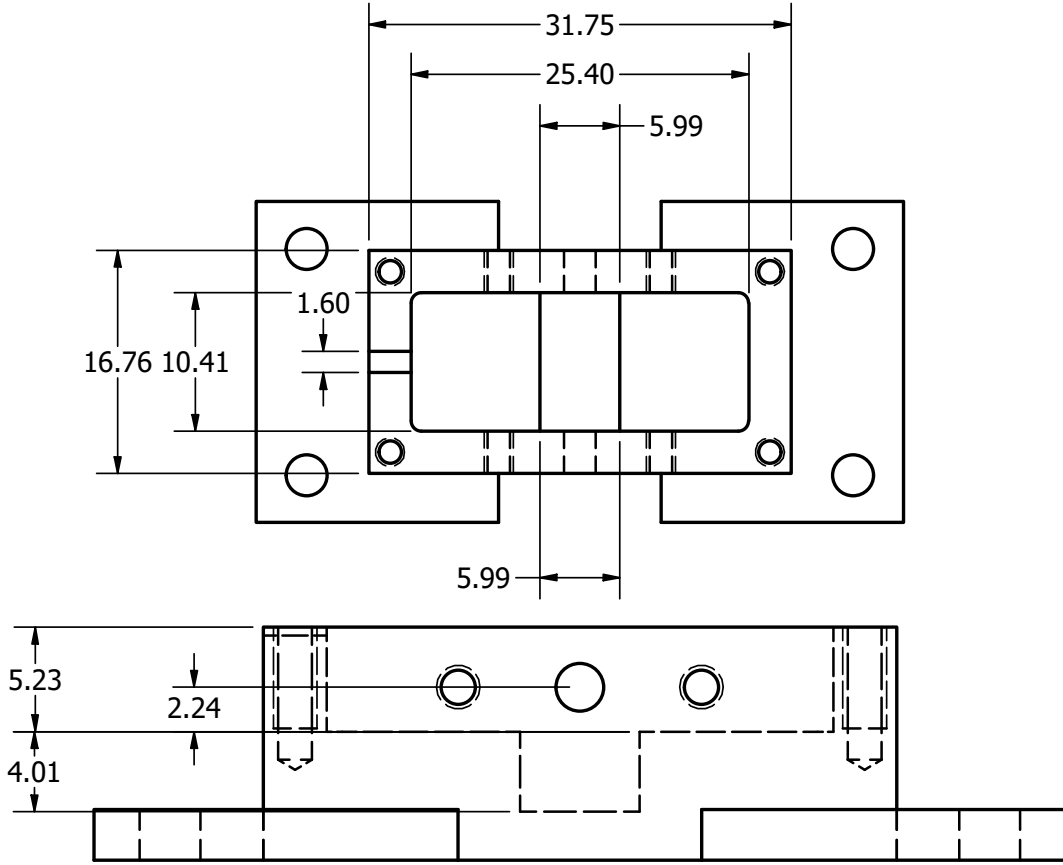
FIG. 29: Top and side view of the resonator box with dimensions in mm. A flat lid is used to fully enclose the box, except for a small slit of width 1.60 mm to ensure the inside of the box is also vacuumed.

Film Material	w	s	t	l	f_r
Nb on Al_2O_3	55.7 μm	25.61 μm	1.5 μm	22.39 mm	2.950 GHz
Nb_3Sn on Al_2O_3	56.74 μm	23.62 μm	120 nm	23.52 mm	2.808 GHz
NbTiN on MgO	59.19 μm	22.77 μm	600 nm	23.74 mm	2.768 GHz

TABLE 1: A summary of select sample dimensions as measured with a digital microscope. The resonant frequency was estimated by calculating L and C from the measured geometry and estimating $\epsilon_r \approx 9.30$ for Al_2O_3 and $\epsilon_r \approx 9.64$ for MgO.

Nipple with a 6 inch fitting. The end flange was prepared by taking a bored 6 inch ConFlat® stainless steel flange and brazing 0.125 inch thick OHFC Cu plate in the center to improve thermal conductivity across the flange. The resonator box was screwed onto the flange with Apiezon® N grease in between for good thermal contact, and two Cernox® temperature censors were mounted on the flange close to the box, and their lead wires were thermally anchored to a gold-plated copper bobbin heatsink (HSB-40, Lake Shore Cryotronics, USA). Figure 31 shows the setup of the flange. On the other end of the tube, ConFlat® 4-way standard cross was used to direct rf cables from the probes to one axis, the thermometer leads to another, and the last port to the vacuum pipe of the vertical test stand. The final assembly on the test stand is shown in the Fig. 32 before being lowered into a cryostat for measurements. The cryostat is approximately 1.8 m deep into the ground with a mu-metal shield for reducing Earth's magnetic field. Once in the cryostat, the rf cables were connected to a vector network analyzer (VNA) and Cernox® temperature sensor leads were connected to Model 218 Temperature Monitor (Lake Shore Cryotronics, USA). The chamber was then evacuated to about 10^{-8} mBar using a turbomolecular pump backed by a diaphragm vacuum pump. The cryostat dewar was filled with LHe for the cooldown to 4.3 K and then pumped down to further lower temperature to 2 K. The schematic of the setup is shown in Fig. 33.
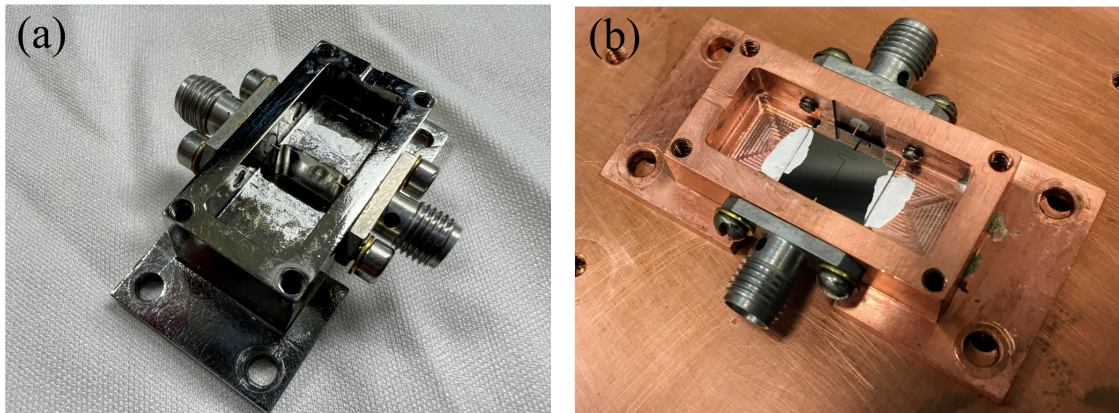
FIG. 30: (a) A box made with Nb and (b) the setup of the copper resonator box with installed probe antennas and the sample mounted with the Ag paint.
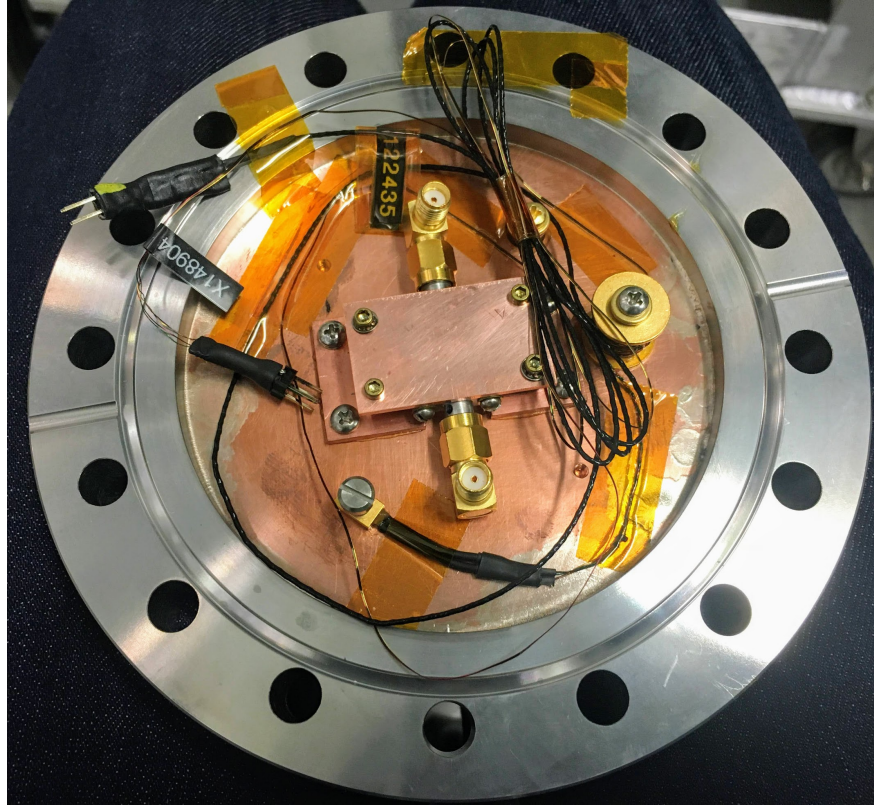
FIG. 31: The setup of the flange with the resonator box with a lid, two Cernox® sensors, and a heat sink installed.

6.5.2 COUPLING FACTOR MEASUREMENTS

The coupling factors of the resonators were measured at the beginning of the experiment. The coupling factors $\beta_{1,2}$ for the antenna port 1 and the port 2 are given as

$$\beta_1 = \frac{\beta_1' \left(1 + \beta_2'\right)}{1 - \beta_1' \beta_2'}, \tag{110}$$

and

$$\beta_2 = \frac{\beta_2' \left(1 + \beta_1'\right)}{1 - \beta_1' \beta_2'}, \tag{111}$$

FIG. 32: The vacuum chamber connected to the vertical test stand for testing.
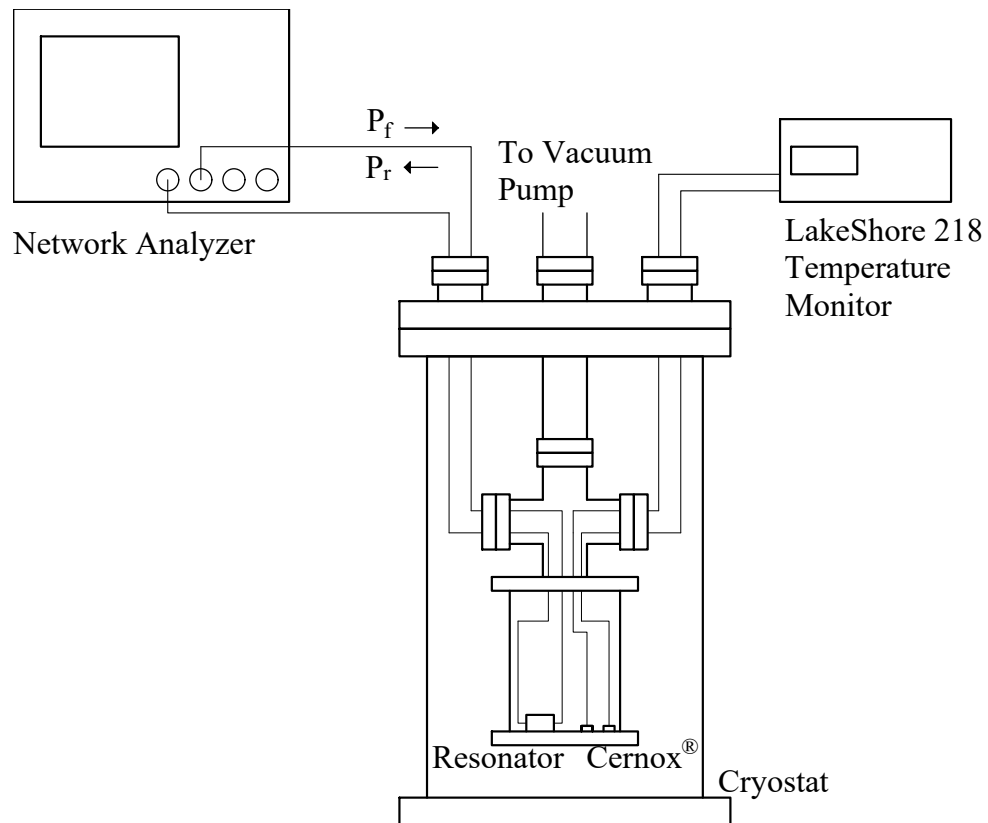
FIG. 33: The schematic diagram of the experimental setup. The vacuum chamber containing the resonator and the temperature sensors are immersed inside a cryostat with liquid helium. The coupling is calculated by measuring P_r and P_f right outside the cryostat using a power meter.

where

$$\beta'_{1,2} = \frac{1 \pm \sqrt{\frac{P_r}{P_f}}}{1 \mp \sqrt{\frac{P_r}{P_f}}}, \tag{112}$$

where P_r and P_f are power reflected from and forwarded to the resonator measured at the port 1 and the port 2, and the upper sign is used for overcoupled ($\beta > 1$) and lower sign is for undercoupled ($\beta < 1$) [26]. Whether the resonator is over or undercoupled is checked by observing the S_{11} and S_{22} around resonance in polar coordinates. If the loop encloses the center, it is overcoupled; if not, it is undercoupled. Once the sample is in the dewar, the forwarded and reflected power of the resonator can only be measured from outside the cryostat as indicated in Fig. 33. The measured power includes attenuations by the cables that are inside the cryostat, and they must be accounted for to calculate the coupling coefficients. To calculate the attenuation in the cables, the forwarded and reflected powers are measured at a frequency $\sim 500\,\mathrm{kHz}$ away from the resonance. Assuming that all the power is reflected at the sample off-resonance, the attenuation of the cables are given as

$$\alpha = \sqrt{\frac{p_{r,off}}{p_{f,off}}}, \tag{113}$$

where $p_{r,off}$ and $p_{f,off}$ are reflected and forwarded power respectively. Taking into the attenuation of the cables, P_r/P_f on resonance is then

$$\frac{P_r}{P_f} = \frac{p_{r,on}/\alpha}{p_{f,on}\alpha} = \frac{p_{r,on}p_{f,off}}{p_{f,on}p_{r,off}}, \tag{114}$$

where $p_{r,on}$ and $p_{f,on}$ are the measured reflected and forwarded power on resonance. Coupling coefficients are calculated by plugging in Eq. (114) into Eq. (112). The corresponding external $Q_{ext1,2}$ are then calculated by

$$Q_{ext1} = \frac{Q_L(1 + \beta_1 + \beta_2)}{\beta_1}, \tag{115}$$

$$Q_{ext2} = \frac{Q_L(1 + \beta_1 + \beta_2)}{\beta_2}. \tag{116}$$

6.5.3 Q_0 AND F_R MEASUREMENTS AND ANALYSIS

A transmission spectrum S_{21} of the resonator was measured as a function of temperature up to T_c of the sample. The drive power of the VNA was selected to be -30 dBm to maximize the signal-to-noise ratio while avoiding distortion of the Lorentzian shape in the transmission signal. As illustrated in Fig. 34, when the input power is increased, the Lorentzian shape becomes asymmetric and the peak frequency decreases. This asymmetry is caused by the nonlinear effect on both the kinetic inductance and the surface resistance. The kinetic inductance increases as the circulating current breaks the Cooper pairs, which in turn, lowers the resonant frequency. The surface resistance is also affected by the current as it induces local heating, vortex penetration, and field penetration through defects. When the input power is further increased, a bifurcation into two peaks is observed at the -10 dBm mark as a result of exceeding the critical current of the film.

A resistive heater at the bottom of the dewar was used to boil off liquid helium and slowly warm up the sample. During the warm-up, a computer program written in LabView™ was used to automatically export an S-parameter S_{21} around resonance and the temperature sensor readings. The program continuously monitored the resistances of the temperature sensors from Model 218 Temperature Monitor and converted them to Kelvin units using calibration curves. Every time the program detected a change in temperatures by $dT = 0.05$ K, it triggered the network analyzer to export the transmission and reflection spectra as Touchstone files. The exported Touchstone files are then fit using MATLAB® to extract Q_0 and f_R at each temperature point.

An ideal S_{21} response around resonance is described by

$$S_{21}(f) = \frac{S_{21}(f_r)}{1 + 2iQ_L \frac{f - f_r}{f_r}}, \tag{117}$$

whose magnitude is a Lorentzian function

$$|S_{21}(f)| = \frac{|S_{21}(f_r)|}{\left(1 + Q_L^2 \left(1 - \frac{f}{f_r}\right)^2\right)^{1/2}}, \tag{118}$$

with a phase given as [19]

$$\tan(\phi(f)) = 2Q_L \frac{f_r - f}{f_r}. \tag{119}$$

The ideal S_{21} plotted on a real and an imaginary axis is a circle that passes through an origin and whose center lies on the real axis as illustrated in Fig. 35. In real measurements, signals
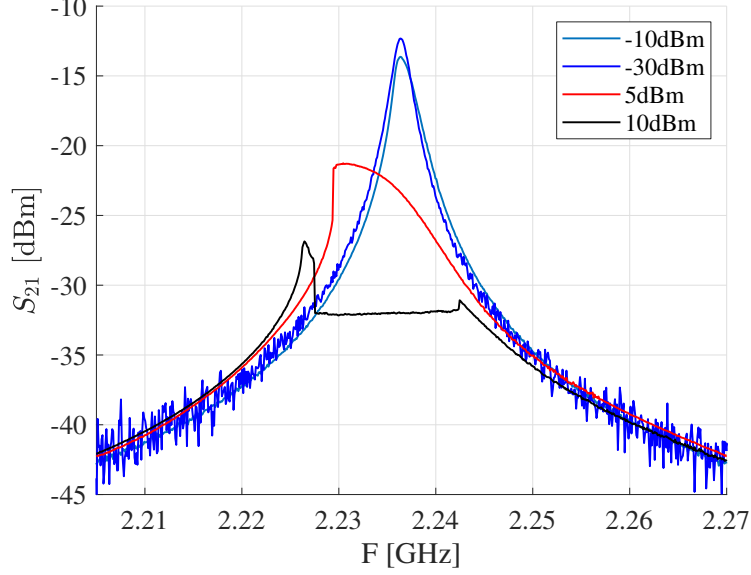
FIG. 34: A power-dependent measurement shows that as the circulating current in the resonator increases, the Lorentzian shape becomes asymmetric caused by nonlinear dependence of current on surface impedance.

travel down long cables before reaching the resonator and back to the VNA, producing a phase shift φ in the spectrum. Additionally, a fraction of the power from the input antenna may directly couple to the output antenna to generate crosstalk that bypasses the resonator. The crosstalk introduces additional background complex signal χ to the spectra. The phase shift and the crosstalk rotate and translate the resonant circle by φ and χ, modifying S_{21} as follows [98]:

$$\tilde{S}_{21} = (S_{21} + \chi)\, e^{i\varphi}. \tag{120}$$

Q_L and the f_r are extracted from the corrupted $\tilde{S}_{21}$ by following the method described in Ref. [99]. First, the plot of $\tilde{S}_{21}$ is fit to a circle on the complex plane to estimate the center. The circle is then translated to the origin. The phase $\phi(f)$ is calculated from the
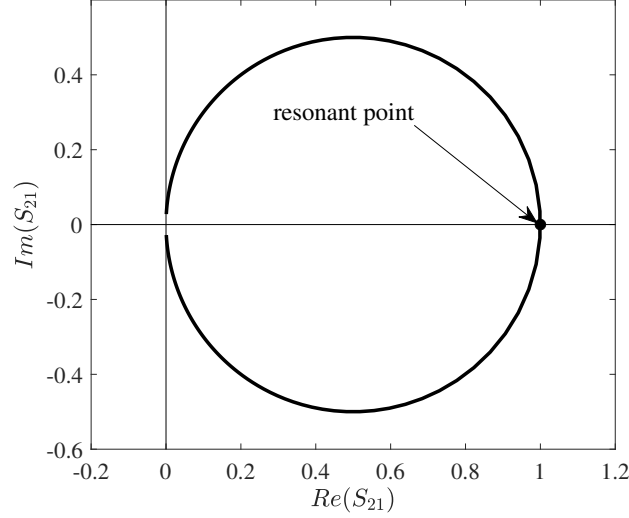
FIG. 35: An ideal S_{21} on a complex plane. Starting from the origin, the frequency increases in a counterclockwise fashion, and the resonant frequency occurs at the intersection of the real axis.

new resonant circle and is then fit to

$$\tan\left(\frac{\phi - \phi_0}{2}\right) = \left[2Q_L\left(1 - \frac{f}{f_r}\right)\right], \tag{121}$$

$$\phi(f) = \phi_0 + 2\tan^{-1}\left[2Q_L\left(1 - \frac{f}{f_r}\right)\right], \tag{122}$$

where the fitting parameters are ϕ_0, Q_L and f_r. The phase difference $\phi(f) - \phi_0$ is divided by two in Eq. (121) because the resonant circle is centered at the origin as opposed to on a real axis as was the case in Eq. (119). Figure 36 illustrates a typical fitting procedure. Finally, Q_0 is calculated by

$$Q_0 = \left(\frac{1}{Q_L} - \frac{1}{Q_{ext1}} - \frac{1}{Q_{ext2}}\right)^{-1}. \tag{123}$$

6.5.4 EXTRACTING $\lambda(T)$ AND R_S

The penetration depth of the film is deduced from a normalized shift in the resonant
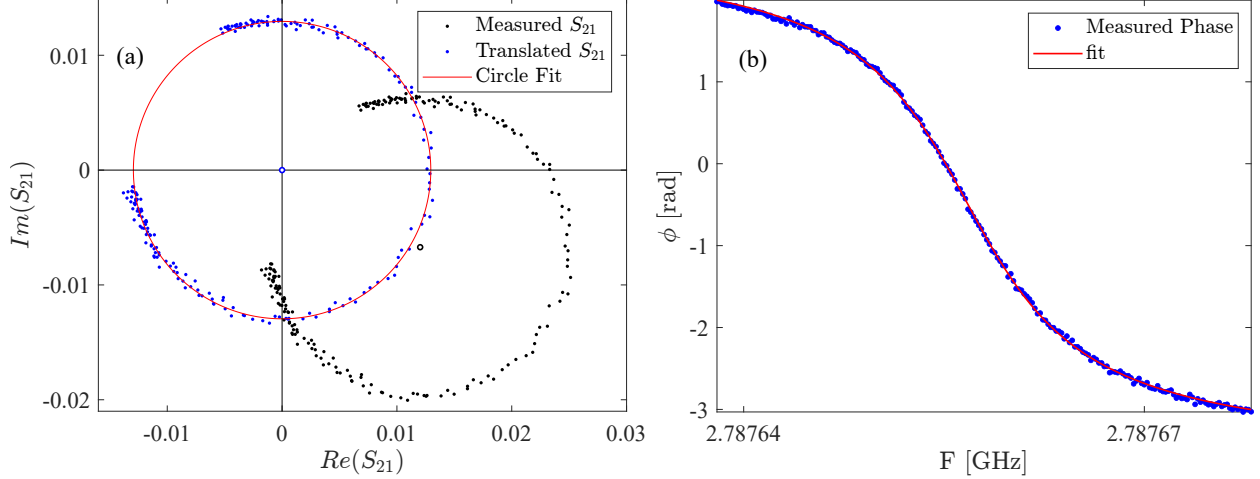
FIG. 36: (a) Shown in black is a measured S_{21} forming a circle that is both displaced and rotated. The spectrum is translated to the center (shown in blue) and fit to a circle, shown in red. (b) The phase as a function of a frequency is extracted from the new circle and fitted to extract ϕ_0, Q_L, and f_r.

frequency as a function of the temperature:

$$\frac{\delta f_r(T)}{f_r(T_0)} = \frac{f_r(T) - f_r(T_0)}{f_r(T_0)} = \sqrt{\frac{L_g + L_k(T_0)}{L_g + L_k(T)}} - 1, \tag{124}$$

where T_0 is the lowest temperature at which f_r was measured, and the geometric inductance L_g and the capacitance C are assumed to be independent of temperature. For each films tested, a functional form of $L = L_g + L_k(\lambda)$ was approximated by numerically calculating L as a function of λ using the program outlined in Section 4.4.

The numerically calculated inductance L is then fit to a second-degree polynomial function in λ to obtain $L(\lambda(T)) = g_1\lambda(T)^2 + g_2\lambda(T) + g_3$. An example plot of the calculated $L(\lambda)$ and the polynomial fit is shown in Fig. 37. This expression for $L(\lambda(T))$ can be substituted into Eq. (124) in place of $L_g + L_k(T)$ to calculate $\lambda(T)$ once the temperature dependence of $\lambda(T)$ is known. To get an estimate for $\lambda(0)$, $\delta f_r(T)/f_r(T_0)$ is fit usiong a simplified $\lambda(T)$ based on the two-fluid model:

$$\lambda(T) = \frac{\lambda(0)}{\sqrt{1 - \left(\frac{T}{T_c}\right)^4}}, \tag{125}$$
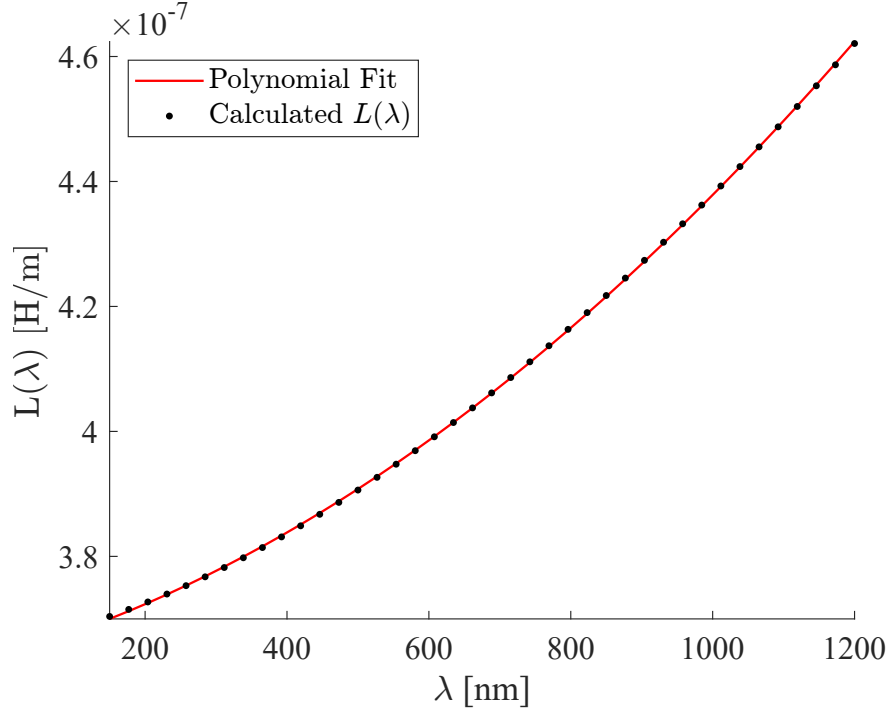
FIG. 37: An example of the numerically calculated inductance L along with the fitted second-degree polynomial function in λ for a resonator with $w = 59.19\,\mu$m, $s = 22.77\,\mu$m, and $t = 600\,\mu$m.

where $\lambda(0)$ and T_c are the fitting parameters. Notice that $\lambda(0)$ calculated in this fit is not the London penetration depth $\lambda_L(0)$ but rather the penetration depth that takes impurity scattering into account such that $\lambda(0) > \lambda_L(0)$.

For a more robust calculation, $\delta f_r(T)/f_r(T_0)$ is fit with $\lambda(T)$ calculated using the BCS theory. A computer program to fit $\delta f_r(T)/f_r(T_0)$ and R_s with the BCS calculation was written in MATLAB®. The code is based on the version originally written by J. Hallbritter [25] and also follows an interpretation by J. Gao [100] for calculating BCS kernels. The program performs a non-linear least squares fit using the Levenberg-Marquardt algorithm to extract the following parameters: T_c, energy gap Δ_0, $\lambda_L(0)$, BCS coherence length ξ_0, mean free path l, and residual resistance R_0.

The surface resistance of the film is obtained from Q_0 of the film. They are related by

$$R_s = \frac{G}{Q_0}, \tag{126}$$
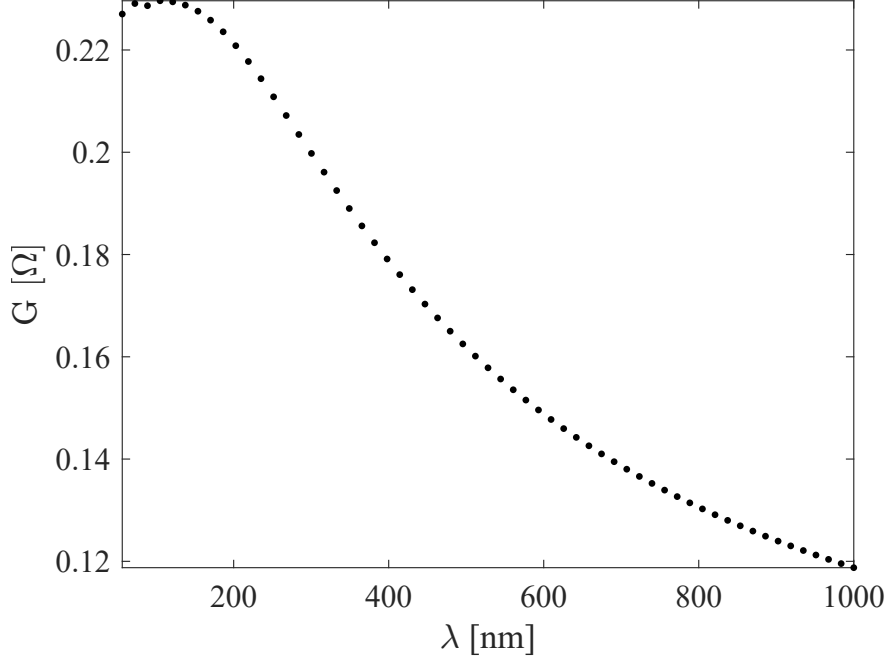
FIG. 38: An example geometric factor calculated as a function of λ for a resonator with thickness $t = 1\,\mu$m. The geometric factor is nearly constant for $\lambda/t \lesssim 0.1$ but decreases as λ increases.

where G is the geometric factor. For a film with thickness t comparable to $\lambda(T)$, G must be calculated as a function $\lambda(T)$. The geometric factor for each $\lambda(T)$ can be calculated using the same numerical algorithm and the procedure used to calculated $L(\lambda)$. An example of calculated geometric factor as a function of λ for resonator with thickness $t = 1.0\mu$m is shown in Fig. 38. Once $G(\lambda)$ is obtained, R_s is calculated using the $\lambda(T)$ obtained from $\delta f_r(T)/f_r(T_0)$ fit. Finally, to get an estimate for $\Delta(T)$, $R_s(T)$ can be fit using an analytical approximation of the BCS surface resistance valid for $T < T_c/2$ [23]:

$$R_s(T) = \frac{A}{T}e^{-\Delta/k_B T} + R_0, \tag{127}$$

where A is a constant and R_0 is a residual resistance.

$R_s(T)$ can also be fit by using the full BCS calculation, and when fit along with the $\delta f_r(T)/f_r(T_0)$ data, the superconducting parameters can be extracted with higher accuracy compared to when only one set of the data is used. This is because $\delta f_r(T)/f_r(T_0)$ data is sensitive to $\lambda(0)$, l, and T_c, while $R_s(T)$ data is more sensitive to $\Delta_0/k_B T_c$ and R_0. To make

use of both sets of data, the following process is used for extraction of the superconducting parameters:

1. Fit $\delta f_r(T)/f_r(T_0)$ using $\lambda(0)$, T_c and l as fitting parameters and $\Delta_0/k_b T_c$ and R_0 as constants.

2. Fit $R_s(T)$ using $\Delta_0/k_b T_c$ and R_0 as fitting parameters while using $\lambda(0)$, T_c, and l obtained in the previous step

3. Repeat the steps using the extracted parameters until they converge to within $\lesssim 10\%$

6.6 Nb MEASUREMENTS RESULTS

A conventional low T_c superconducting sample was used to confirm both the measurement technique of the probe-coupled resonator and the analysis method for extracting $\lambda(T)$ and $R_s(T)$. Nb films have been studied extensively in the past, and their properties are well understood. The $\lambda(T)$ and the $R_s(T)$ obtained from the resonator were compared with the BCS predictions to verify the reliability of the method. Additionally, the same Nb samples were tested in both the Nb and the OFHC Cu boxes to confirm the parasitic losses from the boxes are negligible.

The film was measured at temperatures between $2.1\,\mathrm{K}$ to $8.9\,\mathrm{K}$. A center strip and a gap width were measured to be $W = 44.90\,\mu\mathrm{m}$ and $S = 30.67\,\mu\mathrm{m}$ respectively, and the thickness of the film was approximately $1\,\mu\mathrm{m}$. The dielectric substrate was a $0.5\,\mathrm{mm}$ thick a-plane $\mathrm{Al_2O_3}$. The total length of the resonator was approximately $l \approx 23.38\,\mathrm{mm}$, where the length of curves was estimated by taking an average of inner and outer edge lengths. Using the conformal mapping formulae outlined in the Section 4.3, the geometric transmission line parameters were calculated to be $L_g = 423.8\,\mathrm{nH}$ and $C = 131.2\,\mathrm{pF}$ when $\epsilon_r = 9.3$ was used for the dielectric constant of the substrate [101]. Based on those calculated values, the resonant frequency was estimated to be $f_r = 2.869\,\mathrm{GHz}$.

At $T = 2.1\,\mathrm{K}$, the resonator achieved $f_r = 2.875\,\mathrm{GHz}$, agreeing well with the calculated value, and the Q_L was 2.75×10^5. The couplings at this temperature were $\beta_1 = 0.185$ and $\beta_2 = 0.119$, which resulted in external quality factors of $Q_{ext1} = 1.94 \times 10^6$ and $Q_{ext2} = 3.02 \times 10^6$. To get a crude estimate for the dielectric loss, a value of a-plane $\mathrm{Al_2O_3}$ loss tangent $\tan\delta \approx 4 \times 10^{-8}$ was used [101]. Using Eqs. (96) and (97), the dielectric loss quality factor was estimated to be $Q_d \approx 3 \times 10^7$, roughly factor of two larger than the Q_L. The radiation loss was estimated by using Eq. (98) to be $Q_r \approx 5 \times 10^{10}$. Both Q_d and Q_r were

estimated to be negligible in calculating Q_0 since they were several orders of magnitude larger than the measured Q_L. $Q_0(T)$ was then calculated simply as

$$Q_0(T) = \left(\frac{1}{Q_L(T)} - \frac{1}{Q_{ext1}} - \frac{1}{Q_{ext2}}\right). \tag{128}$$

Plots of $Q_0(T)$ and normalized frequency shift $\delta f(T)/f_0 = (f_r(T) - f_r(T_0))/f_r(T_0)$ are shown in Fig. 39 and in Fig. 40. The difference in the $Q_0(T)$ from the Nb housing and the OFHC Cu housings was insignificant, which confirms that parasitic losses from the housing are negligible, as predicted by the CST simulation.

Errors for Q_0 are calculated from 95% confident bounds from the fit. Errors in $\delta f(T)/f_0$ are given by

$$\Delta \frac{\delta f(T)}{f_0} = \sqrt{\left(\frac{f_r(T)\Delta f_r(T_0)}{f_r(T_0)^2}\right)^2 + \left(\frac{\Delta f(T)}{f_r(T_0)}\right)^2}, \tag{129}$$

where $\Delta f_r(T_0)$ and $\Delta f_r(T)$ were obtained from the 95 % confidence interval from the fit. At T near $2\,\mathrm{K}$, $\Delta Q_0/Q_0 \sim 0.2\%$ and Δf was typically around $5\,\mathrm{Hz}$; however, at T close to T_c, $\Delta Q_0/Q_0 \sim 2\,\%$ while δf became in the order of kHz.

Results of $\delta f(T)/f_0$ and $R_s(T)$ fitted with the BCS calculations are illustrated in Fig. 41 and Fig. 42, and the measured data show a very good agreement with the BCS calculation. The extracted parameters are listed in Table 2, and the calculated values are well within the expected Nb parameters [102]. The estimated errors for $\xi_0(T)$ and l are large due to the effective penetration depth depending roughly on a ratio ξ_0/l; thus a separate measurement would be needed to accurately determine ξ_0 and l individually. Nevertheless, the results show the effectiveness of the measurement and analysis technique. Since the experiments conducted in Cu and Nb boxes both showed consistent results, this measurements technique would be applicable for other superconducting samples with higher T_c.

6.7 NbTiN MEASUREMENTS

A NbTiN film measured in this experiment was fabricated an electron cyclotron resonance (ECR) deposition technique at Thomas Jefferson National Laboratory. A detail of the deposition chamber is described in Ref. [95]. It was deposited on a $0.5\,\mathrm{mm}$ thick MgO substrate, and the film thickness was approximately $600\,\mu\mathrm{m}$. The geometry of the resonator was measured to be $w = 59.19\,\mu\mathrm{m}$, $s = 22.77\,\mu\mathrm{m}$, and $l = 23.74\,\mathrm{mm}$, and the resonant frequency was calculated to be $f_r = 2.768\,\mathrm{GHz}$. The sample was measured inside the Cu box between $2\,\mathrm{K}$ to $16.5\,\mathrm{K}$. For this measurement, FieldFox Handheld RF Vector Network
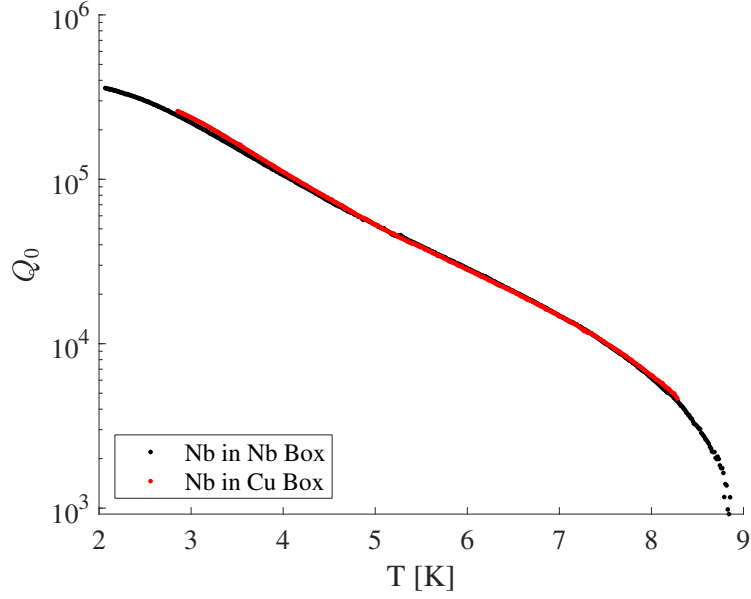
FIG. 39: Q_0 plotted as a function of T for the Nb film tested in both the Nb and the Cu housing. Error bars are omitted because they are comparable to the size of the symbols.

Parameters	Fitted Values
T_c	$9.34 \pm 0.06\,\mathrm{K}$
Δ	$1.48 \pm 0.07\,\mathrm{meV}$
$\lambda_L(0)$	$40.0 \pm 4.7\,\mathrm{nm}$
ξ_0	$39.0 \pm 23.3\,\mathrm{nm}$
l	$50.2 \pm 36.4\,\mathrm{nm}$
R_0	$0.327 \pm 0.030\,\mu\Omega$

TABLE 2: A summary of the extracted parameters for the Nb thin film using the full BCS calculation.
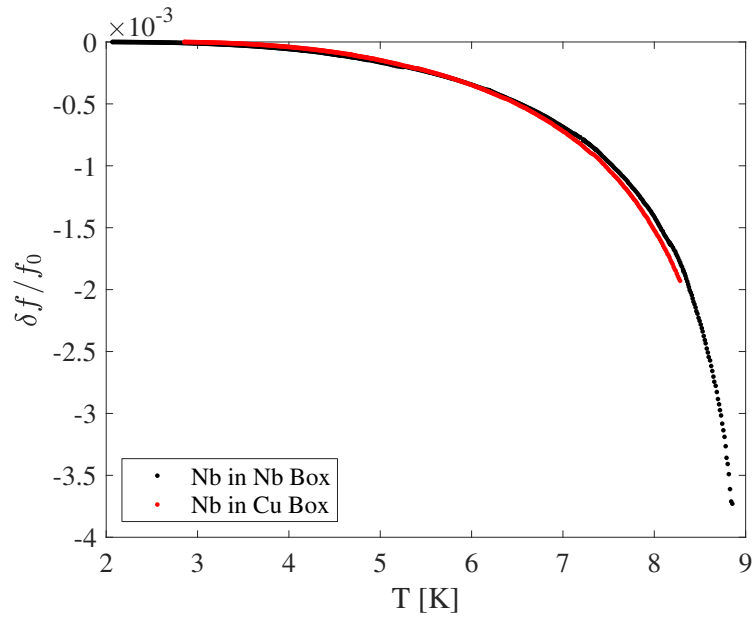
FIG. 40: Normalized frequency shift plotted as a function of T for the Nb film tested in both the Nb housing and the Cu housing. Error bars are omitted because they are comparable to the size of the symbols.
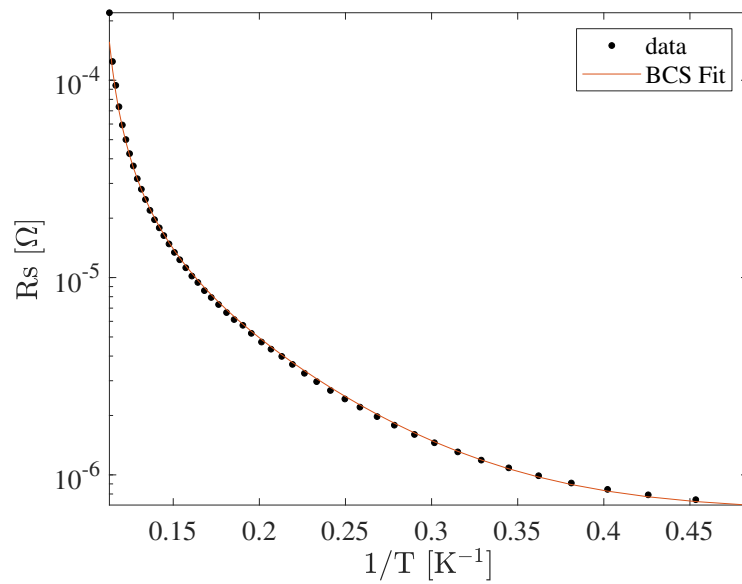
FIG. 41: An Arrhenius plot of the surface resistance versus temperature with fitted R_s from the BCS theory.
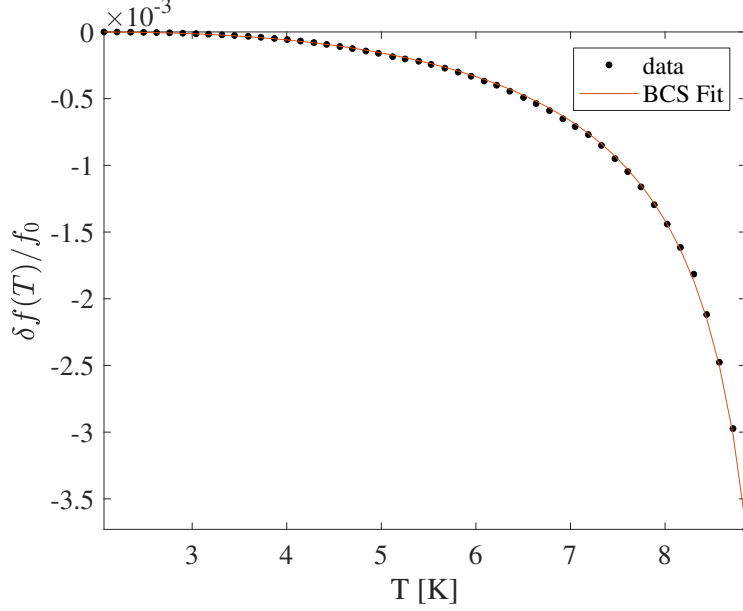
FIG. 42: The normalized frequency shift data fitted with a full BCS calculation.

Analyzer N9918A was used to measure both the fundamental and second harmonics. Similar to the data acquisition using VNA E5080A, the FieldFox was controlled via a LabVIEW program that recorded the transmission spectrum near the first and the second resonances as the dewar was warmed. At $T = 2\,\mathrm{K}$, Q_L was 2.404×10^5 at $f_{r1} = 2.788\,\mathrm{GHz}$, and Q_L was 3.248×10^5 at the second harmonics which occurred at $f_{r2} = 5.570\,\mathrm{GHz}$. The coupling coefficients were $\beta_1 = 0.0802$ and $\beta_2 = 0.0358$, which resulted in $Q_{ext1} = 3.345 \times 10^6$ and $Q_{ext2} = 7.49 \times 10^6$. Figures 43 and 44 illustrate Q_0 and $\delta f(T)/f_0$ as functions of temperatures for both the fundamental and the second harmonics. Since the penetration depth does not depend on the frequency, the normalized frequency shifts for the fundamental and second harmonics are identical.

The $\delta f(T)/f_0$ data were fit with a simplified analytical formula for $\lambda(T)$ given by Eq. (125). The fit agrees well with the data with $\lambda(T) = 270.92 \pm 0.32\,\mathrm{nm}$ and $T_c = 16.72 \pm 0.002\,\mathrm{K}$. The surface resistance up to $T_c/2$ was fit also with an analytical BCS formula given by Eq. (127) and is shown in Fig. 45 and Fig. 46. The extracted parameters were $\Delta_0 = 2.69 \pm 0.03\,\mathrm{meV}$ for both modes, and $R_0 = 0.61 \pm 0.004\,\mu\Omega$ for the fundamental mode and $R_0 = 0.82 \pm 0.007\,\mu\Omega$ for the second harmonics. Although the analysis may give a
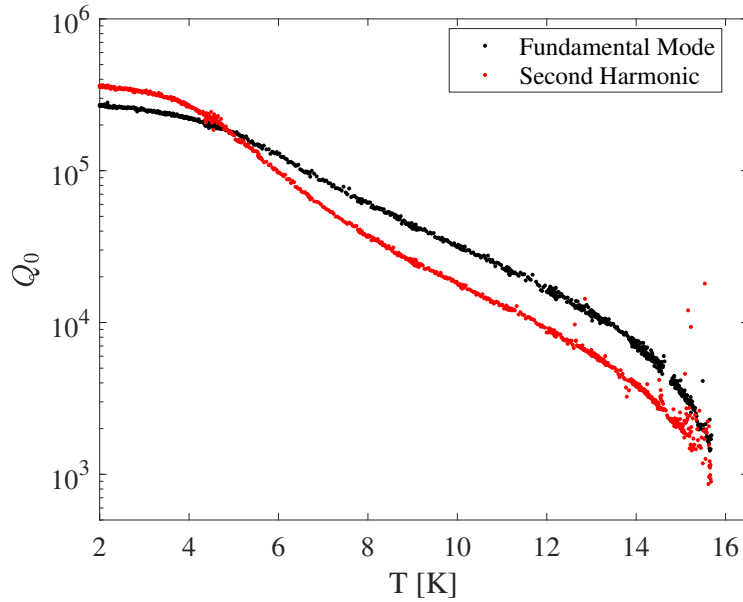
FIG. 43: Q_0 vs T for both the fundamental and the second harmonics for the NbTiN resonator.
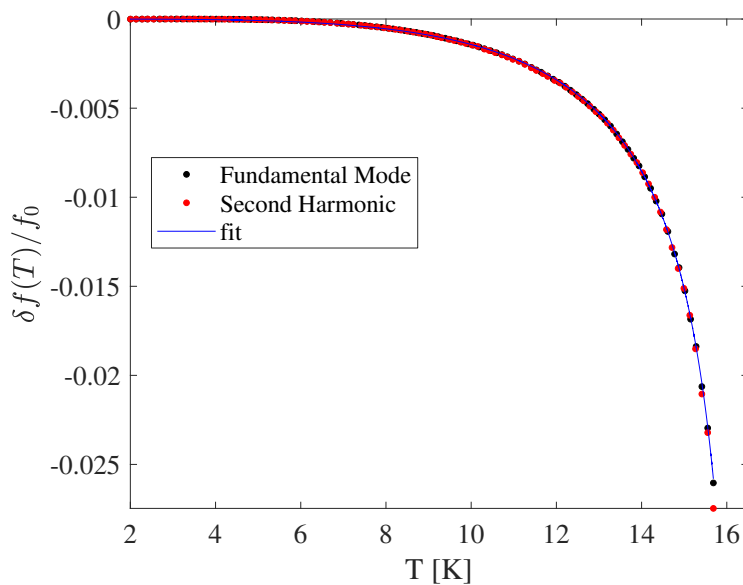
FIG. 44: $\delta f(T)/f_0$ vs. T for both the fundamental and the second harmonics for the NbTiN resonator, along with the simplified $\lambda_{eff}(T)$ fit. The normalized frequency shifts are identical for both resonant frequencies as expected.

rough estimate of the Δ_0, the fit is not a perfect representation of the data, particular in the temperature range 2.0 K–2.5 K where the data shows $R_s(T)$ to be still slightly decreasing.
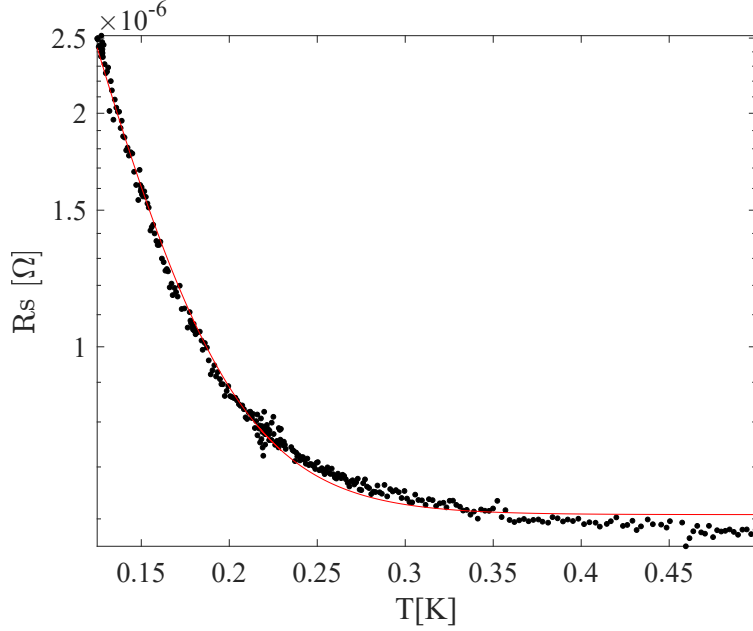
FIG. 45: R_s vs. T for the fundamental mode of the NbTiN resonator sample along with a fit of analytical BCS surface resistance formula.

6.8 Nb$_3$Sn MEASUREMENTS

An Nb$_3$Sn film measured in this study was prepared by a collaborator C. Sundahl from the University of Wisconsin-Madison. A detail of the deposition is described elsewhere [96, 103]. The film was approximately 120 nm thick and was deposited on a 0.3 mm thick, two-inch r-plane Al$_2$O$_3$ substrate. The film was also patterned by STAR Cryoelectronics [97], and the testing was done in the Cu box. The resonator had a center conductor width of $w = 56.74\,\mu$m, gap width $s = 23.56\,\mu$m, and an approximate total length of $l = 23.52\,$mm as measured by the optical microscope. This resulted in a calculated $f_r = 2.795\,$GHz. The
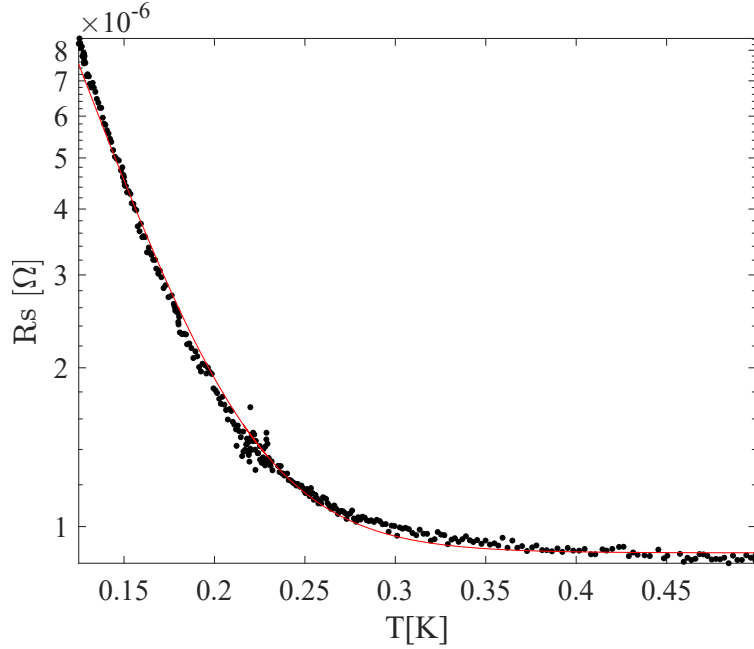
FIG. 46: R_s vs. T for the second harmonic mode of NbTiN resonator sample along with a fit of analytical BCS surface resistance formula.

coupling coefficients and the external quality factors measured at $2\,\mathrm{K}$ were the followings:

$$\beta_1 = 0.0054, \tag{130}$$

$$\beta_2 = 0.010, \tag{131}$$

$$Q_{ext1} = 4.8 \times 10^7, \tag{132}$$

$$Q_{ext2} = 2.6 \times 10^7. \tag{133}$$

Compared to the Nb film, the Al_2O_3 substrate on this sample was $0.2\,\mathrm{mm}$ thinner, which resulted in much lower coupling strengths. Nevertheless, a resonant peak was still observable at $T \sim 17\,\mathrm{K}$ above the noise floor. At $2\,\mathrm{K}$, $Q_L = 2.618 \times 10^5$ and the resonant frequency was $f_r = 2.730\,\mathrm{GHz}$, agreeing well with the analytically calculated f_r based on its geometry. The results of $Q_0(T)$, and $\delta f(T)/f_0$ are plotted in Fig. 47 and Fig. 48

The normalized frequency shift as a function of T was fitted with an approximate form of $\lambda(T)$ shown in Eq. (125) to get an estimate of the $\lambda(0)$. The extracted parameters are $T_c = 16.99 \pm 0.0006\,\mathrm{K}$, and $\lambda(0) = 202.4 \pm 0.08\,\mathrm{nm}$, well above the London penetration depth
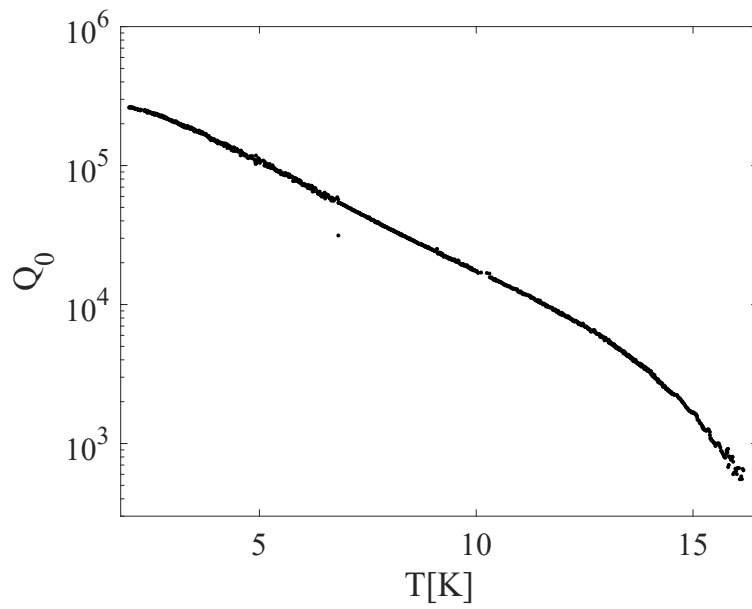
FIG. 47: Q_0 plotted as a function of T for the Nb$_3$Sn film.
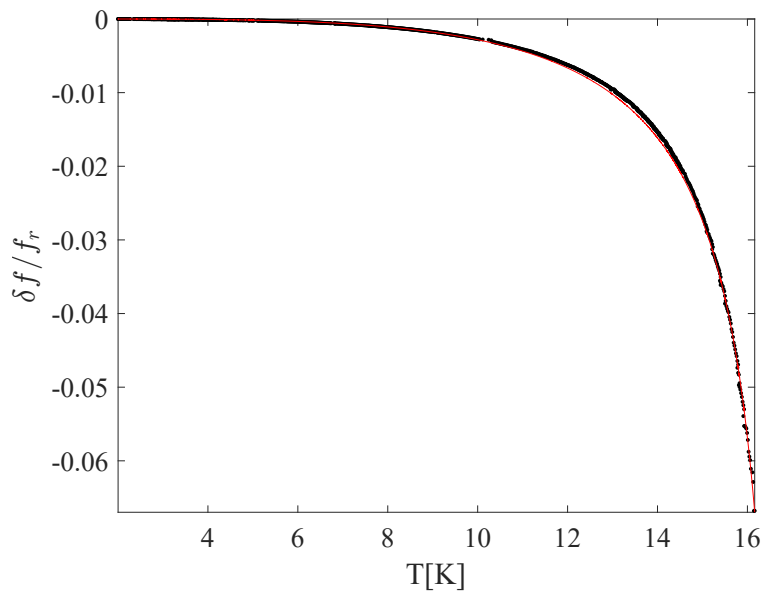
FIG. 48: A normalized frequency shift as a function of temperature for the Nb$_3$Sn sample, along with a fit using an analytical, simplified formula for $\lambda(T)$.

$\lambda(0) \approx 90\,\text{nm}$ for a clean stoichiometric Nb$_3$Sn [104]. This may results from nonstoichiometric inclusions or grain boundary structure of the Nb$_3$Sn film [96, 103].

We attempted to fit $R_s(T)$ data with an analytical form of the BCS surface resistance, but the Eq. (127) did not describe the data well. The result of a poor fit is shown in Fig. 49. The curve is calculated with $\Delta_0 = 1.9\,\text{meV}$ and $R_0 = 0.21\,\mu\Omega$. The fact that the measured R_s does not obey the BCS theory completely may also be explained by the nonstoichiometry of the sample.
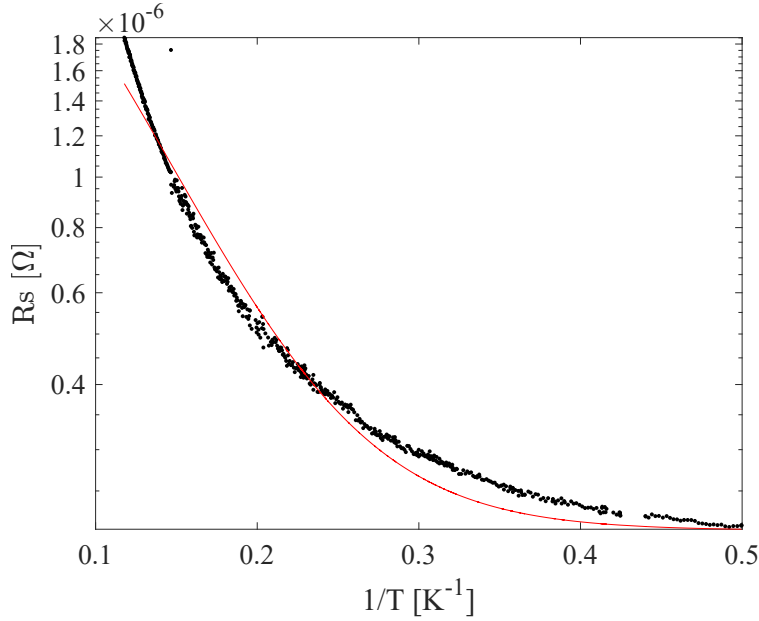
FIG. 49: R_s vs. T of the Nb$_3$Sn film for $T < T_c/2$ along with an attempted fit using an analytical BCS $R_s(T)$ approximation.

Finally, it is interesting to compare R_s for all three materials tested. The results are shown in Fig. 50. Compared to the R_s of Nb$_3$Sn, the R_s of NbTiN and possibly Nb are limited by higher residual resistance. Both Nb$_3$Sn and NbTiN exhibited lower R_s than Nb in this low power testing, which is expected for superconductors with higher T_c and Δ as

the R_s decays exponentially with $\Delta/k_B T$.

6.9 CONCLUSION

In conclusion, we have demonstrated the technique of measuring superconducting CPW resonators with the probe-coupling method. Using this technique, superconducting parameters for Nb were successfully extracted, and the resulting $R_s(T)$ and $\lambda(T)$ agreed well with the BCS predictions. We then measured Nb_3Sn and NbTiN thin films and the results were compared with Nb films. It was shown that the probe-coupled resonator measurement can provide a cost-effective routine for benchmarking superconducting films at a frequency relevant for SRF accelerating cavity application while keeping the sample size small. This will benefit the research and development of the SRF thin films by providing means to interpret how the growth parameters influence the performance of the film. As a future work, the results from probe-coupling method should be compared with those from other surface characterization methods such as the measurements using a host cavity. A 2-inch sample wafer can be measured on a host cavity first prior to being patterned into the CPW resonator, and the results can be compared to further validate this probe-coupling method.
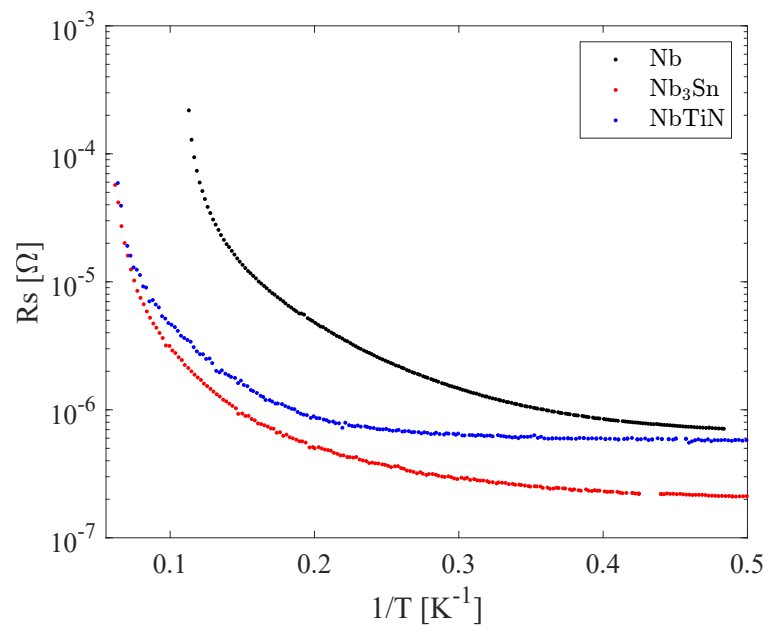
FIG. 50: Comparison of R_s of Nb, Nb$_3$Sn, and NbTiN tested using the probe-coupled resonator technique.

CHAPTER 7

CPW RESONATOR MEASUREMENTS USING

A CRYOGENIC PROBE STATION

7.1 INTRODUCTION

We used the cryogenic probe station to investigate the nonlinear Meissner effect (NLME) in a thin film Nb_3Sn CPW resonator as a function of dc field applied parallel to the film surface. The Meissner screening current density $\mathbf{J} = -e n_s \mathbf{v_s}$ induced by a weak magnetic field is proportional to the velocity $\mathbf{v_s}$ of the superconducting electrons. At higher fields, the density of superconducting electron n_s becomes dependent on $\mathbf{v_s}$ due to pair-breaking effects and results in NLME [9, 105–111]. For a single-band isotropic s-wave superconductor, the NLME is described by

$$\mathbf{J} = -\frac{\phi_0 \mathbf{Q}}{2\pi\mu_0\lambda^2}\left(1 - a\xi^2 Q^2\right),\tag{134}$$

where $\mathbf{Q} = m\mathbf{v}_s/\hbar = \nabla\chi + 2\pi\mathbf{A}/\phi_0$, m is the quasiparticle mass, χ is the phase of the order parameter $\phi = \Delta e^{i\chi}$, $\mathbf{A}$ is the vector potential, ϕ_0 is the magnetic flux quantum, and factor a depends on the temperature T, mean free path l and details of pairing mechanism [37, 112]. The NLME has attracted much attention as a means to probe unconventional pairing symmetries of moving condensates. For example Eq. (134) describes a clean d-wave superconductor at high temperature or a d-wave superconductor with impurities [105–111]. For the s-wave superconductors, NLME is absent in the clean limit, but it is present in the dirty limit $\xi \lesssim l$ [113, 114]. So far the observations of the NLME in high-T_c cuprates have been inconclusive, mostly because of a small field region of the Meissner state in high-κ type-II superconductors and contributions of extrinsic materials factors, such as grain boundaries or local nonstoichiometry [115–121]. Penetration of vortices above the lower critical magnetic field limits the max field for which NLME can be observed. To extend the field region of the NLME, we performed our measurements on a thin film of thickness $d < \lambda$ for which $B_{c1} = (2\pi_0/\pi d^2)\ln(d/\xi)$ is much higher than the bulk B_{c1} [122].
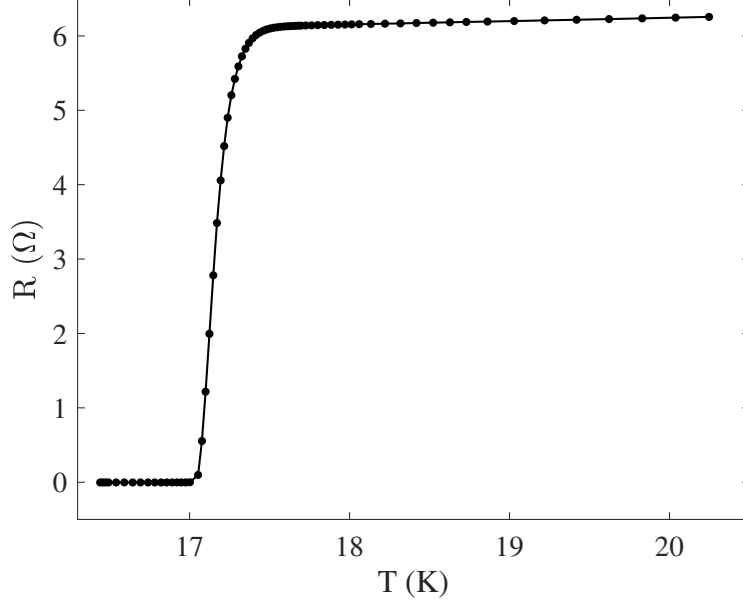
FIG. 51: Temperature dependence of the resistance of the film $R(T)$ with a midpoint critical temperature $T_c = 17.2\,\mathrm{K}$.

In this chapter, the Nb_3Sn CPW resonator and the cryogenic probe station used in the measurements of NLME are described in detail, followed by the main experimental results and the discussion of the results. This chapter is based on Ref. [112].

7.2 DESIGN OF THE SAMPLE

The coplanar resonator measured in the probe station was fabricated from a 50 nm thick Nb_3Sn film on a 10 mm × 10 mm × 1 mm thick r-plane Al_2O_3 substrate. The film was prepared with magnetron co-sputtering using both Nb and Sn targets in a growth chamber at the University of Wisconsin-Madision [96, 103]. Figure 51 shows the resistive transition in a film grown under a similar condition. The film had a midpoint $T_c \approx 17.2\,\mathrm{K}$, normal state sheet resistance of $5.1\,\Omega$, and a residual resistance ratio (RRR) of $R(300\,\mathrm{K})/R(18\,\mathrm{K}) \approx 3.2$.

The film has a polycrystalline structure with rigid grains along the [-1011] direction of the Al_2O_3 substrate as revealed by the atomic force microscopy (AFM) shown in Fig. 52. Those grains contributed to an RMS roughness of approximately 10 nm [96, 103]. The sample was patterned into a half-wave coplanar waveguide resonator using contact lithography followed
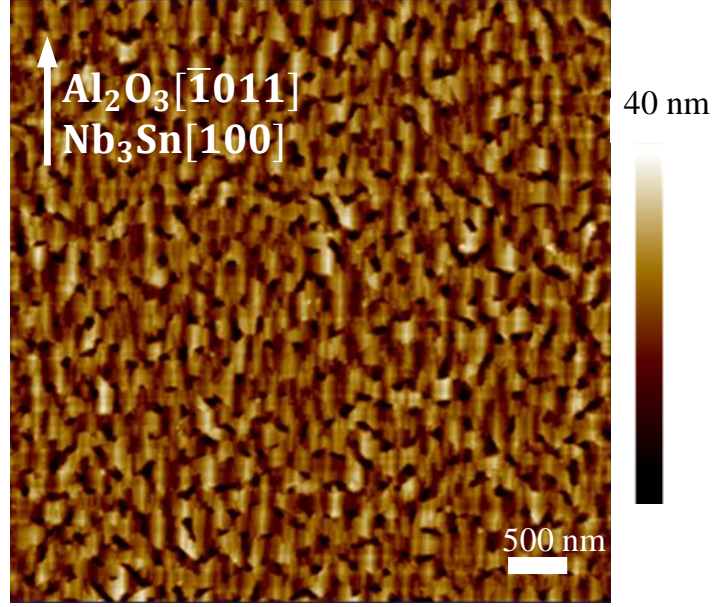
FIG. 52: AFM image showing a polycrystalline structure of the film.

by Ar ion milling. The optical image of the resonator is shown in Fig. 53. The meandered resonator has a total length $l \approx 24.6\,\text{mm}$ corresponding to the fundamental resonant frequency $f_0 = 2.236\,\text{GHz}$. The center conductor width was $w = 14.90\,\mu\text{m}$, a gap width was $s = 8.86\,\mu\text{m}$, and the film thickness was $t \approx 50\,\text{nm}$. This geometry resulted in the external inductance $L_g = 422.5\,\text{nH}$ and $C = 136.9\,\text{pF}$. The resonator is coupled to input and output rf probes by interdigital capacitors of width $w_f = 3.59\,\mu\text{m}$, gap width $2.96\,\mu\text{m}$ and length $l_f = 96.12\,\mu\text{m}$. At the ends of the transmission line, landings pads for the Ground-Signal-Ground (GSG) probes were fabricated, shown as the lightly shaded region in Fig. 53(a). These were made by first removing a few nanometers of oxide layers on the surface of Nb_3Sn using Ar ion milling and depositing a 20 nm thick layer of Pd in-situ using a lift-off technique. The landing pads made of Pd serve to prevent oxidation and damage to the film from repeated touchdown of the probes and ensure ohmic contact between the probe and the sample.
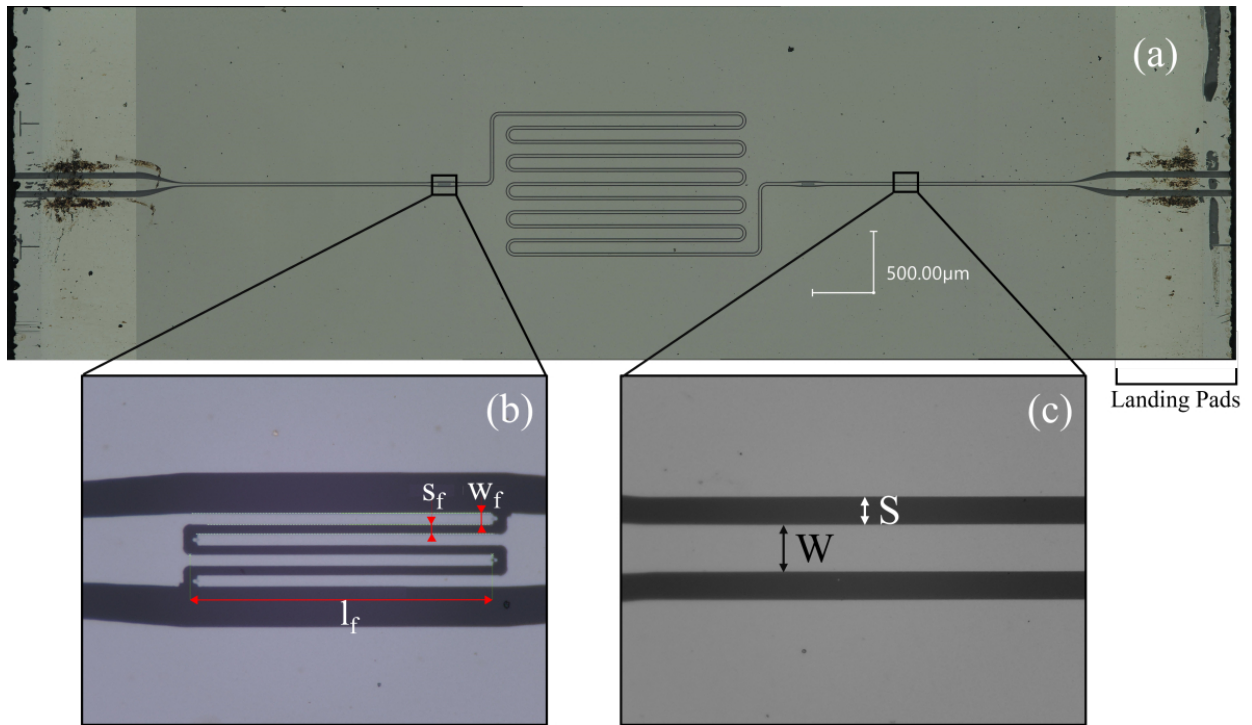
FIG. 53: (a) The image of the Nb$_3$Sn coplanar half-wave resonator. The meandered resonator in the center is terminated on both ends with interdigital capacitors shown in (b) which tapers out to the input and output landing pads. (c) Zoomed in section of the coplanar resonator where the width of the strip is $w = 14.90\,\mu$m and the gap between the signal strip and the ground is $s = 8.86\,\mu$m.

7.3 CRYOGENIC PROBE STATION

The Nb_3Sn film was measured in a Cryogenic Probe Station (CPS), built by MicroXact, Inc [123]. The overall setup of the CPS is shown in Fig. 54, and Fig. 55 illustrates the schematic diagram of the setup. The probe station consists of a vacuum chamber sized approximately $50\,cm \times 50\,cm \times 40\,cm$ rated at $10^{-5}\,Torr$ at room temperature. The vacuum system consists of HiCube 80 Eco Turbo Pump by Pfeiffer Vacuum GmbH backed by a D4B Trivac Rotary Vane Vacuum pump by Leybold GmbH. The sample is cooled to cryogenic temperature using a two-stage cryocooler Sumitomo RDK-4152 with an F-70 water-cooled helium compressor. The temperature of the first stage is $39.60\,K$ with $45.0\,W$ of heat load, and the second stage temperature is as low as $3.99\,K$ with $1.50\,W$ of the applied heat load. The first stage is used for cooling thermal shields surrounding the sample, and the second stage anchors to the superconducting magnet which is then connected to the sample stage using tinned copper braids. The sample stage is positioned at the center of the magnet, and it is thermally isolated from the surrounding using G-10 support structures.

There are two $50\,W$ resistive heaters installed inside the CPS; the first one is located on a thermal radiation shield for the cold head, and the second is fixed on a chuck that is holding the sample stage. They are used to warm the probe station to room temperature and to conduct temperature-dependent measurements. There are five sensors to monitor temperatures throughout the CPS: a silicone diode model Si410 (Scientific Instruments, USA) fixed on the thermal radiation shield of the cold head, a Si410 sensor on one of the probe arms, a silicone diode Dt-470 (Lake Shore Cryotronics, USA) on the chuck, a Cernox® temperature sensor model CX-1050-CU-HT (Lake Shore Cryotronics, USA) on the sample stage, and a ruthenium oxide RO-600 (Scientific Instruments, USA) on the surface of the superconducting magnet. The RO-600 sensor is monitored by Model 612 Temperature Monitor (Cryomagnetics, USA), and the two heaters and four temperature sensors are controlled and monitored by a cryogenic temperature controller CTC100 (Stanford Research System, USA) which is shown in the Fig. 56. The output power to the resistive heaters are regulated by the PID feedback control in the CTC100, which allows for precise temperature control with less than $50\,mK$ stability.

The superconducting magnet equipped inside the CPS is a split-coil NbTi solenoid (Cryomagnetics, USA). It is capable of producing a dc field up to $1\,Tesla$ using a Model 4G Superconducting Magnet Power Supply (Cryomagnetics, USA) shown in the Fig. 57. The magnet system is built on a gold plated support structure with openings for probe arms to reach the sample stage. It is enclosed inside a polished thermal shield cooled by the
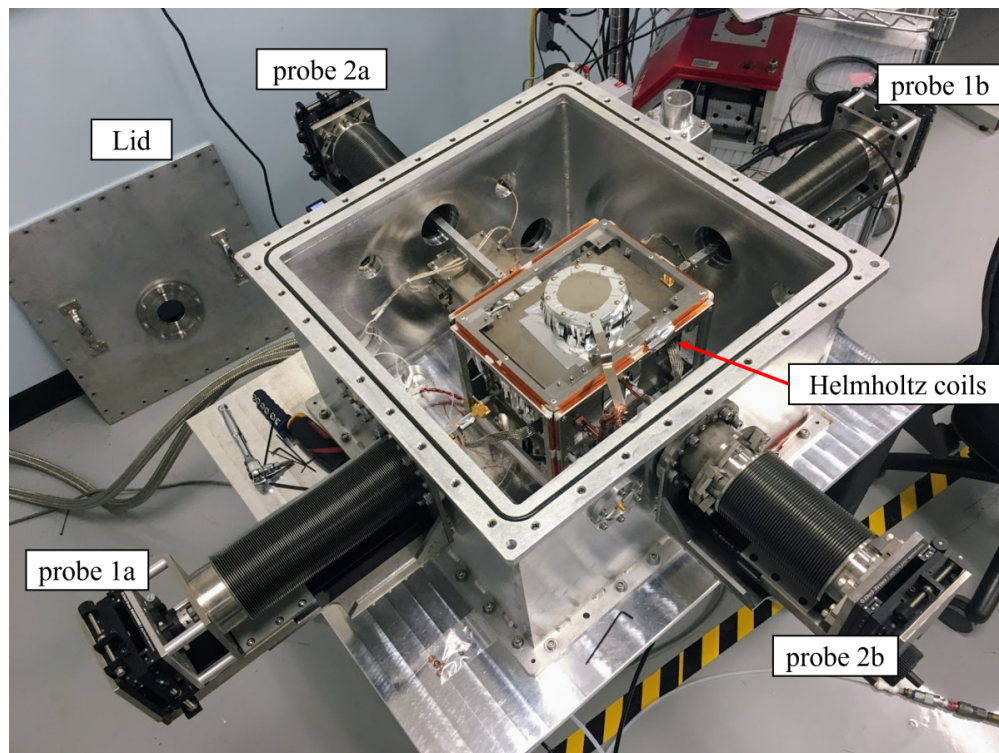
FIG. 54: An overview of the probe station with the vacuum chamber lid open.
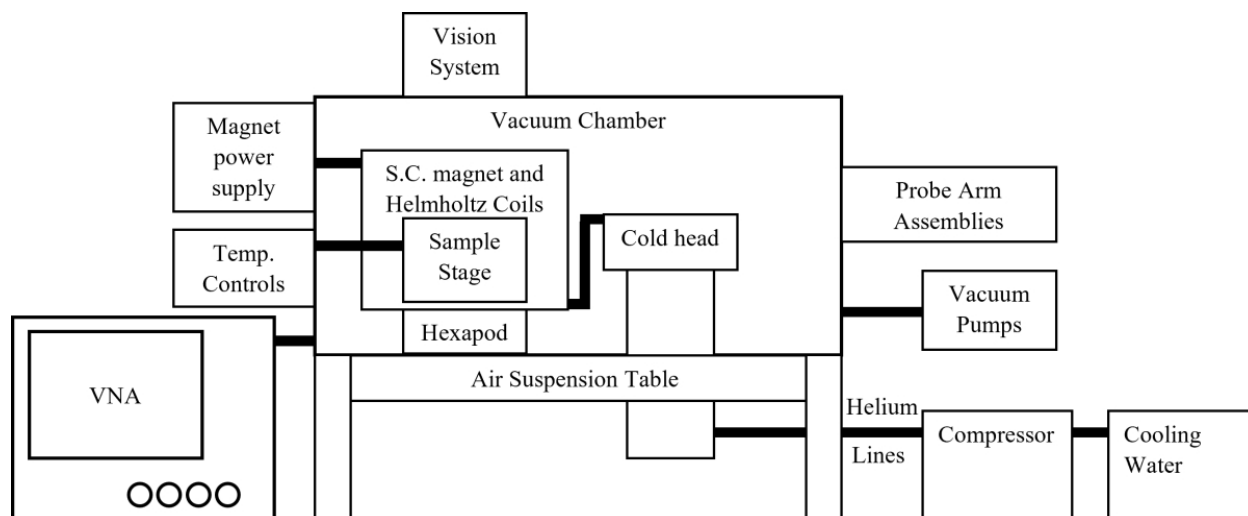
FIG. 55: A schematic diagram illustrating important components of the cryogenic probe station.
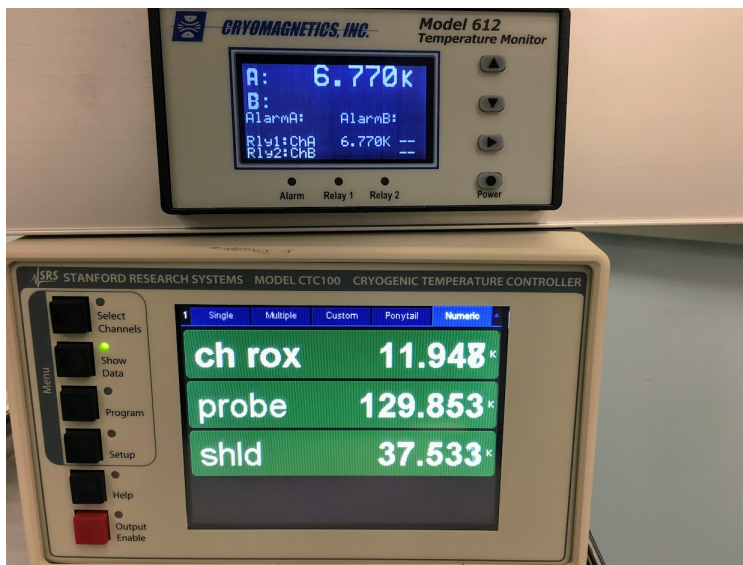
FIG. 56: Model CTC100 cryogenic temperature controller (bottom) is used to monitor four temperature sensors and controls two resistive heaters. Model 612 Temperature Monitor is used for monitoring a sensor on the superconducting magnet.

1st stage of the cryocooler. Figure 58 shows the setup with the partially removed thermal shield to reveal the superconducting magnet and the sample stage. Along the edges of the shield, there are three pairs of copper Helmholtz coils that produce a weak magnetic field to reduce any ambient field at the sample stage to minimize the number of vortices trapped in the sample during its cooldown through T_c. They are driven by three Keysight N6700 DC power modules. At room temperature, a Hall probe (Milligaus Meter MR3, AlphaLab Inc.) was fixed on the sample stage and the magnitude of the ambient field was measured while adjusting the current on the Helmholtz coils to reduce the ambient field to less than $4\,\mathrm{mG}$ in an optimum configuration. The superconducting magnet setup is mounted on a six-motor hexapod system (MHP-14 by Picard-Industries) shown in Fig. 59. It consists of six linear actuators that allow for rotation and translation of a platform in three axes with $\sim 1\,\mu\mathrm{m}$ repeatability. The motion is controlled by computer software shown in Fig. 60, and the magnet angle can be adjusted even while the sample stage is at a cryogenic temperature.

There are four manipulator arms equipped with the CPS. Two manipulators have tilt

FIG. 57: A magnet power supply for the superconducting magnet which is used to operate the ramp up and down of the magnet.
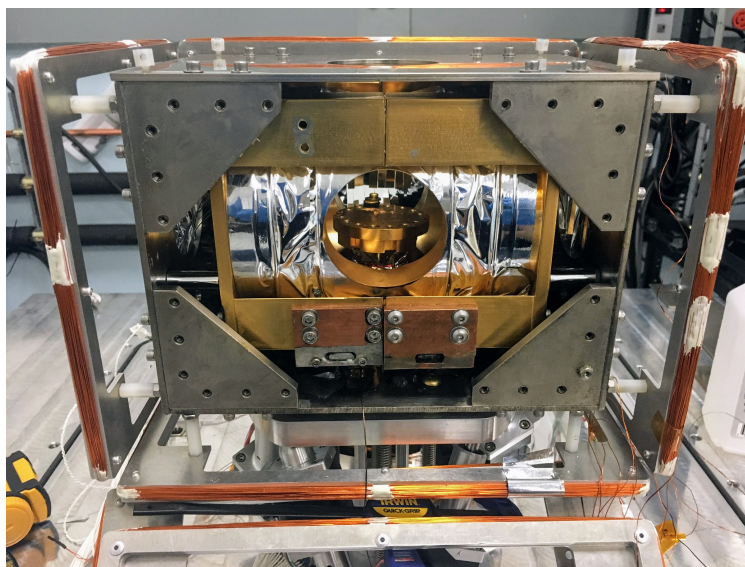
FIG. 58: A partially removed thermal radiation shield showing a gold-plated superconducting magnet structure with NbTi wires hidden behind mylar tapes. It is supported to the radiation shield by G-10 rods to thermally isolate from the 1st stage of the cryocooler. A sample stage can be seen at the center of the magnet system. Surrounding the radiation shield are three pairs of Helmholtz coils.

FIG. 59: Mini Hexapod MHP-14, a six-actuator kinematics platform, that is used to fine adjust the angles and the positions of the superconducting magnet during sample measurements.
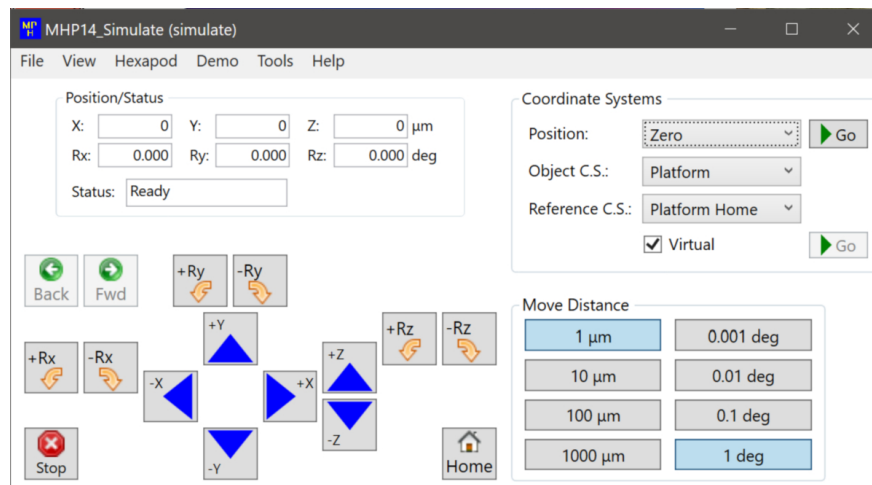
FIG. 60: A Windows software for Hexapod MHP-14 to control the rotation and translation of the hexapod. The position and the rotation can be either manually entered in the top left field, or adjusted in steps by clicking on the arrows.

adjustment which was used to planarize probe tips. The probe arms on the manipulators are thermally anchored to the 1st stage of the cryocooler to reduce the heat load to the sample. The probe tip used in this measurement was Picoprobe® Model 40A (GGB Industries, Inc). shown in Fig. 61. They are fixed at the end of the probe arms and make electrical contact to the sample to send and receive rf power from the network analyzer. The probe is configured with the GSG probe tip, where two outer tips are grounded and the center tip is for carrying the signal, with the tip separation of $100\,\mu$m. Each tip is constructed with an individually spring-loaded BeCu which allows for reliable contacts to the sample surface even under a small vibration. To further minimize the heat load to the sample when the probes make the contact, non-magnetic, low thermal conductivity semi-rigid rf cables by Keycom Corp. are used.
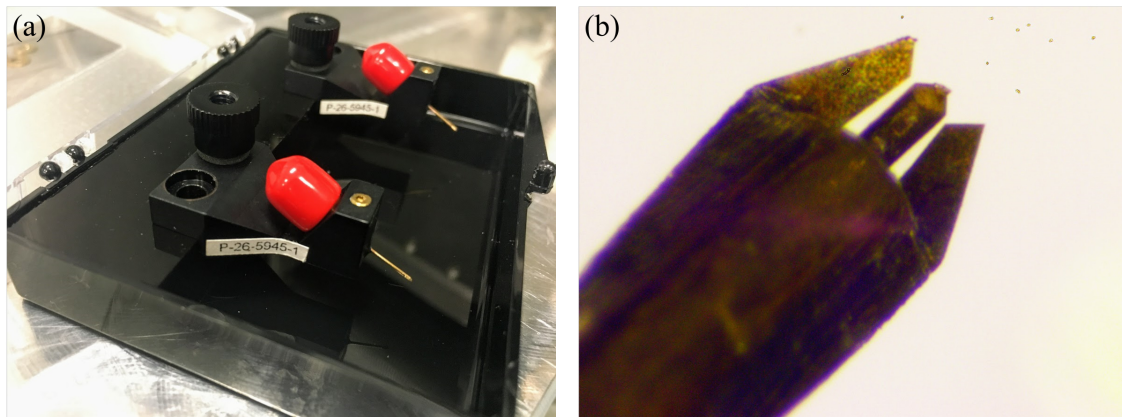
FIG. 61: (a) GSG probe tips used in the measurements to make electrical contacts to the sample. (b) A zoomed-in picture of the probe tips consisting of two ground tips on the outside and one signal tip at the center separated by $100\,\mu$m.

An optical microscope shown in the Fig. 62 is used for viewing and for precise landing of the probes to the contact pads on the resonator. The chamber lid is built with a sapphire window with IR blocking coating for viewing with a microscope while minimizing radiative

heating of the sample. The equipped microscope system is Optem® Zoom 160 which consists of a 2X TV tube and an objective lens yielding a combined optical magnification range of 1.0 to 16.0X. An 18 megapixel USB3.0 CMOS camera is mounted on the microscope and is connected to a computer to display a live feed of the microscope image to a monitor. The setup is capable of $2\,\mu$m resolution. Both an LED ring light and $150\,$W fiber optic light source are used for illuminating the sample.
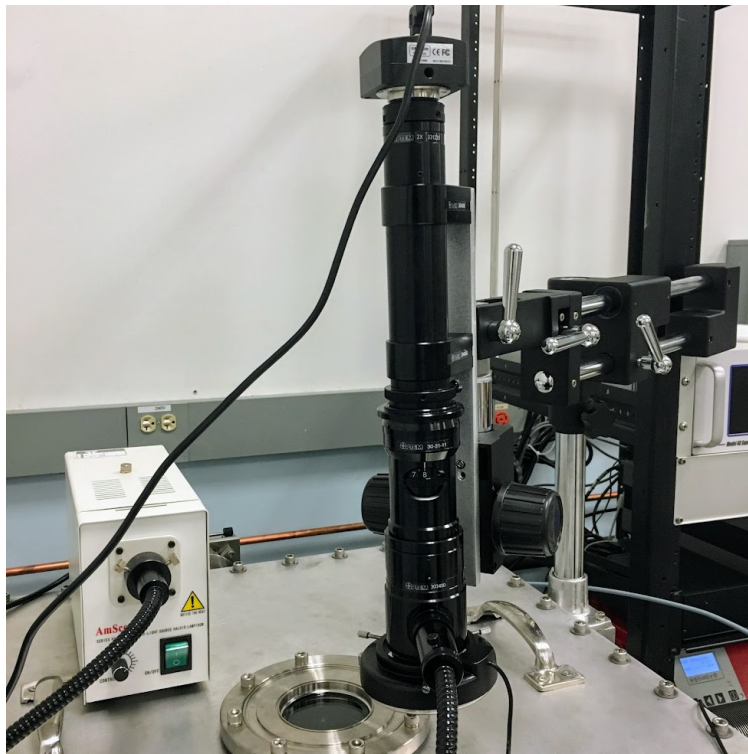
FIG. 62: A microscope system that is fixed to the chamber wall via a boom arm. The LED ring light and the fiber optic light source are attached to the microscope. The USB camera is attached at the top of the microscope for viewing the sample through the viewport on the chamber lid.

The cryocooler produces mechanical vibrations due to periodic compression and expansion of the helium gas inside the cold head. They can couple to the sample stage and the probes which introduce uncertainty in the measurements. There are several features on the CPS that passively isolate vibration. The chamber is placed on top of a pneumatic table with four pressurized legs shown in Fig. 63, which isolates the majority of the vibration from the cryocooler. The cryocooler is indirectly attached to the chamber via a stage shown in
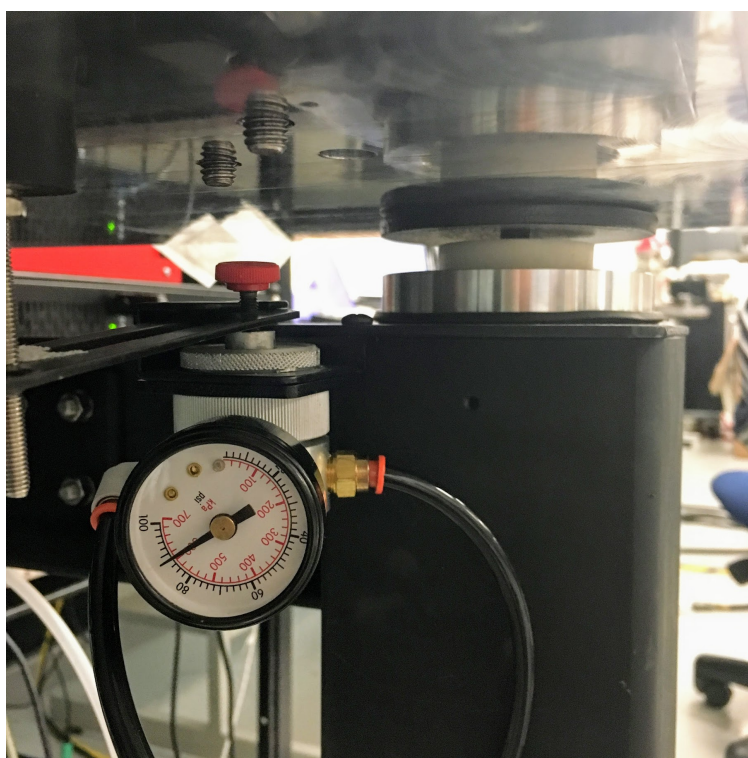
FIG. 63: One of the pneumatic legs supporting the CPS chamber. The pressurized legs provide passive vibration isolation from the cryocooler.

Fig. 64 which connects to the chamber via a flexible bellow. The stage is then fixed to the pneumatic table via four rubber vibration isolators. Finally, flexible tinned copper braids
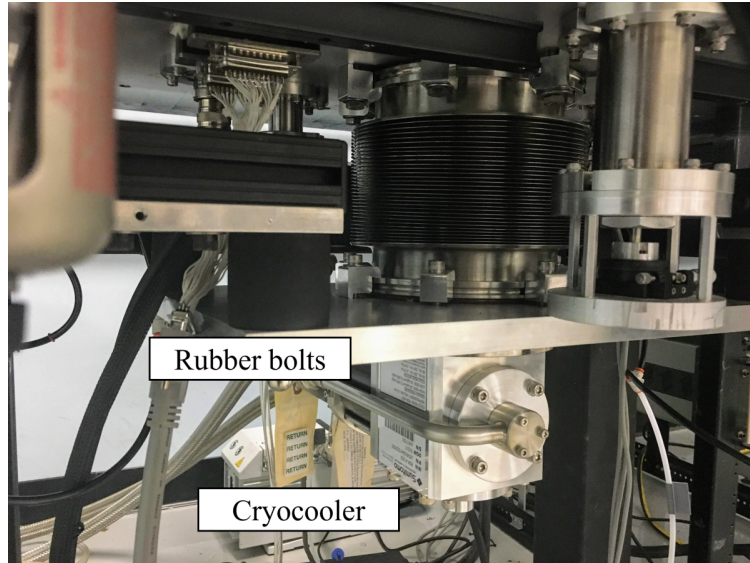
FIG. 64: A setup of the cryocooler underneath the probe station chamber. The cryocooler is bolted upside down with the cold head inside the main chamber where it is connected via a flexible bellow to dampen vibration. It is also supported by four rubber bolts to the pneumatic table.

were used to thermal anchor the superconducting magnet to the second stage to isolate vibrations as shown in Fig. 65. Nevertheless, the probe arms and the sample stage still suffered from residual vibration. The vibration was measured on the sample stage and the tip of one of the probe arms using piezoelectric accelerometers. Figure 66 illustrate the magnitudes of acceleration as a function of time and their Fourier Transforms at the sample stage and the probe arm. The largest spikes in the accelerations occur at a frequency of roughly $1.2\,\mathrm{Hz}$, which corresponds to the expansion and compression cycle of the cryocooler.

7.4 MEASUREMENT SETUP

The patterned sample was mounted on a sample stage using the Ag paint, and a calibration substrate was mounted on a side as shown in the Fig. 67. The chamber was then pumped down to $1 \times 10^{-5}\,\mathrm{Torr}$ and cooled down until the sample stage temperature reached $T \sim 7\,\mathrm{K}$. The calibration substrate is a model CS-5 (GGB Industries, Inc.), which contains several calibration standards specifically designed for the GSG probes. For the measurement,
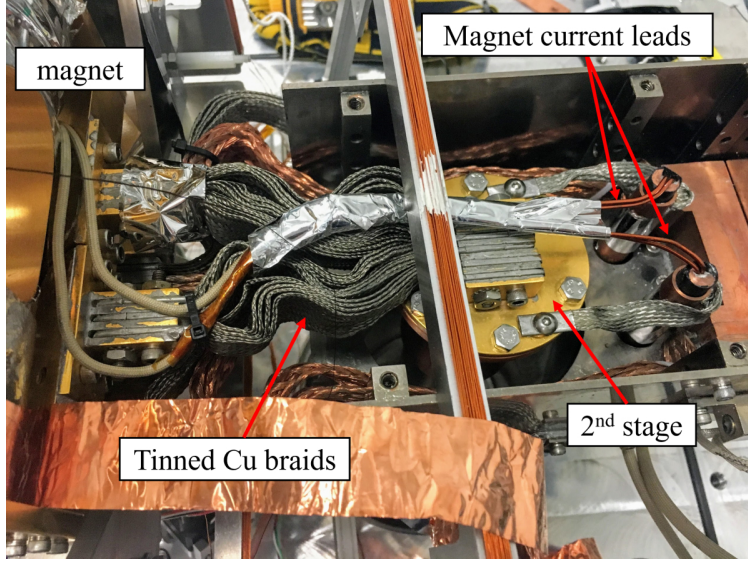
FIG. 65: A picture showing inside of the radiation shield of the 2nd stage. Tinned copper braids are used to isolate vibration from the second stage to the superconducting magnet.

a Short-Open-Load-Thru calibration was used to correct the errors in the measurement system from the probe, cable, and to the network analyzer at a cryogenic temperature. This allows for the error corrections in the same environment that the sample was measured in. At the same time, the probe tips were planarized to ensure the tips were at the same height by adjusting the probe arm rotation until the GSG tips made equal probe marks on the gold substrate. The output port of the VNA provided rf power, and the drive power was selected to be $-30\,\mathrm{dBm}$ while avoiding distortion of the Lorentzian shape in the transmission signal observed at higher power due to nonlinear heating effects [124, 125].

All four S-parameters, $S_{11,22}$ and $S_{12,21}$, were measured for this experiment as a function of temperature and parallel dc field. Any cross talk and phase delays in the transmission spectra were fixed by fitting and correcting the resonant circles, and f_r and Q_L were extracted from the phase vs frequency fit [98]. At each measurement, coupling strengths were calculated by fitting the phase of S_{11} and S_{22} to the formula [19]:

$$\phi(f) = \tan^{-1}\left[\frac{2Q_L}{S(f_r)}\left(\frac{f-f_r}{f_r}\right)\right] - \tan^{-1}\left[2Q_L\left(\frac{f-f_r}{f_r}\right)\right] + \varphi_0, \qquad (135)$$

where $S(f_r)$ is the S_{11} or S_{22} on resonance and φ_0 is any phase delay in the cable. The
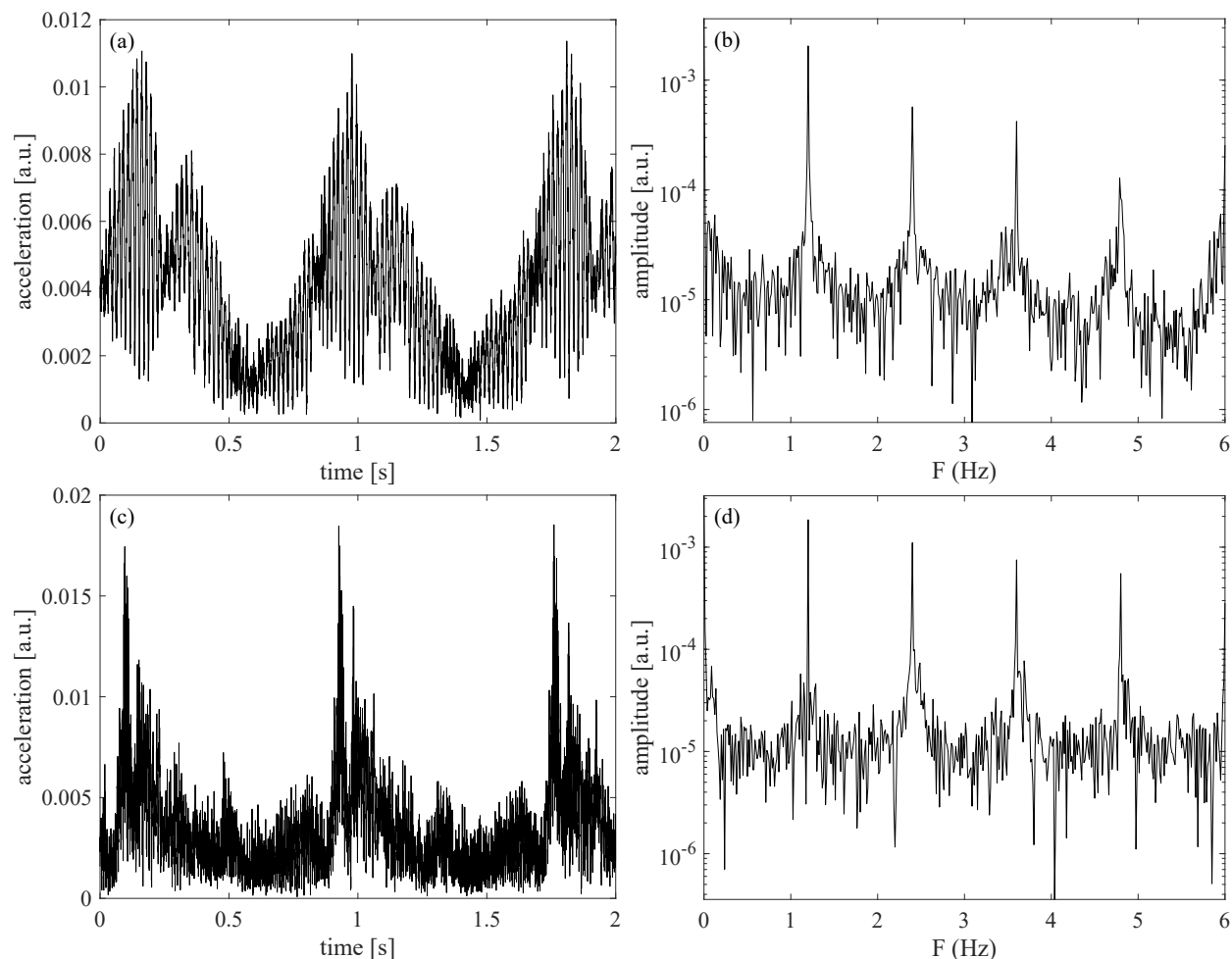
FIG. 66: Measured accelerations using the Piezo accelerometers on (a) the tip of the probe arm and (b) its Fourier Transform. (c) Accelerations on top of the sample stage and (d) its Fourier Transform. There are large spikes of acceleration corresponding to the cycle of the cryocooler gas compression and expansion at a frequency of $\sim 1.2\,\mathrm{Hz}$ despite several implementations to passively isolate such vibrations.
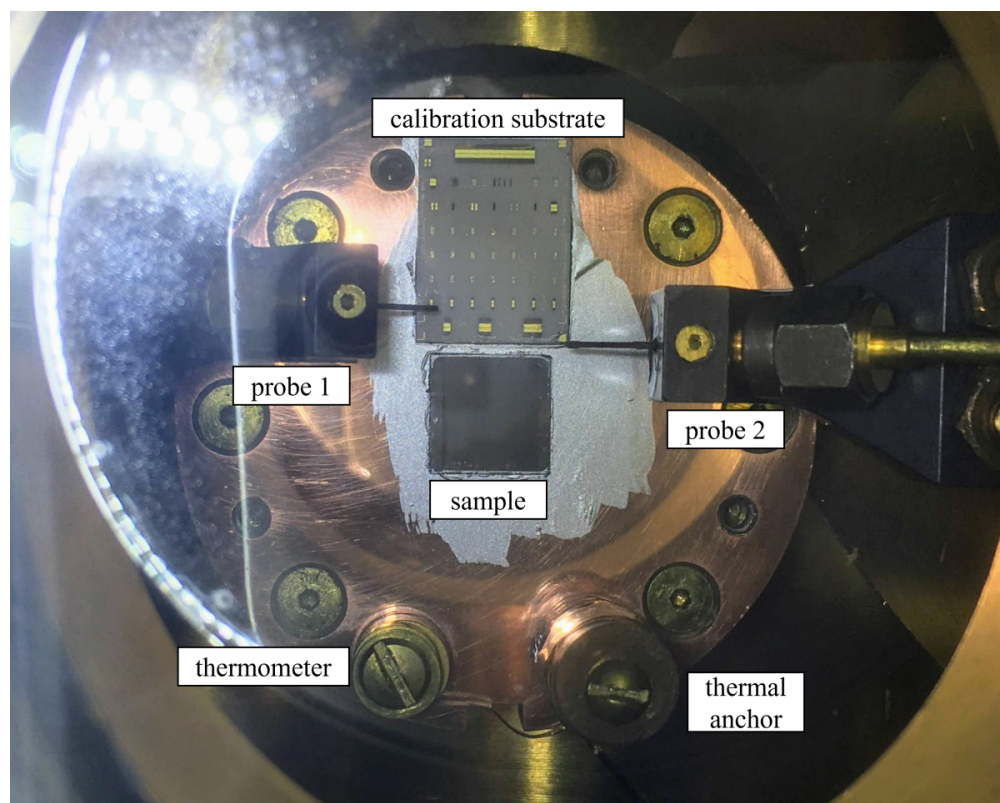
FIG. 67: A photo of the sample, the calibration substrate, and two GSG probes taken from the viewport of the chamber lid. The thermometer and the OFHC Copper bobbin for thermal anchoring of the lead wires are screwed onto the sample stage.

coupling coefficients are then

$$\beta_{1,2} = \frac{1 \pm S_{11,22}(f_r)}{1 \mp S_{11,22}(f_r)}, \tag{136}$$

where the upper sign is used for the overcoupled and the lower sign for the overcoupled resonator. A typical transmission and reflection coefficients of the sample at $T = 7.2\,\mathrm{K}$ are shown in the Fig. 68 along with the nonlinear least-squares fits to extract Q_L, f_r, and coupling coefficients.
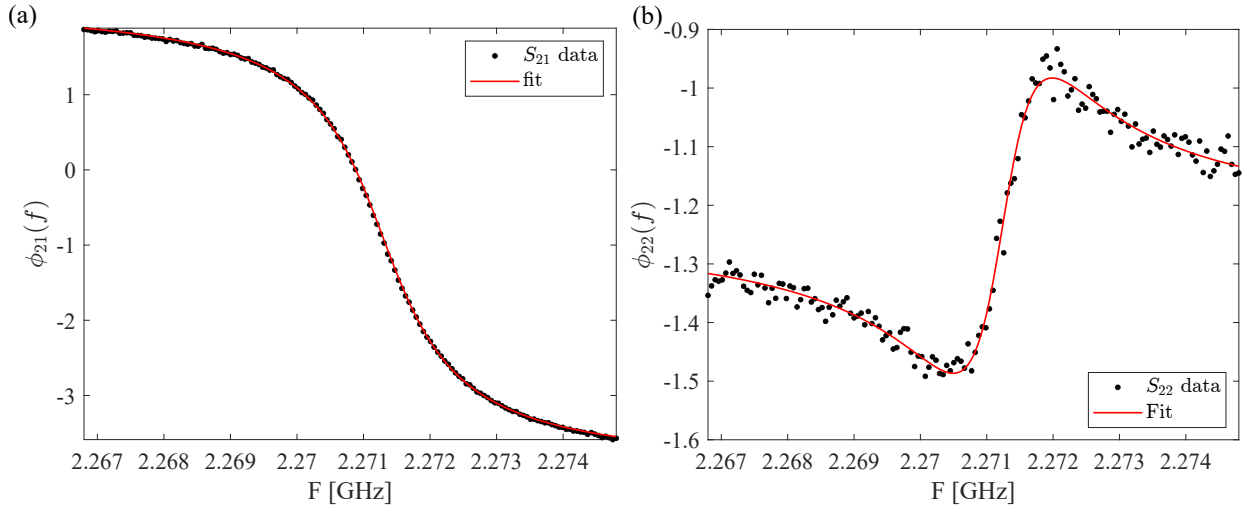
FIG. 68: (a) The phase versus frequency fit of the $S_{21}(f)$ for the Nb$_3$Sn sample measured using the probe station at $T = 7.2\,\mathrm{K}$ and (b) the phase versus frequency fit for the $S_{22}(f)$.

The cryocooler caused some vibrations on the probes while they are in contact with the sample. This caused some spread in measured frequency responses. Multiple frequencies sweeps taken consecutively at the same temperature show fluctuations in Lorentzian shapes as illustrated by the Fig. 69. In analyzing the sample, the transmission and reflection spectra were recorded multiple times at one data point and the average of the extracted f_r and Q_L are reported, with the error bars representing the standard deviation from the repeated measurements.
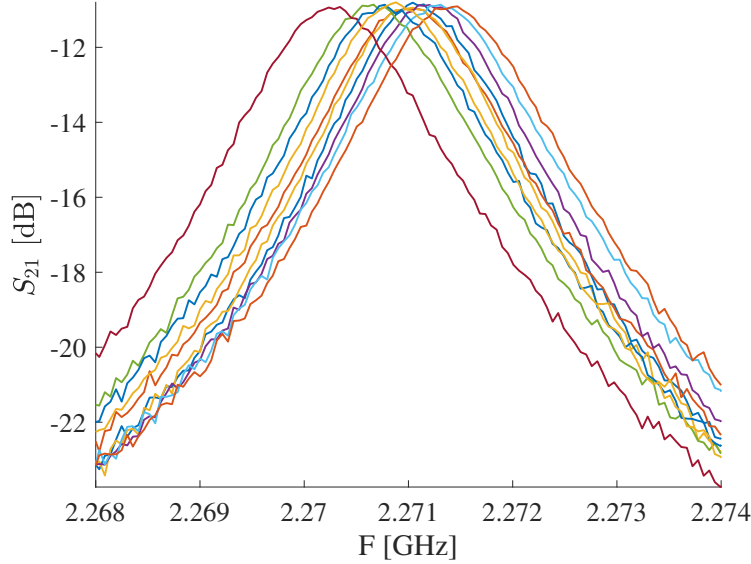
FIG. 69: The measured transmission spectra near resonance taken consecutively without moving probes or changing temperatures. Vibration from the cryocooler couples to the sample stage and probes causing fluctuations in the resonant frequencies.

Data acquisitions were conducted using LabView programs. The first program shown in Fig. 70 was used to connect to CTC100 Temperature Controller and Models 612 Cryogenic Temperature Monitor to record temperatures from all five sensors and also set a desired temperature on the sample stage by accessing the PID controller. A second program shown in Fig. 71 was used to access the VNA to configure measurements and record the transmission and reflection spectra as S2P Touchstone files. Finally, a third program was used to control the ramp-up and down of the superconducting magnet by connecting to the Model 4G power supply.

The lowest stable temperature obtained at the sample stage while landing the probes on the sample was $T = 7\,\mathrm{K}$. For the temperature-dependent measurements, f_r and Q_L were measured from $7\,\mathrm{K}$ to $17\,\mathrm{K}$ with $0.2\,\mathrm{K}$ increments, where the precise temperatures were obtained using the PID controller and the resistive heater on the sample chuck. At each data point, fifty spectra were taken to extract the average f_r and Q_L. The temperature dependencies of $\lambda(T)$ were then inferred from the measured frequency shift $\delta f(T)/f_0 = [f_r(T) - f_r(7\mathrm{K})]/f_r(7\mathrm{K})$.
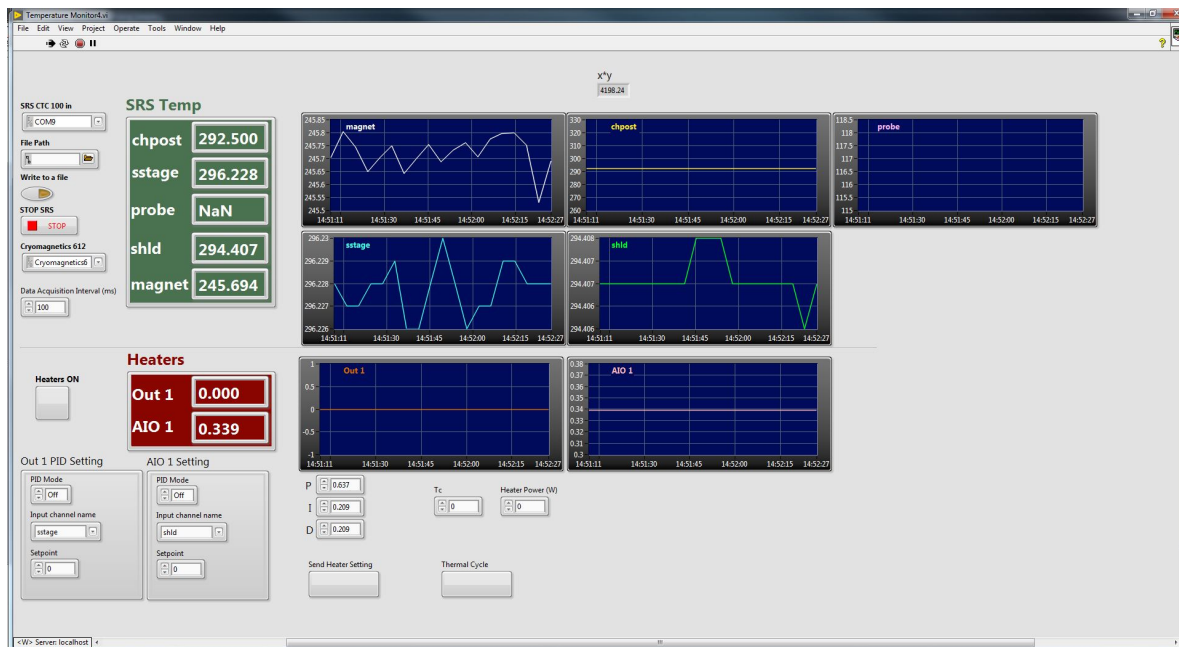
FIG. 70: A LabView program used to monitor all temperature sensors and PID controls.
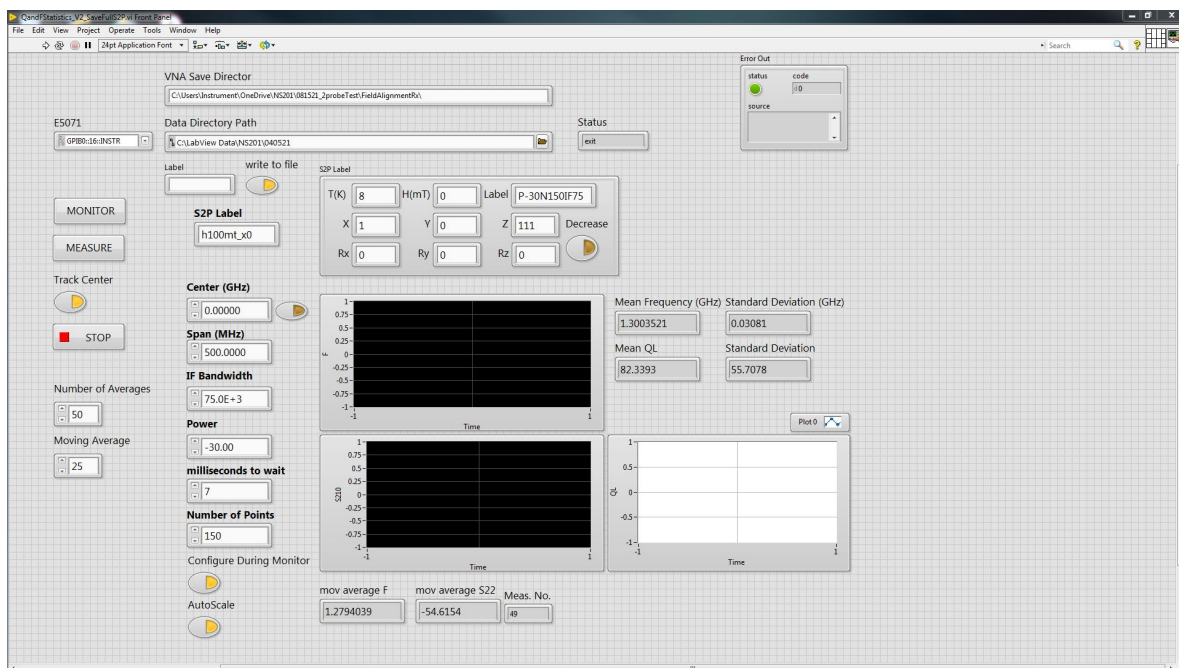
FIG. 71: A LabView program used to configure VNA and record S-parameters.
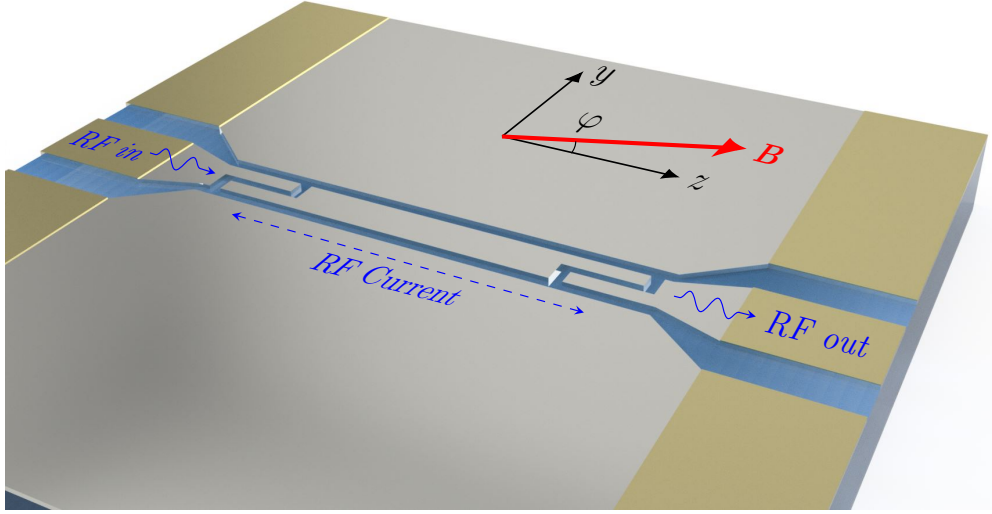
FIG. 72: The coordinate system for the magnet orientation with respect to the direction of the rf current on the coplanar resonator.

To investigate NLME, f_r was measured as a function of parallel dc field up to $200\,\mathrm{mT}$ at temperatures between $7\,\mathrm{K}$ and $13\,\mathrm{K}$. The field was applied in both parallel $\varphi = 0°$ and perpendicular $\varphi = 90°$ field orientations with respect to the strip as indicated by Fig. 72. To conduct field-dependent measurements, the sample was fixed to one temperature, and $f_r(H)$ was measured while increasing the field from 0 to $200\,\mathrm{mT}$ at $10\,\mathrm{mT}$ increments. Once the data was taken at $200\,\mathrm{mT}$, the field was zeroed first, and the sample was warmed up above T_c to expel any trapped vortices in the strip. The sample was then set to a new temperature and the measurements were repeated.

For the NLME measurements, the alignment of the dc field $\mathbf{B}$ to the plane of the strip is crucial to keep the superconductor in the Meissner state and avoid perpendicular vortices penetrating from the film edges. These vortices caused by the misaligned field reduce the quality factor and give rise to an additional field dependence of $\delta f(\mathbf{B}, T)$ unrelated to the NLME. To find the orientation of the magnet which produces $\mathbf{B}$ parallel to the film plane and the minimum amount of flux, the loaded quality factor $Q_L(\mathbf{B})$ and $\delta f(\mathbf{B})$ were measured as a function of the out-of-plane field angle ζ, and we picked an angle that produced the least hysteresis before and after the field ramp. The following steps were taken to find such

an angle:

1. Measure the initial values of f_{0i} and Q_{Li} at zero field.

2. Ramp the field up to $60\,\text{mT}$ and wait for a resonator response to stabilize.

3. Ramp the field down to zero and measure f_{0a} and Q_{La} affected by the number of vortices trapped in the previous field ramp.

4. Thermal cycle the sample above $T_c = 17.2\,\text{K}$ at zero field to flush out trapped vortices.

5. Repeat the measurements after adjusting the magnet to a new angle using the hexapod.

Shown in Fig. 73 are the normalized shifts $\delta f_0/f_0 = (f_{0a} - f_{0i})/f_{0i}$ and $\delta Q_L/Q_L = (Q_{La} - Q_{Li})/Q_{Li}$ as functions of the magnet angle ζ. Both $\delta f_0(\zeta)/f_0$ and $\delta Q_L(\zeta)/Q_L(0)$ peaked at $\zeta = 3.8°$ which was adopted as a magnet orientation producing the dc field parallel to the plane of the film. This procedure is similar to that which was used in Ref. [37].
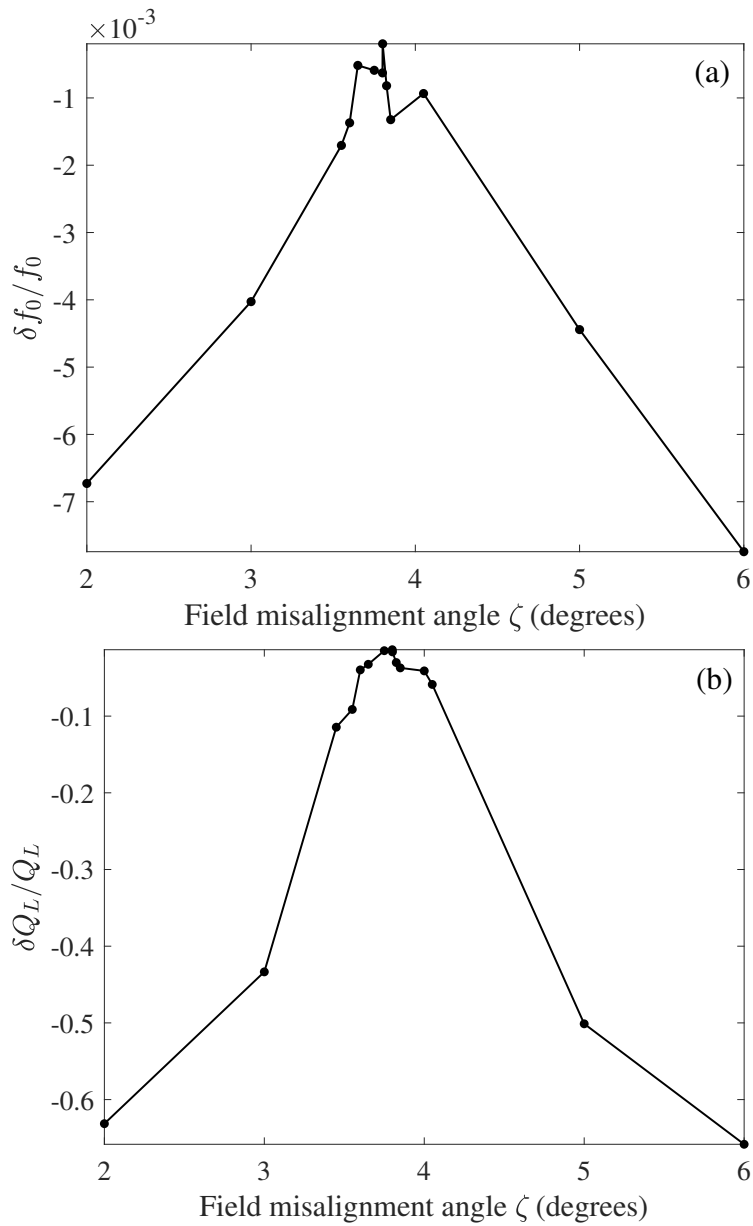
FIG. 73: Normalized shifts in (a) resonant frequencies and (b) loaded quality factors after cycling **B** from 0 to 60 mT and back to 0 as a function of the offset angle ζ. Both $\delta f(\zeta)$ and $\delta Q_L(\zeta)$ are peaked at $\zeta = 3.8°$.

7.5 NB₃SN MEASUREMENT RESULTS

7.5.1 TEMPERATURE DEPENDENCE

Shown in Fig. 74 is the temperature dependent part of $f_r(T)$ along with the fit of the normalized frequency shift:

$$\frac{f_0(T) - f_0(7\text{K})}{f_0(7\text{K})} = \frac{\sqrt{L_g + L_k(7\text{K})}}{L_g + L_k(T)} - 1. \tag{137}$$

Since the film has a thickness $t \ll \lambda(T)$, the kinetic inductance is approximated as

$$L_k \approx \frac{\mu_0 \lambda(T)}{w} \coth\left[\frac{t}{\lambda(T)}\right] \approx \frac{\mu_0 \lambda(T)^2}{wt}, \tag{138}$$

and the two-fluid approximation of the temperature dependence of $\lambda(T) = \lambda(0)\left[1 - (T/T_c)^4\right]^{-1/2}$ is assumed. The fit gives $\lambda(0) = 353\,\text{nm}$, well above the London penetration depth $\lambda(0) \approx 90\,\text{nm}$ for a clean stoichiometric Nb₃Sn [104]. This may result from nonstoichiometric inclusions which cause a slight reduction of T_c in the films [96, 103]. For $\lambda_{eff}(0) = 353\,\text{nm}$, $w = 15\,\mu\text{m}$ and $t = 50\,\text{nm}$, the kinetic inductance can be approximated to be $L_k = \mu_0\lambda^2\lambda(T)/wd \simeq 200\,\text{nH/m}$ which accounts for about 1/3 of the total inductance $L = L_g + L_k$ with $L_g = 420.5\,\text{nH/m}$.

Another factor contributing to the large value of $\lambda(0)$ is the grain boundary structure of the Nb₃Sn films shown in Fig. 52. Sn depletion at grain boundaries results in weak Josephson coupling of crystalline grains [126–128]. These weakly-coupled grain boundaries facilitate preferential penetration of the magnetic field along the network of grain boundaries, causing an increase of the effective λ, as is characteristic of many superconductors with short coherence length, including Nb₃Sn, cuprates, and pnictides [129, 130].

7.5.2 FIELD DEPENDENCE

Shown in Fig. 75 are the observed field dependencies of the frequency shifts for in-plane **B** parallel and perpendicular to the strip. In both cases, $\delta f(B)$ decreases nearly linearly with B above 30-40 mT but flattens at lower fields. Here the slope of $\delta f(B)$ for in-plane **B** parallel to the strip is about twice of the slope of $\delta f(B)$ for in-plane **B** perpendicular to the strip. In the field range $0 < B < 200\,\text{mT}$ of the measurements, the Nb₃Sn film of thickness 50 nm is in the Meissner state as the parallel field B remains below the nominal lower critical field of a vortex in a thin film. In the London approximation [10], the lower critical field is
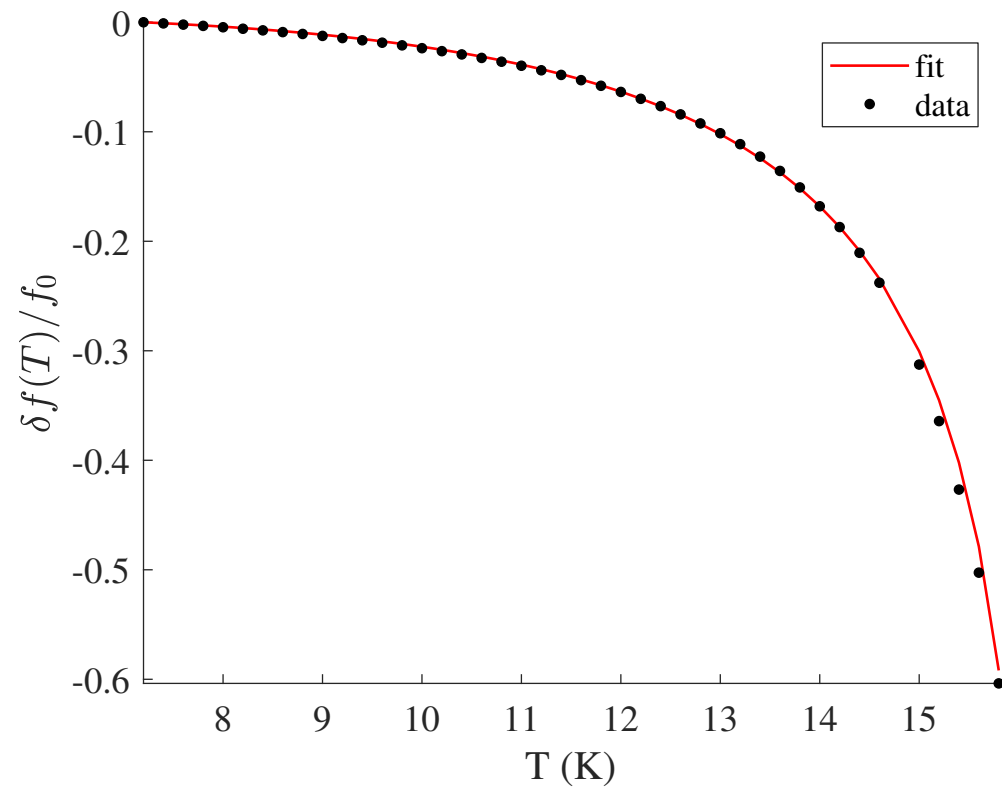
FIG. 74: The normalized temperature-dependent part of the resonant frequency. The fit of the data to Eq. (137) and (138) gives $\lambda(0) = 353\,\mathrm{nm}$.

given as

$$B_{c1} = \left(\frac{2\phi_0}{\pi t^2}\right) \ln\left(\frac{t}{\xi}\right), \tag{139}$$

which yields $B_{c1} \simeq 1.17\,\mathrm{T}$ with $t = 50\,\mathrm{nm}$ and $\xi = 5\,\mathrm{nm}$, exceeding $B_c = 0.54\,\mathrm{T}$ of $\mathrm{Nb_3Sn}$ [131, 132]. The slope of $\delta f(B)$ in Fig. 75 increases with increasing temperature, consistent with the temperature dependence of $\lambda(T)$. The $\delta f(B)$ data exhibit significant scatter, which has also been observed in NLME experiments on cuprates [117]. The error bars in Fig. 75 represent a standard deviation from repeated measurements at each data point. The main contribution to the error bars comes from vibrations of the sample stage and the GSG probes which are coupled from the cryocooler cycles. For the NLME measurements with $\mathbf{B}$ perpendicular to the strip, longer probe arms had to be used, which increased the amplitude of vibrations.

7.5.3 DISCUSSION

The nonlinear Meissner effect correction to the L_k caused by the pair breaking Meissner screening current has a quadratic dependence in B given by [112]

$$\delta L_k = \frac{\mu_0 \lambda^2}{3tw} \left(\frac{\pi \xi t B}{\phi_0}\right)^2 \left[1 + \frac{2\sin^2\varphi}{1 + (\omega\tau/2)^2)}\right], \tag{140}$$

where ϕ_0 is the flux quantum, φ is the field orientation with respect to the rf current, and τ is an effective relaxation time of the superconducting order parameters [76, 133]. The frequency shift is then

$$\frac{\delta f}{f} = -\frac{\mu_0 \lambda^2}{6wtL_g} \left(\frac{\pi \xi t B}{\phi_0}\right)^2 \left(\frac{1}{4} + \frac{2\sin^2\varphi}{4 + \omega^2\tau^2}\right). \tag{141}$$

For $\omega\tau \ll 1$, $t = 50\,\mathrm{nm}$, $\xi = 5\,\mathrm{nm}$, $\varphi = \pi/2$ and $B = 100\,\mathrm{mT}$, the predicted frequency shift is $\delta f(B)/f_0 \approx 4 \times 10^{-4}$. well below the observed $\delta f/f_0$. Moreover, according to Eq. (141), the field induced shift in frequency at $\varphi = \pi/2$ for which the dc field is parallel to the rf currents in the strip is three times larger than δf at $\varphi = 0$. This is inconsistent with the experimental results where the slope of the $\delta f(B)/f_0$ at $\varphi = 0$ from Fig. 75(a) is about two times larger than for $\delta f(B)/f_0$ at $\varphi = \pi/2$ shown in Fig. 75(b). Not only is the Meissner pairbreaking too weak to account for the observed $\delta f/f_0$, but it also yields the field and orientational dependencies of $\delta f(\mathbf{B})/f_0$ inconsistent with the experimental data on $\mathrm{Nb_3Sn}$.

A significant contribution to L_k can come from local non-stoichiometry, strains, and grain boundaries in polycrystalline $\mathrm{Nb_3Sn}$. Particularly, Sn depletion at the grain boundaries results in weak Josephson coupling of grains in $\mathrm{Nb_3Sn}$ [126–128, 134]. If weakly coupled
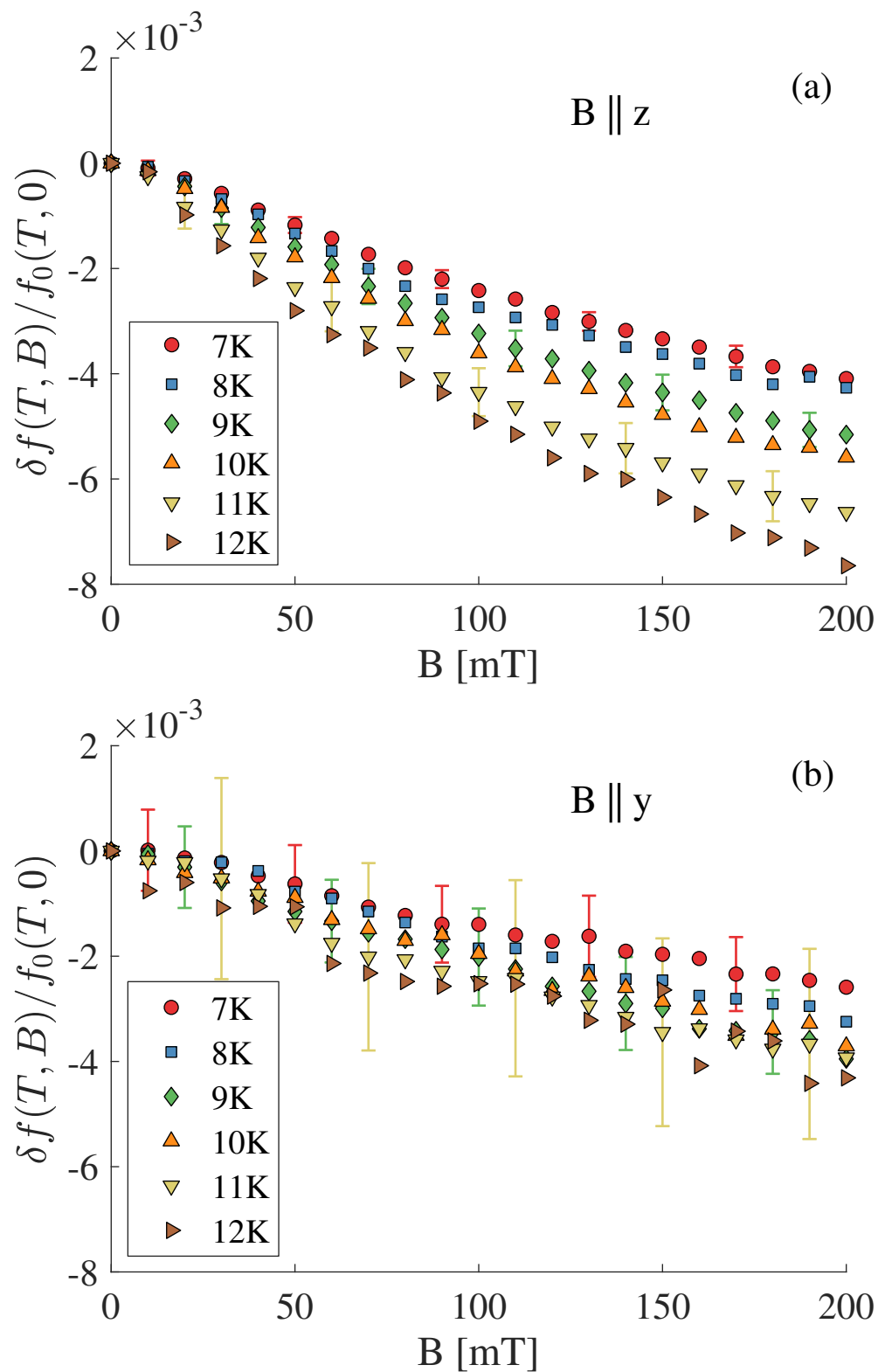
FIG. 75: Normalized frequency shift $\delta f_0(T,B)/f_0(T,0)$ as a function of the in-plane dc magnetic field (a) parallel and (b) perpendicular to the strip.

grain boundaries are regarded as planar Josephson junctions, each grain boundary has a kinetic inductance of

$$L_j = \frac{\phi_0}{2\pi I_c \cos\theta},$$ (142)

where $I_c(T)$ is a critical current of the Josephson junctions, and θ is the sum of the phase difference between the superconducting order parameters around the grains and the phase difference induced by the dc magnetic field [135]. The field induced phase factor is given as

$$\theta_A = \frac{2\pi}{\phi_0} \int \mathbf{A} \cdot d\mathbf{l},$$ (143)

where $\mathbf{A}$ is the magnetic vector potential, the integration is from one superconductor of the grain to the other, and $\mathbf{l}$ is the unit normal to the plane of the grain boundary [7, 135]. If the grain boundaries form interfaces across the cross-section of the strip, they can significantly increase L_k because Nb$_3$Sn can have broad distributions of sizes and I_c values. A model of the grain boundary in the strip can be represented as a rectangular plane as shown in the Fig. 76, where L_1 is in the order of the film thickness $\simeq 50\,\text{nm}$ and $L_2 \sim 0.1\text{--}1\,\mu\text{m}$ as shown in Fig. 52. The phase differences from an array of weakly coupled grain boundaries are
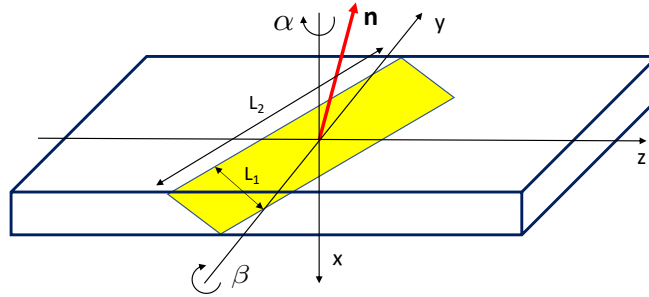
FIG. 76: Geometry of a rectangular tilted grain boundary (yellow). The red arrow shows the normal to the grain boundary plane.

modeled by $\langle\cos\theta\rangle$ averaged over randomly oriented planar grain boundaries parameterized

by the Euler angles α and β from Fig. 76. The results of $\langle \cos \theta \rangle$ calculated in Ref. [112] are

$$\langle \cos \theta \rangle = \frac{1}{\pi^2 b} \int_0^\pi d\alpha \int_0^\pi d\beta \sin(b \cos \alpha \sin \beta) \frac{\cos \alpha \cos \beta}{\tan \beta}, \tag{144}$$

for the dc field **B** parallel to the rf current, and

$$\langle \cos \theta \rangle = \frac{1}{\pi^2 b} \int_0^\pi d\alpha \int_0^\pi d\beta \sin(b \sin \alpha \sin \beta) \frac{\cos \alpha \cos \beta}{\tan \alpha \tan \beta}, \tag{145}$$

for the field perpendicular to the rf current, where $b = B/B_0$ and $B_0 \simeq \phi_0/3\pi dl_2$. Numerical calculation of Eq. (144) and Eq. (145) yields the field dependencies of the average kinetic inductance per unit length $L_k^J \sim \langle L_j \rangle / l_2$ by the weakly coupled grain boundaries with $I_c \sim twJ_c$:

$$L_k^J \sim \frac{\phi_0}{2\pi J_c wtl_2 \langle \cos \theta \rangle}. \tag{146}$$

The fit of the observed normalized frequency shift $\delta f(T, B)/f_0(T, 0)$ to the grain boundary model depends on many uncertain parameters such as distribution of orientations and local I_c values of the grain boundaries, their geometrical sizes and mechanisms of current transport through grain boundaries. Shown in Fig. 77 is an example of $\delta f(T, B)/f_0(T, 0)$ calculated for uniform distributions of the Euler angles of the grain boundaries given as

$$\frac{\partial f(T, B)}{f_0(T, 0)} = \sqrt{\frac{L + L_j(0)}{L + L_j(B)}} - 1, \tag{147}$$

$$= \sqrt{\frac{1 + a\epsilon(T)/\langle \cos \theta(0) \rangle}{1 + a\epsilon(T)/\langle \cos \theta(B) \rangle}} - 1, \tag{148}$$

where L is the geometric inductance, $a = L_j(0, 0)/L$, the factor $\epsilon(T) = [1 - (T/T_c)^4]^{-2}$ approximates the temperature dependence of I_c in Eq. (142), and $\langle \cos \theta \rangle$ are given in Eq. (144) and Eq. (145). The plots in Fig. 77 are calculated with $a = 3.5 \times 10^{-4}$ and $B_0 = 10\,\mathrm{mT}$. The model captures the observed features of $\partial f(T, B)/f_0(T, 0)$ for both orientations of **B** shown in Fig. 75, although a perfect fit from such a crude model can hardly be expected.

The plot shows that the grain boundary contribution to the kinetic inductance can radically change the behavior of field dependence compared to the pair breaking NLME. First, the grain boundary contribution L_j is quadratic in B only at very low fields $B \lesssim B_0 \ll B_c$ and exhibits a nearly linear field dependence at $B \gtrsim B_0 \ll B_c$, in contrast to the Meissner pairbreaking δL_k that is proportional to B^2 all the way to $B = B_c$. Second, the field B applied along the rf current causes stronger increase of $L_j(B)$ than the perpendicular field,
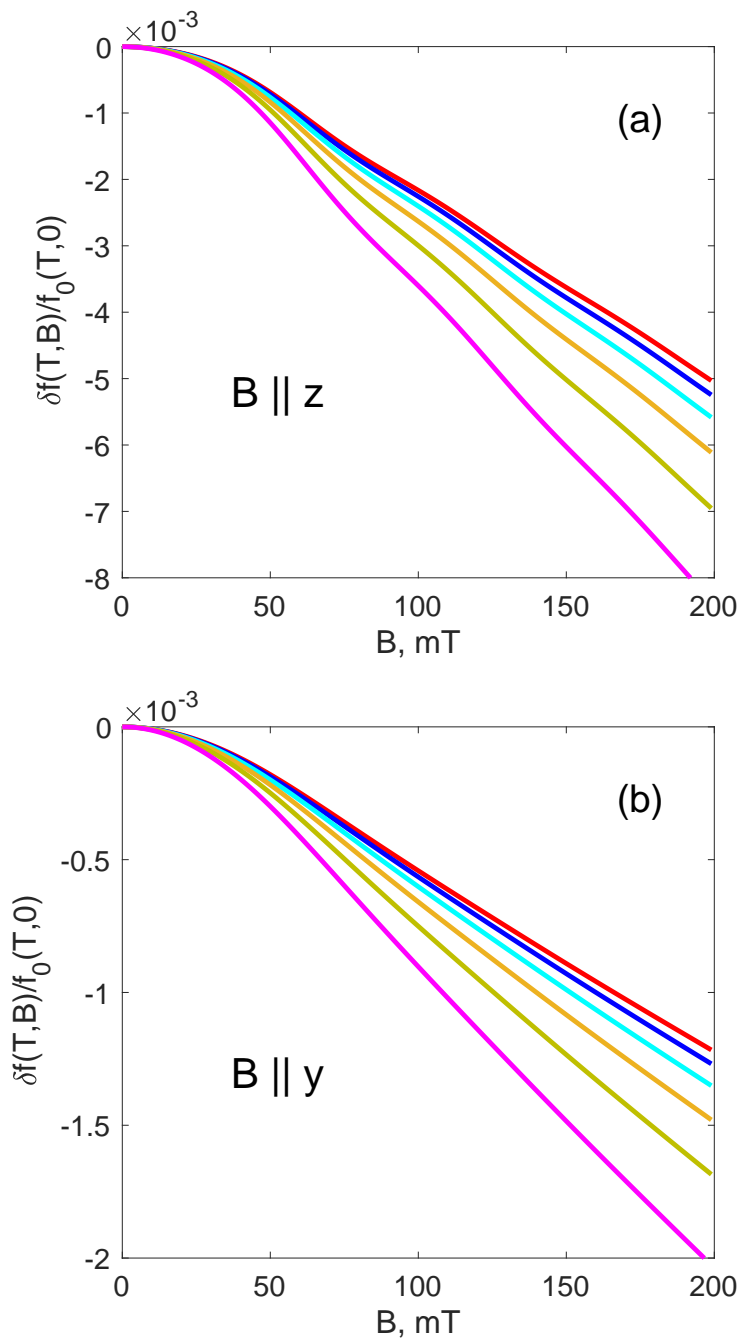
FIG. 77: Normalized shift in $\delta f_0(T,B)/f_0(T,0)$ as a function of field calculated from Eqs. (124), (144) and (145) at $B_0 = 10\,\mathrm{mT}$, $L_k^J(0,0)/L = 3.5 \times 10^{-4}$ and different temperatures corresponding to those in Fig. 75 for: (a) $\mathbf{B}\|z$ and (b) $\mathbf{B}\|y$.

which is opposite of the orientational field dependence of $\delta L_k(B)$ described by the Eq. (141) and observed on Nb coplanar resonator [37]. Both of these features of L_j are in agreement with the observed $\delta f(B)/f_0$ data of the polycrystalline Nb$_3$Sn film as shown in Fig. 141.

The grain boundaries can also contribute to the field-dependent resistance. The impedance of the grain boundaries are given as

$$Z = \left(\frac{1}{R_\square} + \frac{1}{i\omega\langle L_k^J \rangle} \right)^{-1},$$ (149)

where $R_\square$ is the grain boundary quasiparticle resistance per unit area averaged over the grain boundary orientations. Taking the real part of the impedance yields the field-dependent grain boundary resistance:

$$R_j(B) \sim \frac{\omega^2}{wtl_2 R_\square} \langle L_k^J \rangle^2.$$ (150)

For $\langle L_k^J(B) \rangle$ calculated for Fig. 77, $R_j(B) \propto B^2$ and increases quadratically with B at $B \gtrsim B_0$. Thus, grain boundaries can give rise to a strong nonlinearity of the electromagnetic response of polycrystalline films. This is a particularly important issue for Nb$_3$Sn applications of the SRF cavity, where the thin-film coatings of Nb$_3$Sn are applied on top of the Nb SRF cavities [23, 96, 128, 134].

7.6 CONCLUSION

This measurement has shown that the grain boundaries in the polycrystalline film contribute significantly to the NLME in the film. In contrast to elemental superconductors such as Nb [37] and Al [136] that exhibit $L_k \propto B^2$ dependencies described by pair breaking Meissner current, the polycrystalline Nb$_3$Sn film has shown nearly linear dependence of B, as expected from the clean d-wave superconductors. This finding raises an alternative interpretation of nonlinear Meissner effect data used to detect the structure of order parameters in d-wave superconductors. Specifically, our results emphasize the importance of having single crystals for measuring the nonlinear Meissner effect to obtain information about the gap shape, particularly in cuprates and pnictides prone to weak-link behavior of grain boundaries.

Our results also revealed the potentially strong field dependence of the resistances across the grain boundaries. The calculation shows that the resistance across the grain boundaries can increase quadratically with B for a field greater than B_0, determined by the characteristics of the grains on the film. The actual impact of the grain boundaries on the performance

of the Nb$_3$Sn cavity will depend on numerous factors including density of the grain boundaries and specific resistance across the grain boundaries, and it remains to be a future task to investigate the field dependent losses rising from grain boundaries on thin films.

CHAPTER 8

CONCLUSION

Two nitrogen-doped Nb cavities and a standard Nb cavity were tested with the temperature map to study the quenching mechanism. While the standard cavity exhibited heating of $\Delta T \sim 500\,\mathrm{mK}$ on hot spots prior to quenching, nitrogen-doped cavities only showed $\Delta T \sim 10\,\mathrm{mK}$ at most. Thus, it was concluded that the nature of the quench in the nitrogen-doped cavity is mot likely magnetic, where the phase transition occurs by exceeding the critical magnetic field in a local region. It was also observed that the faster cool-down can create a spatial temperature gradient during the cool down across T_c and improve Q_0 by almost a factor of two.

To get an insight into the mechanism by which the nitrogen doping improves the Q_0, the cold spots samples from the nitrogen-doped and the standard Nb cavities were investigated using the STM. The tunneling spectra were obtained by either crashing the STM tip into the native surface to break the thick oxide layer, or by first cleaning the oxide layer with Ar-ion sputtering. The collected data were then analyzed using a simple, phenomenological Dynes formula and also with a more robust modified DOS that modeled a superconductor with a thin layer of proximity coupled normal layer. This model represented the presence of metallic suboxide layers within the natural oxide layer of the Nb surface and described the DOS with two additional dimensionless parameters, α and β, quantifying the thickness of the normal layer and the contact resistance between the normal and the superconducting layer [70].

The results of both tunneling methods showed a striking difference between the surface of the nitrogen-doped and standard Nb samples. The measurements revealed that nitrogen doping has the following effect on the surface:

1. It lowers the average Δ

2. It reduces spatial inhomogeneity in Δ values

3. It reduces the thickness of the metallic oxides by partially converting them into semi-conducting or dielectric oxides.

4. It reduces spatial inhomogeneity of the contact resistance by eliminating its low- and high-values

The results provided an insight into a possible scenario by which nitrogen doping can improve the quality of the SRF cavity. The nitrogen doping may be improving the surface condition by bringing material properties toward optimal values that minimize R_s, mostly by shrinking the metallic suboxide layer. These changes caused by nitrogen doping could be reducing the material broadening of gaps peaks in DOS, such that the broadening induced by the rf field becomes more significant; hence, the reduction of $R_s(B_p)$ with the field as seen in nitrogen-doped cavities can take place. The results of this work showed that altering surface structure leads to performance boost in SRF cavity, and they can give new insights into material treatment and surface nanostructuring for the future of SRF cavities.

As a part of an R&D effort to develop SRF cavities with alternative materials to reach efficiency beyond Nb, an experimental setup for SRF thin film evaluations was designed and developed. A CPW resonator that can be patterned onto a $10\,\text{mm} \times 10\,\text{mm}$ sized thin film to achieve a resonant frequency of $\sim 3\,\text{GHz}$ was designed. This special pattern and the housing of the sample allow for testing of the film without making physical contact with the input and to output rf ports. The input and output antennas couple the rf power to the resonator capacitively, which completely removes the process of fabricating reliable, ohmic contacts to the resonators. The housing was designed using the finite-element electromagnetic simulator to analyze any parasitic losses and resonant modes before fabrication, and the setup was also tested using both Nb and OFHC Cu housing to guarantee any losses from the housing were negligible.

The new probe-coupled CPW resonator was tested first on a Nb film, and its superconducting properties were calculated by numerically analyzing the geometric factor and kinetic inductance. The results showed good agreement with the BCS theory and known properties of the Nb films, which indicate that the experiment can successfully perform rf characterization of the film at low power. Additionally, Nb_3Sn and NbTiN films were tested on this device. Although the results could not be fit fully with the BCS predicted $R_s(T)$, the measured $R_s(T)$ of those films were comparable to that of Nb film. One of the reasons Nb_3Sn film did not agree well with the BCS calculation may be due to nonstoichiometric compounds with weakened superconductivity.

In addition to the probe-coupled resonator technique, a cryogenic probe station was set up to perform rf characterization with dc magnetic field parallel to the surface. The probe station uses manipulators to land probe tips to the sample to send and received rf signals;

therefore, proper landings pads free of oxide must be deposited on the film. Although the temperature of the film is limited to $> 7\,\mathrm{K}$, the probe station is a liquid helium free system that uses a cryocooler, which simplifies and reduces the cost of sample testing. Furthermore, the probe station is equipped with a superconducting magnet capable of producing a dc magnetic field of up to 1 Tesla.

Using the cryogenic probe station, the nonlinear Meissner effect on a thin Nb_3Sn film was studied. The resonant frequency was measured as a function of the in-plane field both in parallel with and perpendicular to the direction of the rf current in the resonator. The field dependency was measured up to $200\,\mathrm{mT}$, which is well below the first critical field that was enhanced to $\simeq 1$ T due to the film thickness being much less than λ. Interestingly, the results showed a linear dependence of frequency with the field, as opposed to a quadratic dependence, as expected from a conventional s-wave superconductor. It was found that the weakly coupled grain boundaries can have a more significant contribution to the kinetic inductance compared to the pair breaking Meissner current in a polycrystalline Nb_3Sn film. The results of the experiment bring to the table an alternative interpretation of the nonlinear Meissner effect, particularly when analyzing for the structure of order parameters in d-wave superconductors. It also emphasizes the requirement for single crystals in measuring the nonlinear Meissner effect to understand the gap shape in high-temperature superconductors.

For future work on the rf characterization of the thin films, it would be beneficial to cross-check the superconducting properties extracted from the probe-coupled resonator and probe station with rf characterization performed using other methods involving host cavities. It would further validate the experimental procedure and help demonstrate the CPW resonator technique as a robust technique for benchmarking SRF thin film samples. As for the cryogenic probe station, lowering the useful temperature range will broaden the range of the samples that can be tested and mitigating vibration is still a challenge that should be addressed to improve the measurement accuracy. As a new generation of the SRF films such as Nb_3Sn and SIS multilayer is emerging as a promising alternative to Nb for achieving more efficient operation of accelerators, it is important to establish rf characterization method that can potentially bridge a gap between RF performance of thin film samples to the bulk cavity.

BIBLIOGRAPHY

[1] P. Dhakal, G. Ciovati, and G. R. Myneni, A path to higher Q_0 with large grain niobium cavities, in Proc. of IPAC2012 (2012).

[2] A. Grassellino, A. Romanenko, D. Sergatskov, O. Melnychuk, Y. Trenikhina, A. Crawford, A. Rowe, M. Wong, T. Khabiboulline, and F. Barkov, Nitrogen and argon doping of niobium for superconducting radio frequency cavities: a pathway to highly efficient accelerating structures, Supercond. Sci. Technol. **26**, 102001 (2013).

[3] J. Stohr, *Linac Coherent Light Source II (LCLS-II) Conceptual Design Report*, tech. rep. (SLAC National Accelerator Lab., 2011).

[4] S. Posen, J. Lee, D. N. Seidman, A. Romanenko, B. Tennis, O. S. Melnychuk, and D. A. Sergatskov, Advances in Nb_3Sn superconducting radiofrequency cavities towards first practical accelerator applications, Supercond. Sci. Technol. **34**, 025007 (2021).

[5] C. J. Gorter and H. B. G. Casimir, On supraconductivity I, Physica **1**, 306 (1934).

[6] F. London and H. London, The electromagnetic equations of the supraconductor, Proc. R. Soc. A **149**, 71 (1935).

[7] M. Tinkham, *Introduction to Superconductivity*, Second (Dover Publications Inc., Mineola, USA, 1996).

[8] A. B. Pippard, An experimental and theoretical study of the relation between magnetic field and current in a superconductor, Proc. R. Soc. A **216**, 547 (1953).

[9] V. L. Ginzburg and L. D. Landau, On the theory of superconductivity, Sov. Phys. JETP **20**, 1066 (1950).

[10] A. A. Abrikosov, On the magnetic properties of superconductors of the second group, Sov. Phys. JETP **5**, 1174 (1957).

[11] J. Bardeen, L. N. Cooper, and J. R. Schrieffer, Theory of superconductivity, Phys. Rev. **108**, 1175 (1957).

[12] C. A. Reynolds, B. Serin, W. H. Wright, and L. B. Nesbitt, Superconductivity of isotopes of mercury, Phys. Rev. **78**, 487 (1950).

[13] E. Maxwell, Isotope effect in the superconductivity of mercury, Phys. Rev. **78**, 477 (1950).

[14] H. Frohlich, Theory of the superconducting state. I. The ground state at the absolute zero of temperature, Phys. Rev. **79**, 845 (1950).

[15] H. Frohlich, Interaction of electrons with lattice vibrations, Proc. R. Soc. A **215**, 291 (1952).

[16] J. Bardeen and D. Pines, Electron-phonon interaction in metals, Phys. Rev. **99**, 1140 (1955).

[17] L. N. Cooper, Bound electron pairs in a degenerate Fermi gas, Phys. Rev. **104**, 1189 (1956).

[18] N. N. Bogoliubov, On a new method in the theory of superconductivity, Il Nuovo Cimento **7**, 794 (1958).

[19] M. J. Lancaster, *Passive Microwave Device Applications of High-Temperature Super-conductors* (Cambridge University Press, Cambridge, UK, 1997).

[20] K. Fossheim and A. Sudbo, *Superconductivity: Physics and Applications* (John Wiley & Sons Ltd, Chichester, UK, 2004).

[21] J. Zmuidzinas, Superconducting microresonators: physics and applications, Annu. Rev. Condens. Matter Phys. **3**, 169 (2012).

[22] M. Abramowitz and I. A. Stegun, *Handbook of Mathematical Functions* (Dover Publications, New York, USA, 1972).

[23] A. Gurevich, Theory of RF superconductivity for resonant cavities, Supercond. Sci. Technol. **30**, 034004 (2017).

[24] D. C. Mattis and J. Bardeen, Theory of the anomalous skin effect in normal and superconducting metals, Phys. Rev. **111**, 412 (1958).

[25] J. Halbritter, *KFK-Extern 3/70-6* (Karlsruhe, 1970).

[26] H. Padamsee, J. Knobloch, and T. Hays, *RF Superconductivity for Accelerators* (Wiley-VCH Verlag GmbH, Weinheim, Germany, 2008).

[27] J. Knobloch, "Advanced thermometry studies of superconducting radio-frequency cavities", PhD thesis (Cornell University, 1997).

[28] J. M. Sage, V. Bolkhovsky, W. D. Oliver, B. Turek, and P. B. Welander, Study of loss in superconducting coplanar waveguide resonators, J. Appl. Phys. **109**, 063915 (2011).

[29] H. J. Li, Y. W. Wang, L. F. Wei, P. J. Zhou, Q. Wei, C. H. Cao, Y. R. Fang, Y. Yu, and P. H. Wu, Experimental demonstrations of high-Q superconducting coplanar waveguide resonators, Chi. Sci. Bull. **58**, 2413 (2013).

[30] P. K. Day, H. G. Leduc, B. A. Mazin, A. Vayonakis, and J. Zmuidzians, A broadband superconducting detector suitable for use in large arrays, Nature **425**, 817 (2003).

[31] R. J. Schoelkopf and S. M. Girvin, Wiring up quantum systems, Nature **451**, 664 (2008).

[32] M. H. Devoret and R. J. Schoelkopf, Superconducting circuits for quantum information: an outlook, Science **339**, 1169 (2013).

[33] H. Malissa, D. I. Schuster, A. M. Tyryshkin, A. A. Houck, and S. A. Lyon, Superconducting coplanar waveguide resonators for low temperature pulsed electron spin resonance spectroscopy, Rev. Sci. Instrum. **84**, 025116 (2013).

[34] C. Clauss, D. Bothner, D. Koelle, R. Kleiner, L. Bogani, M. Scheffler, and M. Dressel, Broadband electron spin resonance from 500 MHz to 40 GHz using superconducting coplanar waveguides, Appl. Phys. Lett. **102**, 1 (2013).

[35] J. C. Booth, J. A. Becall, D. C. DeGroot, D. A. Rudman, R. H. Ono, J. R. Miller, M. L. Chen, S. H. Hong, and Q. Y. Ma, Microwave characterization of coplanar waveguide transmission lines fabricated by ion implantation patterning of $YBa_2Cu_3O_{7-\delta}$, IEEE Trans. Appl. Supercond. **7**, 2780 (1997).

[36] W. Rauch, E. Gornik, G. Sölkner, A. A. Valenzuela, F. Fox, and H. Behner, Microwave properties of $YB_2Cu_3O_{7-x}$ thin films studies with coplanar transmission line resonators, J. Appl. Phys. **73**, 1866 (1993).

[37] N. Groll, A. Gurevich, and I. Chiorescu, Measurements of the nonlinear Meissner effect in superconducting Nb films using resonant microwave cavity: A probe of unconventional order parameter, Phys. Rev. B **81**, 020504(R) (2010).

[38] A.-M. Valente-Feliciano, Superconducting RF materials other than bulk niobium: a review, Supercond. Sci. Technol. **29**, 113002 (2016).

[39] D. M. Pozar, *Microwave Engineering* (John Wiley & Sons, Hoboken, USA, 2012).

[40] R. E. Collin, *Foundations of Microwave Engineering* (McGraw-Hill, New York, USA, 1992).

[41] R. K. Hoffmann, *Handbook of Microwave Integrated Circuits* (Artech House, Norwood, USA, 1987).

[42] L. G. Maloratsky, *Passive RF & Microwave Integrated Circuits* (Elseveir, New York, USA, 2003).

[43] M. Horno, F. L. Mesa, F. Medina, and R. Marqués, Quasi-TEM analysis of multi-layered, multiconductor coplanar structures with dielectric and magnetic anisotropy including substrate losses, IEEE Trans. Microw. Theory Techn. **38**, 1059 (1990).

[44] S. Doyle, "Lumped element kinetic inductance detectors", PhD thesis (Cardiff University, 2008).

[45] T. P. Orlando and K. A. Delin, *Foundations of Applied Superconductivity* (Addison-Wesley Publishing Company, Massachusetts, USA, 1990).

[46] W. T. Weeks, L. L. H. Wu, M. F. McAllister, and A. Singh, Resistive and inductive skin effect in rectangular conductors, IBM Journal of Research and Development **23**, 652 (1979).

[47] A. Porch, M. J. Lancaster, and R. G. Humphreys, The coplanar resonator technique for determining the surface impedance of $YBa_2Cu_3O_{7-\delta}$ thin films, IEEE Trans. Microw. Theory Tech **43**, 306 (1995).

[48] J. Mateu, "Sheen analysis to a CPW transmission line", MATLAB® Code, 2015.

[49] P. Dhakal, G. Ciovati, G. R. Myneni, K. E. Gray, N. Groll, P. Maheshwari, D. M. McRae, R. Pike, T. Proslier, F. Stevie, R. P. Walsh, Q. Yang, and J. Zasadzinzki, Effect of high-temperature heat treatments on the quality factor of a large-grain superconducting radio-frequency niobium cavity, Phys. Rev. ST Accel. Beams **16**, 042001 (2013).

[50] E. M. Lechner, J. W. Angle, F. A. Stevie, M. J. Kelley, C. E. Reece, and A. D. Palczewski, RF surface resistance tuning of superconducting niobium via thermal diffusion of native oxide, Appl. Phys. Lett. **119**, 082601 (2021).

[51] J. Makita, G. Ciovati, and P. Dhakal, Temperature mapping of nitrogen-doped niobium superconducting radio frequency cavities, in Proc. of IPAC2015 (2015).

[52] P. Dhakal, Nitrogen doping and infusion in SRF cavities: a review, Physics Open **5**, 100034 (2020).

[53] E. M. Lechner, B. D. Oli, J. Makita, G. Ciovati, A. Gurevich, and M. Iavarone, Elecron tunneling and x-ray photoelectron spectroscopy studies of the superconducting properties of nitrogen-doped niobium resonator cavities, Phys. Rev. Appl. **13**, 044044 (2020).

[54] B. Bonin and R. Roth, Q degradation of niobium cavities due to hydrogen contamination, in Proc. of 5th Workshop on RF Superconductivity (1991).

[55] H. Padamsee, *RF Superconductivity: Science, Technology, and Applications* (Wiley-VCH Verlag GmbH & Co. KGaA, Weinheim, Germany, 2009).

[56] B. Aune et al., Superconducting TESLA cavities, Phys. Rev. ST Accel. Beams **3**, 092001 (2000).

[57] G. Ciovati, H. Tian, and S. G. Corcoran, Buffered electrochemical polishing of niobium, J. Appl. Electrochem. **41**, 721 (2011).

[58] T. Kubo, Flux trapping in superconducting accelerating cavities during cooling down with a spatial temperature gradient, Prog. Theor. Exp. Phys. **5**, 053G01 (2016).

[59] A. Romanenko, A. Grassellino, O. Melnychuk, and D. A. Sergatskov, Dependence of the residual surface resistance of superconducting radio frequency cavities on the cooling dyanmics around T_c, J. Appl. Phys. **115**, 184903 (2014).

[60] D. Gonnella, R. Eichhorn, F. Furuta, M. Ge, D. Hall, V. Ho, G. Hoffstaetter, M. Liepe, T. O'Connell, S. Posen, P. Quigley, J. Sears, V. Veshcherevich, A. Grassellino, A. Romanenko, and D. A. Sergatskov, Nitrogen-doped 9-cell cavity performance in a test cryomodule for LCLS-II, J. Appl. Phys. **117**, 023908 (2015).

[61] J. Knobloch, H. Muller, and H. Padamsee, Design of a high speed, high resolution thermometry system for 1.5 GHz superconducting radio frequency cavities, Rev. Sci. Instrum. **65**, 3521 (1994).

[62] A. Gurevich and G. Ciovati, Effect of vortex hotspots on the radio-frequency surface resistance of superconductors, Phys. Rev. B **87**, 054502 (2013).

[63] J. Knobloch, Field emission and thermal breakdown in superconducting niobium cavities for accelerators, IEEE Trans. Appl. Supercond. **9**, 1016 (1999).

[64] A. Gurevch, Thermal RF breakdown of superconducting cavities, in Proceedings of the Workshop on Pushing the Limits of RF Superconductivity (2005).

[65] A. Gurevich, Reduction of dissipative nonlinear conductivity of superconductors by static and microwave magnetic fields, Phys. Rev. Lett. **113**, 087001 (2014).

[66] G. Ciovati, P. Dhakal, and A. Gurevich, Decrease of the surface resistance in superconducting niobium resonator cavities by the microwave field, Appl. Phys. Lett. **104**, 092601 (2014).

[67] M. P. Garfunkel, Surface impedance of type-I superconductors: calculation of the effect of a static magnetic field, Phys. Rev. **173**, 516 (1968).

[68] P. Fulde, Tunneling density of states for a superconductor carrying a current, Phys. Rev. **137**, A783 (1965).

[69] T. Proslier, M. Kharitonov, M. Pellin, J. Zasadzinski, and G. Ciovati, Evidence of surface paramagnetism in niobium and consequences for the superconducting cavity surface impedance, IEEE Trans. Appl. Supercond. **21**, 2619 (2011).

[70] A. Gurevich and T. Kubo, Surface impedance and optimum surface resistance of a superconductor with an imperfect surface, Phys. Rev. B. **96**, 184515 (2017).

[71] T. Kubo and A. Gurevich, Field-dependent nonlinear surface resistance and its optimization by surface nanostructuring in superconductors, Phys. Rev. B **100**, 064522 (2019).

[72] C. Antoine, *Materials and surface aspects in the development of SRF niobium cavities*, EuCARD editorial series on accelerator science (2012).

[73] H. Padamsee, Superconducting radio-frequency cavities, Annu. Rev. Nucl. Part. Sci. **64**, 175 (2014).

[74] R. C. Dynes, V. Narayanamurti, and J. P. Garno, Direct measurement of quasiparticle-lifetime broadening in a strong-coupled superconductor, Phys. Rev. Lett. **41**, 1509 (1978).

[75] R. C. Dynes and J. P. Garno, Tunneling study of superconductivity near the metal-insulator transition, Phys. Rev. Lett. **53**, 2437 (1984).

[76] N. Kopnin, *Theory of Nonequilibrium Superconductivity* (Oxford University Press, New York, USA, 2001).

[77] J. Bardeen, Tunneling from a many-particle point of view, Phys. Rev. Lett. **6**, 57 (1960).

[78] E. L. Wolf, *Principles of Electron Tunneling Spectroscopy: Second Edition* (Oxford University Press, Oxford, UK, 2012).

[79] B. Voitglander, *Scanning Probe Microscopy: Atomic Force Microscopy and Scanning Tunneling Microscopy* (Springer-Verlag, Berlin, Germany, 2015).

[80] E. Lechner, "Electron tunneling studies of materials for superconducting radio frequency applications", PhD thesis (Temple University, 2019).

[81] J. Halbritter, On the oxidation and on the superconductivity of niobium, Appl. Phys. A **43**, 1 (1987).

[82] A. Romanenko and D. I. Schuster, Understanding quality factor degradation in superconducting niobium cavities at low microwave field amplitudes, Phys. Rev. Lett. **119**, 264801 (2017).

[83] N. R. Groll, G. Ciovati, A. Grassellino, A. Romanenko, J. F. Zasadzinski, and T. Proslier, Insight into bulk niobium superconducting RF cavities performances by tunneling spectroscopy, arXiv: **1805.06359** (2018).

[84] A.-M. Valente-Feliciano, H. L. Phillips, C. E. Reece, J. Spradlin, X. Zhao, D. Gu, H. Baumgart, D. Beringer, R. A. Lukaszew, B. Xiao, and K. Seo, RF and structural characterization of SRF thin films, in Proc. of IPAC2010 (2010).

[85] G. Eremeev, L. Phillips, C. E. Reece, A.-M. Valente-Feliciano, and B. P. Xiao, Characterization of superconducting samples with SIC system for thin film developments: status and recent results, in Proc. of SRF2013 (2013).

[86] T. Junginger, W. Weingarten, and C. Welsch, Extension of the measurement capabilities of the quadrupole resonator, Rev. Sci. Instrum. **83**, 063902 (2012).

[87] R. Kleindienst, O. Kugeler, and J. Knobloch, Development of an optimized quadrupole resonator at HZB, in Proc. of SRF2013 (2013).

[88] P. B. Welander, M. Franzi, and S. Tantawi, Cryogenic RF characterization of superconducting materials at SLAC with hemispherical cavities, in Proc. of SRF2015 (2015).

[89] P. Goudket, O. B. Malyshev, S. Pattalwar, N. Pattalwar, L. Gurran, R. Valizadeh, L. B. Bizellot, and G. Burt, First full cryogenic test of the SRF thin film test cavity, in Proc. of SRF2017 (2017).

[90] O. B. Malyshev, P. Goudket, N. Pattalwar, S. Pattalwar, J. Conlon, and G. Burt, The SRF thin film test facility in LHe-free cryostat, in Proc. of SRF2019 (2019).

[91] J. T. Maniscalco, D. L. Hall, O. B. Malyshev, R. Valizadeh, and S. Wilde, New material studies in the Cornell sample host cavity, in Proc. of IPAC2016 (2016).

[92] D. Okai, M. Kusunoki, M. Mukaida, and S. Ohshima, Surface resistance measurement of superconducting thin film using probe-coupling-type microstrip line resonator, Electronics and Communications in Japan **86**, 27 (2003).

[93] Photo Sciences, *Photomasks, Patterned Optics, Shadow Masks, ITO: photo Sciences, Inc.* `https://www.photo-sciences.com/`, 2021.

[94] A.-M. Valente, G. Wu, L. Phillips, H. Wang, and A. Wu, Niobium thin film cavity deposition by ECR plasma, in Proceedings of EPAC'04 (2004).

[95] A.-M. Valente-Feliciano, H. L. Phillips, C. E. reece, and J. K. Spradlin, SRF multilayer structures based on NbTiN, in Proc. of SRF 2011 (2011).

[96] C. Sundahl, J. Makita, P. B. Welander, Y. F. Su, F. Kametani, L. Xie, H. Zhang, L. Li, A. Gurevich, and C. B. Eom, Development and characterization of Nb_3Sn/Al_2O_3 superconducting multilayers for particle accelerators, Sci. Rep. **11**, 7770 (2021).

[97] STAR Cryoelectronics, *SQUID sensors, readout electronics, cryogenic systems & foundry services*, `https://starcryo.com/`, 2022.

[98] P. J. Petersan and S. M. Anlage, Measurement of resonant frequency and quality factor of microwave reonsators: comparison of methods, J. Appl. Phys **84**, 3392 (1998).

[99] Z. Ma, "RF properties of high temperature superconducting materials", PhD thesis (Stanford University, 1995).

[100] J. Gao, "The physics of superconducting microwave resonators", PhD thesis (California Institute of Technology, 2008).

[101] J. Krupka, R. G. Geyer, M. Kuhn, and J. H. Hinken, Dielectric properties of single crystals of Al_2O_3, $LaAlO_3$, $NdGaO_3$, $SrTiO_3$, and MgO at cryogenic temperatures, IEEE Trans. Microw. Theory Techn. **42**, 1886 (1994).

[102] J. P. Turneaure, J. Halbritter, and H. A. Schwettman, The surface impedance of superconductors and normal conductors: the Mattis-Bardeen theory, J. Supercond. **4**, 341 (1991).

[103] C. Sundahl, "Synthesis of superconducting Nb_3Sn thin film heterostructures for the study of high-energy RF physics", PhD thesis (University of Wisconsin-Madision, 2019).

[104] M. Hein, *High-Temperature-Superconductor Thin Films at Microwave Frequencies* (Springer-Verlag, Heidelberg, Germany, 1999).

[105] S. K. Yip and J. A. Sauls, Nonlinear Meissner effect in CuO superconductors, Phys. Rev. Lett. **69**, 2264 (1992).

[106] D. Xu, S. K. Yip, and J. A. Sauls, Nonlinear Meissner effect in unconventional super-conductors, Phys. Rev. B **51**, 16233 (1995).

[107] T. Dahm and D. J. Scalapino, Theory of intermodulation in a superconducting mi-crostrip resonator, J. Appl. Phys. **81** (2002).

[108] T. Dahm and D. J. Scalapino, Nonlinear current response of a d-wave superfluid, Phys. Rev. B **60**, 13125 (1999).

[109] M.-R. Li, P. J. Hirschfeld, and P. Wölfle, Is the nonlinear Meissner effect unobservable, Phys. Rev. Lett. **81**, 5640 (1998).

[110] M.-R. Li, P. J. Hirschfeld, and P. Wölfle, Free energy and magnetic penetration of a d-wave superconductor in the Meissner state, Phys. Rev. B **61**, 648 (2000).

[111] R. Prozorov and R. W. Giannetta, Magnetic penetration depth in unconventional superconductors, Supercond. Sci. Technol. **19**, R41 (2006).

[112] J. Makita, C. Sundahl, G. Ciovati, C. B. Eom, and A. Gurevich, Nonlinear Meissner effect in Nb_3Sn coplanar resonators, Phys. Rev. Res. **4**, 013156 (2022).

[113] J. Bardeen, Critical fields and currents in superconductors, Rev. Mod. Phys. **34**, 667 (1962).

[114] K. Maki, On persistent currents in a superconducting alloy. II, Prog. Theor. Phys. **29**, 333 (1963).

[115] C. P. Bidinosti, W. N. Hardy, D. A. Bonn, and R. Liang, Magnetic field dependence of λ in $YBa_2Cu_3O_{6.95}$: results as a function of temperature and field orientation, Phys. Rev. Lett. **83**, 3277 (1999).

[116] A. Bhattacharya, I. Zutic, O. T. Valls, A. M. Goldman, U. Welp, and B. Veal, Angular dependence of the nonlinear transverse magnetic moment of $YBa_2Cu_3O_{6.95}$ in the Meissner state, Phys. Rev. Lett. **82**, 3132 (1999).

[117] A. Carrington, R. W. Giannetta, J. T. Kim, and J. Giapintzakis, Absence of nonlinear Meissner effect in $YBa_2Cu_3O_{6.95}$, Phys. Rev. B **59**, R14173 (1999).

[118] K. Halterman, O. T. Valls, and I. Žutić, Reanalysis of the magnetic field dependence of the penetration depth: observation of the nonlinear Meissner effect, Phys. Rev. B **63**, 180405(R) (2001).

[119] D. E. Oates, S.-H. Park, and G. Koren, Observation of the nonlinear Meissner effect in YBCO thin films: evidence for a d-wave order parameter in the bulk of the cuprate superconductors, Phys. Rev. Lett. **93**, 197001 (2004).

[120] D. E. Oates, Overview of nonlinearity in HTS: what we have learned and prospects for improvement, J. Supercond. Novel Magn. **20**, 3 (2007).

[121] A. Carrington, Studies of the gap structure of iron-based superconductors using magnetic penetration depth, C. R. Phys. **12**, 502 (2011).

[122] A. A. Abrikosov, On the lower critical field of thin layers of superconductors of the second group, Sov. Phys. JETP **19**, 998 (1964).

[123] MicroXact, Inc., *SCM-50-CF Closed Cycle Cryomagnetic Probe Station*, `http://microxact.com/`, 2017.

[124] D. Hafner, M. Dressel, and M. Scheffler, Surface-resistance measurements using superconducting stripline resonators, Rev. Sci. Instrum. **85**, 014702 (2014).

[125] B. Abdo, E. Segev, O. Shtempluck, and E. Buks, Nonlinear dynamics in the resonance line shape of NbN superconducting resonators, Phys. Rev. B **73**, 13 (2006).

[126] M. S. W. Jansen, Chemical compositions at and near the grain boundaries in bronze-processed superconducting Nb_3Sn, Appl. Phys. Lett. **43**, 791 (1983).

[127] M. J. R. Sandim, D. Tytko, A. Kostka, P. Choi, S. Awaji, K. Watanabe, and D. Raabe, Grain boundary segregation in a bronze-route Nb_3Sn superconducting wire studied by atom probe tomography, Supercond. Sci. Technol. **26**, 055008 (2013).

[128] J. Lee, S. Posen, Z. Mao, Y. Trenikhina, K. He, D. L. Hall, M. Liepe, and D. N. Seidman, Atomic-scale analyses of Nb_3Sn on Nb prepared by vapor diffusion for superconducting radiofrequency cavity applications: a correlative study, Supercond. Sci. Technol. **26**, 055008 (2013).

[129] J. H. Durrel, C. B. Eom, A. Gurevich, E. E. Hellstrom, C. Tarantini, A. Yamamoto, and D. C. Larbalestier, The behavior of grain boundaries in the Fe-based superconductors, Rep. Prog. Phys. **74**, 124511 (2011).

[130] T. L. Hylton and M. R. Beasley, Effect of grain boundaries on magnetic field penetration in polycrystalline superconductors, Phys. Rev. B **39**, 9042 (1989).

[131] A. Godeke, A review of the properties of Nb_3Sn and their variation with A15 composition, morphology and strain state, Supercond. Sci. Technol. **19**, R68 (2006).

[132] T. P. Orlando, W. J. McNiff, S. Foner, and M. R. Beasley, Critical fields, Pauli paramagnetic limiting, and material parameters of Nb$_3$Sn and V$_3$Si, Phys. Rev. B **19**, 4545 (1979).

[133] L. Kramer and R. J. Watts-Tobin, Theory of dissipative current-carrying states in superconducting filaments, Phys. Rev. Lett. **40**, 1041 (1978).

[134] J. Lee, Z. Mao, K. He, Z. H. Sung, T. Spina, S.-I. Baik, D. L. Hall, M. Liepe, D. N. Seidman, and S. Posen, Grain-boundary structure and segregation in Nb$_3$Sn coatings on Nb for high-performance superconducting radiofrequency cavity applications, Acta Mater. **188**, 155 (2020).

[135] A. Barone and G. Paterno, *Physics and Applications of Josephson Effect* (Wiley, New York, USA, 1982).

[136] K. Borisov, D. Rieger, P. Winkel, F. Henriques, F. Valenti, A. Ionita, M. Wessbecher, M. Spiecker, D. Gusenkova, I. M. Pop, and W. Wernsdorfer, Superconducting granular aluminum resontaors resilient to magnetic fields up to 1 Tesla, Appl. Phys. Lett. **117**, 120502 (2020).

[137] P. Morse and H. Feshbach, *Methods of Theoretical Physics, Part I* (McGraw-Hill, New York, USA, 1953).

APPENDIX A

CALCULATING L AND C BY CONFORMAL MAPPING

A detail of calculating L and C using a conformal mapping technique is described here. For $t \ll w$, the cross-sectional geometry of the CPW is assumed to have zero-thickness with the ground planes extending to infinity as shown in Fig. 78(a). This zero-thickness
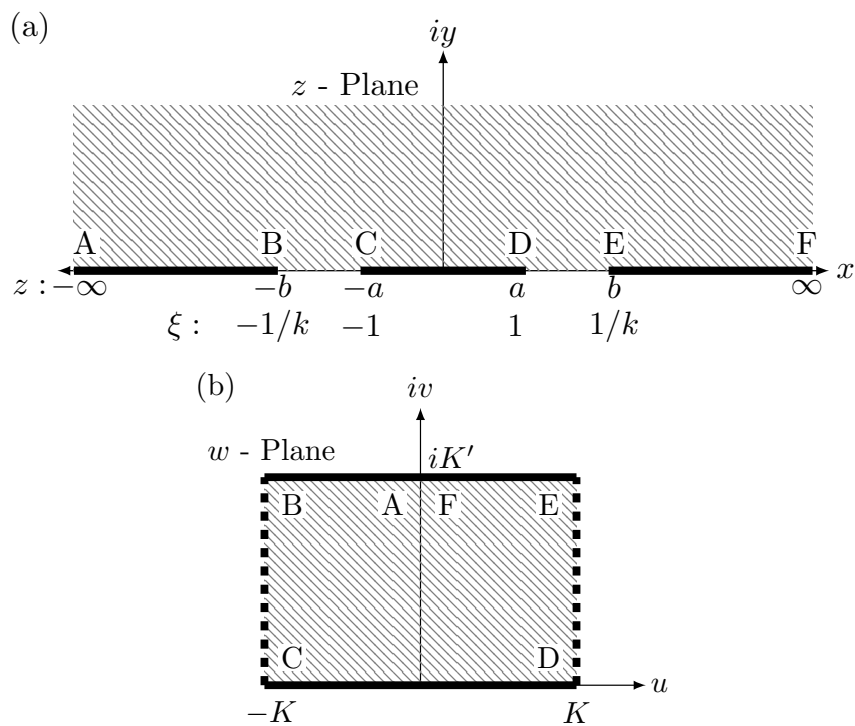

FIG. 78: (a) Coplanar waveguide with zero thickness, and (b) mapping on w-plane

CPW is then conformal mapped into a simpler geometry where L and C can be calculated

analytically. Using a type of transformation called Schwarz-Christoffel mapping, the shaded, upper-half z-plane is mapped into a closed rectangle in the w-plane as shown in Fig. 78(b). The transformation that maps z-plane to w-plane is [40]

$$w(z) = A \int_0^z \frac{dz}{\sqrt{(z - x_1)(z - x_2)(z - x_3)(z - x_4)}}, \tag{151}$$

where x_1, x_2, x_3, and x_4 correspond to points B, C, D, and E on Fig. 78. After plugging in $x_1 = -b$, $x_2 = -a$, $x_3 = a$, and $x_4 = b$, Eq. (151) becomes

$$w(z) = A \int_0^z \frac{dz'}{\sqrt{(z'^2 - a^2)(z'^2 - b^2)}}. \tag{152}$$

Changing variables $\xi = z/a$ and $k = a/b$ yield

$$w(z) = \frac{A}{b} \int_0^\xi \frac{d\xi'}{\sqrt{(1 - \xi'^2)(1 - k^2\xi'^2)}}. \tag{153}$$

The complex factor in front of the integral is a normalization factor which can be set to 1. This expression is equivalent to an inverse elliptic function:

$$w(z) = sn^{-1}(\xi, k). \tag{154}$$

The transformation from $w-$plane to $z-$plane is then simply the elliptic function:

$$z(w) = sn(w, k). \tag{155}$$

The values of w that result in the appropriate coordinate values ξ defined in Fig. 78(a) is then

$$sn(0, k) = 0, \tag{156}$$

$$sn(\pm K(k), k) = \pm 1, \tag{157}$$

$$sn(\pm K(k) + iK(k'), k) = \pm \frac{1}{k}, \tag{158}$$

$$sn(iK(k'), k) = \pm\infty, \tag{159}$$

where $K(k)$ and $iK(k)$ are the complete elliptic integral of the first and seoncd kind respectively [137]:

$$K(k) = \int_0^1 \frac{d\xi}{\sqrt{(1 - \xi^2)(1 - k^2\xi^2)}}, \tag{160a}$$

$$iK'(k) = \int_1^{1/k} \frac{d\xi}{\sqrt{(\xi^2 - 1)(1 - k^2\xi^2)}} = \int_0^1 \frac{d\xi}{\sqrt{(1 - \xi^2)(1 - \xi^2 - k^2\xi^2)}} = K(k'), \tag{160b}$$

with $k' = \sqrt{1-k^2}$. The mapping transforms points listed (A–F) in Fig. 78(a) to the corresponding points in Fig. 78(b), and the upper half of the z-plane is mapped into the interior of the rectangle.

Now the capacitance per unit length between the center strip and the ground plane through just the upper plane in z can be computed easily by calculating the capacitance of the parallel plate capacitor in w-plane:

$$C_{air} = 2\epsilon_0 \frac{K(k)}{K(k')}. \tag{161}$$

The capacitance through the lower plane in z in which represent the portion filled with a dielectric material is same as that of upper plane except with the extra factor of e_r. The total capacitance per length is the sum:

$$C = (1 + \epsilon_r)\,C_{air} = \frac{1 + \epsilon_r}{2}\epsilon_0 \frac{4K(k)}{K(k')}, \tag{162}$$

$$= \epsilon_e \epsilon_0 \frac{4K(k)}{K(k')}. \tag{163}$$

Where ϵ_e is called effective dielectric constant because the presence of dielectric substrate increases the capacitance by a factor of ϵ_e.

The inductance per unit length can be computed by considering the current I running into the page on the bottom plate and $-I$ on the upper plate of the parallel plate capacitor. The magnetic field produced by such current is

$$\boldsymbol{B} = \mu_0 \frac{I}{2K(k)}. \tag{164}$$

The flux is then

$$\Phi = \mu_0 I \frac{K(k')}{2K(k)}. \tag{165}$$

Hence, the inductance per unit length on the upper part is

$$L_{air} = \mu_0 \frac{K(k')}{2K(k)}. \tag{166}$$

The inductance on the bottom part is equivalent to the upper part since the relative permeability is assumed to be 1 in the dielectric medium. The total inductance is then

$$L = \mu_0 \frac{K(k')}{4K(k)}. \tag{167}$$

VITA

Junki Makita

Department of Physics

Old Dominion University

Norfolk, VA 23529

Eductaion:

M.S. Physics, Old Dominion University, Norfolk, VA. December 2015

B.A. Physics, Cornell University, Ithaca, NY. May 2012

Selected Publications:

- J. Makita, G. Ciovati, and P. Dhakal, Temperature mapping of nitrogen-doped niobium superconducting radio frequency cavities, in *Proc. of IPAC 2015* (Richmond, USA, 2015).

- J. Makita, C. Sundahl, G. Ciovati, C. B. Eom, and A. Gurevich, Nonlinear meissner effect in Nb_3Sn coplanar resonators, Phys. Rev. Res. **4**, 013156 (2022).

- E. M. Lechner, B. D. Oli, J. Makita, G. Ciovati, A. Gurevich, and M. Iavarone, Electron tunneling and x-ray photoelectron spectroscopy studies of the superconducting properties of nitrogen-doped niobium resonator cavities, Phys. Rev. Appl. **13**, 044044 (2020).

- C. Sundahl, J. Makita, P. B. Welander, Y. F. Su, F. Kametani, L. xie, H. Zhang, L. Li, A. Gurevich, and C. B. Eom, Development and characterization of Nb_3Sn/Al_2O_3 superconducting multilayers for particle accelerators, Sci. Rep. **11**, 7770 (2021).

Typeset using LaTeX.